

A STIS SURVEY FOR O VI ABSORPTION SYSTEMS AT $0.12 < z \lesssim 0.5$ II.: PHYSICAL CONDITIONS OF THE IONIZED GAS

C. THOM AND HSIAO-WEN CHEN

Dept. of Astronomy & Astrophysics and Kavli Institute for Cosmological Physics
 University of Chicago, Chicago, IL, 60637, U.S.A.
 cthom, hchen@oddjob.uchicago.edu

Draft version June 28, 2018

ABSTRACT

We present a complete catalogue of 27 O VI absorbers at low redshift ($0.12 < z < 0.5$) from a blind survey of 16 QSO echelle spectra in the HST/STIS data archive. These absorbers are identified based only upon matching line profiles and the expected doublet ratio between the $\lambda\lambda$ 1031, 1037 transitions. Subsequent searches are carried out to identify their associated transitions. Here we present all relevant absorption properties. By considering absorption components of different species which are well-aligned in velocity-space, we derive gas temperatures and non-thermal broadening values, b_{nt} . We show that in all 16 cases considered the observed line width is dominated by non-thermal motion and that gas temperatures are well below those expected for O^{5+} in collisional ionization equilibrium. This result reaffirms previous findings from studies of individual lines of sight, but are at odds with expectations for a WHIM origin. At least half of the absorbers can be explained by a simple photoionization model. In addition, in some absorbers we find evidence for large variation in gas density/metallicity across components in individual absorbers. Comparisons of multiple associated metal species further show that under the assumption of the gas being photoionized by the metagalactic background radiation field, the absorbing clouds have gas densities $< n_H > < -2.9$ and sizes $L > 1$ kpc. Finally, we compare our absorber selection with the results of other independent studies.

Subject headings: cosmology: observations—intergalactic medium—quasars: absorption lines

1. INTRODUCTION

One of the current key questions in observational cosmology is the location of the missing baryons. The *total* baryon content of the universe is well constrained, with various measurements in relatively good agreement (e.g. Burles et al. 2001; Spergel et al. 2003; O’Meara et al. 2006). In the high-redshift universe, the Ly α forest dominates the baryon census (Rauch et al. 1997), but in the present day universe, only 1/3 of the baryons have been identified in known components (Fukugita & Peebles 2004). Cosmological simulations indicate that up to 50% of the baryons exist in a warm-hot intergalactic medium (WHIM), in which gas is shock-heated to $\sim 10^5 - 10^7$ K by the accretion onto large-scale structures, and remains hot owing to the low gas density and inefficient cooling (Cen & Ostriker 1999; Davé et al. 2001; Cen & Ostriker 2006). This gas is a result of accretion onto large-scale filamentary structures, where cooling is inefficient due to the low densities, and (in some models) the operation of large scale winds that shock-heat outflowing gas to $\sim 10^6$ K (e.g. Cen & Ostriker 2006). It is therefore important to identify this gas, and constrain its contribution to the baryon fraction.

At the temperature range in question ($\log T = 5.0 - 7.0$), the best observational window for this hot gas is X-ray absorption lines (e.g. O VII K α , O VIII K α , Ne IX K α ; Gnat & Sternberg 2007), but the resolutions of current X-ray spectrographs (e.g. Chandra and XMM/Newton) are an order of magnitude too coarse to

be useful, and the sensitivities are more than an order of magnitude too low (e.g. Fang et al. 2006). The best tool currently available, therefore, is UV absorption spectroscopy. The O VI doublet ($\lambda\lambda$ 1031.9261, 1037.617 Å) offers the best hot gas tracer for a number of reasons: the transition has a large oscillator strength; Oxygen is a relatively common metal; the abundance of the O^{5+} ion peaks in collisional ionization equilibrium (CIE) at $\log T \sim 5.3^2$; the transition occurs longward of the Lyman limit; and absorption can be detected down to limiting column densities $\log N \approx 13.5$ ($W_r = 30$ mÅ) with current instruments such as STIS.

If the absorption lines of an element are resolved and unsaturated, we can measure directly the column density (N) and Doppler parameter (b) of the absorbing gas by voigt profile fitting³. The Doppler parameter is an oft-used measure of the temperature of the gas, through the well-known relation $b^2 = b_{nt}^2 + 2kT/m$, where b_{nt} accounts for non-thermal broadening of the line due to e.g. turbulence. The column-density, meanwhile, may be used in conjunction with the path-length to derive the contribution to the cosmological mass density of the O^{5+} ions, $\Omega_{O^{5+}}$ (see Thom & Chen 2008, hereafter paper I).

In the optical band, ground-based high resolution (echelle) spectra have made O VI detection possible at $2.3 \lesssim z \lesssim 3$ (e.g. Norris et al. 1983; Carswell et al. 2002; Simcoe et al. 2002). The lower limit is set by the plummeting transmissivity of the atmosphere to UV

² It also has an ionization fraction greater than 10^{-2} up to $\log T \sim 5.7$; see e.g. Gnat & Sternberg (2007).

³ In cases where multiple transitions of the same species are available, a curve-of-growth analysis can also be used.

¹ Based in part on observations with the NASA/ESA Hubble Space Telescope, obtained at the Space Telescope Science Institute, which is operated by the Association of Universities for Research in Astronomy, Inc., under NASA contract NAS5-26555.

photons below $\sim 3500 \text{ \AA}$, while the upper limit is set by confusion with the Ly α forest. In the high-redshift regime, O^{5+} is predominantly photoionized by the UV background radiation field, much the same as the Ly α clouds (Carswell et al. 2002; Simcoe et al. 2004). To push to lower redshifts, space-based UV spectrographs are required. Using near-UV spectra from the Faint Object Spectrograph on-board HST, Burles & Tytler (1996) identified 12 O VI doublets with $W_r(1031) > 0.21 \text{ \AA}$ in the range $0.5 \lesssim z \lesssim 2$ and derived a cosmological mass density $\Omega_{\text{O}^{5+}} h \geq 7 \times 10^{-8}$, providing the first constraint on the mass density of this highly ionized gas.

In the low-redshift universe ($z \lesssim 0.5$), the O VI doublet transition remains in the far-UV ($\lambda_{\text{obs}} \lesssim 1600 \text{ \AA}$). The terminated Far Ultraviolet Spectroscopic Explorer (*FUSE*; Moos et al. 2000) could probe O VI absorption out to $z \sim 0.15$ with good signal-to-noise, but at a resolution of only $\sim 20 \text{ km s}^{-1}$ (e.g. Danforth & Shull 2005). This compares poorly with the thermal line width of O VI ($\sim 3 \text{ km s}^{-1}$ at $\log T = 4.0$ and $\sim 10 \text{ km s}^{-1}$ at $\log T = 5.0$). The (currently suspended) Space Telescope Imaging Spectrograph (*STIS*; Woodgate et al. 1998) on-board the Hubble Space Telescope (*HST*) offers a resolution of $\sim 6\text{--}7 \text{ km s}^{-1}$ and its data are useful for studies of O VI absorption at slightly higher redshifts than *FUSE* ($0.12 < z < 0.5$).

Early work on O VI absorption in the low- z universe typically concentrated on single lines of sight, due to the paucity of data. Single-sightline or single-absorber analyses have been conducted on the various lines of sight, beginning with the QSO H 1821+643 (Tripp et al. 1998, 2000, 2001; Oegerle et al. 2000). As more data become available, further sightline were analysed: PG0953+415 (Savage et al. 2002), PG1259+593 (Richter et al. 2004), PG1116+215 821 (Sembach et al. 2004), PKS0405–123 (Prochaska et al. 2004), HE0226–4110 (Lehner et al. 2006) and PKS1302–102 (Cooksey et al. 2008). Now, with a database of UV data available⁴, statistical approaches have become possible (Danforth & Shull 2005; Danforth et al. 2006; Thom & Chen 2008; Tripp et al. 2008; Danforth & Shull 2008).

This is the second in a series of papers reporting the results of our search for O VI absorption systems in the *STIS* E140M archive. Unlike other searches, we employ a *blind* search for O VI doublets, which is independent of *a priori* knowledge of the presence of other transitions such as Ly α . In paper I we reported results on the statistics of the O VI absorbers. The major results were: a) a measurements of the number of absorbers per unit redshift, $dN(W \geq 30 \text{ m\AA})/dz = 10.4 \pm 2.2$; b) a measurement of the cosmological mass density of the O^{5+} gas, $\Omega_{\text{O}^{5+}} h = (1.7 \pm 0.3) \times 10^{-7}$; c) $< 5\%$ of O VI absorbers originate in underdense regions that do not show a significant trace of H I; d) H I column densities of O VI absorbers span more than 5 orders of magnitude, and a moderate correlation exists between $N(\text{H I})$ and $N(\text{O VI})$; and e) the number density of O VI absorbers along a given line of sight appears to be inversely correlated with the number density of H I absorbers. In this paper we present our catalogue of O VI absorbers upon

which the results of paper I are based. We also address the physical conditions of the O^{5+} bearing gas. The nature of the IGM, the O VI absorbers in particular, and their relation to the WHIM is an area that has seen much recent progress. At least two other groups have contemporaneously reported results of similar analyses. We refer the interested reader to the works of Tripp et al. (2008) and Danforth & Shull (2008). Specifically, see Tripp et al. (2008) Sec 4 for comments on the differences between both works.

We recall the description of our search and selection technique from paper I in Sec 2, presenting the full table of absorbers. We discuss individual lines-of-sight, and present the measured quantities for each system, in Sec 3. In Sec 4 we discuss those systems reported in Tripp et al. (2008) that are not accepted by our selection criteria. The physical properties of the ionized gas selected via O VI absorption are discussed in Sec 5. Sec 6 contains a summary and concluding remarks.

2. DATA AND CATALOGUE

2.1. *STIS* Data

Our data were drawn from the *STIS* data archive⁵. The data and search technique is described in paper I (see in particular, Sec 2.1 for details). For completeness, we repeat parts of that description here. We chose all data with sufficient signal-to-noise ratio ($S/N \geq 5$ per pixel), and resolution, as to be able to detect weak ($W_r > 30 \text{ m\AA}$) O VI absorbers. This selection yielded 16 lines of sight with *STIS* E140M data. Table 1 describes these lines of sight.

O VI absorbers were selected on the basis of the equivalent width ratio of the doublet lines alone. In order not to bias our search by the presence of other transitions, we do not consider other associated lines until a later stage. This differs from the traditional technique, which relies on *a priori* knowledge of absorber positions (usually from Ly α), and then searches for possibly associated species. We began our search by Hanning smoothing the spectra, and identifying all deviations $> 1.5 \sigma$ from the continuum level. A gaussian profile was fit to each feature, with the width restricted to $6 < \sigma < 300 \text{ km s}^{-1}$, where the lower limit is taken from the spectrograph resolution, and the upper limit from consideration of the line width distribution of known O VI systems (e.g. Heckman et al. 2002; Danforth & Shull 2005). An equivalent width was determined by directly integrating the data, with integration limits determined from the gaussian width. All features with $< 2 \sigma$ significance were rejected.

We consider each feature a putative O VI 1031 line and fit a doublet absorption model to the data to determine whether the spectrum is consistent with the presence of both O VI 1031, 1037 lines. The doublet model requires both transitions to have the same line width, and have a line strength ratio of 2 : 1 (i.e. the ratio of the oscillator strength–wavelength product, $f \lambda^2$, for the two transitions). Each system was also visually inspected to determine whether the spectrum is consistent with the presence of a doublet. We accepted candidates if (a) the O VI 1031 member has $> 3 \sigma$ significance, and; (b) the ratio of rest-frame line strengths—

⁴ More data are likely soon to be available with the upcoming HST servicing mission.

⁵ CALSTIS v2.23 (2006 Oct 06)

$R_{\text{O VI}} \equiv W_r(1031)/W_r(1037)$ —lies between $1 - \sigma_{R_{\text{O VI}}}$ and $2 + 2\sigma_{R_{\text{O VI}}}$.

Finally, we visually identified other species associated with each absorber, typically searching for transitions of the ions H^0 , $\text{Si}^{+,2+,3+}$, $\text{S}^{+,2+}$, $\text{O}^{0,2+,3+}$, $\text{C}^{+,2+}$, $\text{N}^{+,4+}$ and Ne^{7+} . The *vpfit*⁶ software was used to fit Voigt profiles to all components of all detected species in each absorber. *vpfit* convolves the voigt profile with a gaussian line-spread function (LSF), whose width is set by the instrument resolution. The STIS LSF has significant broad wings in some configurations. We have tested that this difference does not affect our measurements of N and b (i.e. the differences are much smaller than the error in the measured values). The number, position and initial values for the absorption components was assessed initially by eye. We performed a minimum- χ^2 analysis that includes multiple components; new components were added and fit iteratively until either the normalized χ^2 did not decrease, or the newly added component became ill-constrained (error-bars for the best-fit parameters were greater than the best-fit values) by the data. For O VI and H I, this process is typically facilitated by the presence of multiple transitions. Section 3 has details of the component structure for each absorber. The fits were used to evaluate the total column density for each absorber, and are given in Table 2. Fit results for the individual components that comprise each absorber are given in Tables 3–17. In our fitting, we employed the latest version of the standard atomic data distributed with *vpfit*. These data are primarily from the compilation of Morton (2003), with some more recent updates included.

2.2. A Catalogue of Random O VI Absorbers at $0.12 < z < 0.50$

The final catalogue of O VI doublet systems is given in Table 2. The table lists the line-of-sight and redshift of the absorber, typically the redshift of the strongest O VI component (columns 1 & 2). Rest-frame equivalent widths (W_r), and errors (σ_{W_r}), are reported in units of mÅ (columns 3–6), for both lines of the O VI doublet. The ratio of equivalent widths, $R_{\text{O VI}}$, and associated error are listed in columns (7) and (8). Finally, columns (9) and (10) give the total O VI column density for the absorber, which is the sum of the individual components. Individual component fitting results are given in the following section.

3. INDIVIDUAL LINES OF SIGHT

For each absorber in the following sub-sections, we present the results of our profile fitting in the associated figures and tables. Spectra are unbinned, and profile fits are overlayed in solid (blue). The error spectrum is plotted as a solid line at the bottom of each panel (red), also unbinned. The dot-dashed (green) lines indicate the continuum and zero flux levels. Component positions are marked above the spectra with the (red) solid ticks. The tables list, for each absorber along each line of sight, the ion, component position in redshift (z) and velocity offset (v) (from the absorber redshift), and the profile fit Doppler parameter (b) and column-density ($\log N$), and their associated errors. The flags denote upper (U) and

lower (L) limits, or uncertain features (Z). Note that errors are not reported for upper and lower limits.

3.1. 3C 249.1

The QSO 3C 249.1 lies at $z_{\text{qso}} = 0.3115$, and we searched for O VI absorption along the line of sight from $0.122 < z_{\text{abs}} < 0.2885$. We identify a single O VI doublet system along this line of sight.

$z_{\text{abs}} = 0.24676$ (Figure 1; Table 3)—This system shows a clear detection of both O VI lines, strong Ly α , β , and tentative Si III 1206. The O VI 1037 line shows warm pixels on the very edges of the line wings, which do not affect our line fits. The blue wing of the Ly β line partially blends with another strong line, which we tentatively identify as Ly α at $z = 0.0517$. We cannot check this assignment, as the corresponding Ly β line for this putative assignment is below our wavelength range. In the unblended region, the model fit to the data is good. The Ly γ line is on the edge of the Galactic Ly α trough, and was excluded from our fits. The Si III line is very weak and offset from the O VI and H I absorption ($\Delta v = 11 \pm 3 \text{ km s}^{-1}$); its identification is thus uncertain. With the well aligned O VI and H I components, we derive $b_{\text{nt}} = 26.1 \text{ km s}^{-1}$ and $\log T = 4.7$; see Sec 5.2 for details.

3.2. 3C 273

The STIS data for 3C 273 ($z_{\text{qso}} = 0.1583$) are of excellent quality, but offer only a short path-length over which to detect O VI doublet systems ($0.1144 < z_{\text{abs}} < 0.1417$). The lowest redshift absorber in our sample, at $z_{\text{abs}} = 0.12003$ is detected along this line of sight.

$z_{\text{abs}} = 0.12003$ (Figure 2; Table 4)—This narrow, weak, single-component absorber is the lowest redshift absorber in our sample, and is detectable at such a low wavelength ($\lambda_{\text{obs}} = 1156 \text{ Å}$) only due to the high quality data for the 3C 273 sightline. For both O VI lines, while noisy, the data show corresponding profiles, and the model fits are satisfactory for both lines. The line strengths from direct integration of the data, are mismatched (the equivalent width ratio is $\sim 1.0 \pm 0.4$), but neither line can be weak Ly α (the system is blueward of the Galactic Ly α line). Of the H I lines, only Ly α is present in our data at such low redshifts, and the line is unsaturated and well fit by a single component. Due to the simple structure, we are able to derive $b_{\text{nt}} = 6.6 \text{ km s}^{-1}$ and the gas temperature, $\log T = 4.5$; see Sec 5.2 for details.

3.3. 3C 351.0

3C 351.0 lies at $z_{\text{qso}} = 0.3716$, giving a usable path-length for detecting O VI systems $0.1309 < z_{\text{abs}} < 0.3483$. We detect only a single O VI doublet along this line of sight.

$z_{\text{abs}} = 0.31659$ (Figure 3; Table 5)—This system shows a complex structure, with three well-defined O VI components present, and corresponding H I profiles. The Ly α line is saturated, but the Ly β line shows three components that are well aligned with the O VI. The weak Ly γ line is noisier and less well fit by this H I model; the Ly δ line is contaminated by Galactic S II 1250 absorption. No C III 977 is observed; the strong, putative C III 977 line which aligns with the red-most O VI component is H I 937 at $z = 0.37193$, associated with

⁶ <http://www.ast.cam.ac.uk/~rfc/vpfit.html>

the QSO host. As all three O VI components are well-aligned with the three H I components, we attempt to derive the gas temperature and non-thermal broadening. For the components at $v = -3, -53 \text{ km s}^{-1}$ we derive $b_{nt} = 23.0, 19.5 \text{ km s}^{-1}$ and $\log T = 4.1, 4.8$ respectively. For the component at $v = +62 \text{ km s}^{-1}$, we cannot find a solution since $b_{\text{O VI}} > b_{\text{H I}}$; at the 1σ level this component is consistent with a system whose Doppler parameter is entirely dominated by non-thermal broadening. Sec 5.2 contains further discussion of this case.

3.4. H 1821+643

The H 1821+643 ($z_{\text{qso}} = 0.297$) line has been studied extensively in terms of intervening absorbers. Tripp et al. (1998) used GHRs and galaxy redshifts to study the Ly α absorbers. Tripp et al. (2000) followed up with STIS observations, focusing on O VI absorption, complemented by Oegerle et al. (2000) with FUSE observations. The STIS data allow us to search for O VI absorbers between $0.1144 < z_{\text{abs}} < 0.2741$. We uncover four absorbers at $z_{\text{abs}} = 0.22496, 0.22638, 0.24532, 0.26656$.

$z_{\text{abs}} = 0.22496$ (Figure 4; Table 6)—This absorber and the next (H 1821+643; $z_{\text{abs}} = 0.22638$) are separated by only $\sim 350 \text{ km s}^{-1}$, but the two absorbers appear to be physically distinct systems (as opposed to components of the same absorption system). The O VI absorption consists of a broad, strong component, with a very weak, narrow component on the red edge. The associated Ly α, β lines are strongly saturated, while the Ly γ, δ lines show some saturation. Three separate H I components are included in the fit, but $N(\text{H I})$ is a lower limit; the two strong components are saturated in the three lowest order Lyman lines, while the Ly δ line is very noisy. The C III 977 profile is similarly complex, with several possible weak components evident around the three main, strong components, (at least two of which show signs of saturation). There are three well-defined but unsaturated Si III 1206 components corresponding to the strong C III 977 absorption lines. The $v = 0 \text{ km s}^{-1}$ component of Si III and the $v = -6 \text{ km s}^{-1}$ C III absorption component, while aligned with the main O VI absorption, cannot arise in the same gas phase, since e.g. $b_{\text{Si III}} \ll b_{\text{O VI}}$, and we require $0.8 < b_{\text{Si III}}/b_{\text{O VI}} < 1.0$. These limits are discussed in more detail in Sec 5.2. At least two weak Si IV 1393 components are also present, which align with the two strongest C III components, but are too weak to be detected in the weaker Si IV 1402 doublet transition. $z_{\text{abs}} = 0.22638$ (Figure 5; Table 6)—The weak absorber at $z = 0.22638$ is separated from the strong system at $z = 0.22496$ by only $\sim 350 \text{ km s}^{-1}$. The O VI doublet is well fit by a weak, narrow, single component absorption profile. Ly α absorption at $v = -53 \text{ km s}^{-1}$ shows a similar single component profile. There is some evidence of weak C III 977 at the same velocity as the Ly α , but we could not obtain a satisfactory fit, and better quality data are needed to confirm this claim.

$z_{\text{abs}} = 0.24532$ (Figure 6; Table 6)—There are two weak O VI components in this system, with a single weak, broad H I component. There is possible N V present, corresponding the red-most O VI component, but the weak N V 1242 line is totally obscured by Galactic C IV 1548, and we regard this identification as uncertain.

$z_{\text{abs}} = 0.26656$ (Figure 7; Table 6)—This absorber is relatively simple, with well-aligned, single-component O VI and H I lines. The O VI and H I line centroids differ by only 4 km s^{-1} , and the good alignment permits us to derive gas temperature and non-thermal broadening of $\log T = 4.9$ and $b_{nt} = 24.4 \text{ km s}^{-1}$ respectively. Sec 5.2 has the details of this derivation.

3.5. HE 0226-4110

The STIS spectrum of HE 0226-4110, at $z_{\text{abs}} = 0.495$, allows us to search for intervening O VI absorbers in the interval $0.1154 < z_{\text{abs}} < 0.4707$. We identified O VI doublets at $z_{\text{abs}} = 0.20702, 0.32639, 0.34034, 0.35525$. This line of sight has also been studied by Savage et al. (2005), who focused on the $z_{\text{abs}} = 0.20702$ system, and Lehner et al. (2006) who studied the full path length using STIS and FUSE data.

$z_{\text{abs}} = 0.20702$ (Figure 8; Table 7)—The strong absorber at $z_{\text{abs}} = 0.20702$ has associated H I, C III 977, Si III 1206 and N V. The O VI 1037 transition differs from the single-component structure seen in O VI 1031, which is probably a result of bad pixels in the O VI 1037 region. We measure only a lower limit on $N(\text{H I})$; the Ly α and Ly β transitions are saturated, while the Ly γ line is contaminated by hot pixels. Si III 1206 has two components blueward of the fiducial O VI position, which roughly correspond to the saturated C III 977 line. The N V lines are weak, and uncertain. (Savage et al. 2005) detected Ne VIII aligned with the O VI absorption in FUSE data. They show this system is likely collisionally ionized, which is consistent with the single broad-component in O VI that we observe.

$z_{\text{abs}} = 0.32639$ (Figure 9; Table 7)—We tentatively identify an O VI doublet at $z_{\text{abs}} = 0.32639$ as the only system in our sample that shows no sign of H I absorption. Both O VI lines are well fit by a single doublet model, while the position of any putative Ly α line is in the red-most portion of the STIS wavelength coverage, making the data noisier than the O VI region, as can be seen in Figure 9. Fixing the redshift and expected Doppler parameter from the O VI profile, we set an upper limit on the H I column density $N(\text{H I}) < 12.5$. No other transitions are present in this system. We note that Lehner et al. (2006) do not report identifications for either lines (see e.g. their Figure 3). We also note that the O VI 1037 line is detected at low significance (only 2σ), and emphasize that caution is required interpreting this system as H I free. We suggest that further observations would be very valuable to confirm this system, and whether it is H I free.

$z_{\text{abs}} = 0.34034$ (Figure 10; Table 7)—The O VI 1037 line in this system is contaminated by an unidentified metal line at $v = -26 \text{ km s}^{-1}$, which is excluded from the fit. The Ly α line aligns well with the O VI absorption, but is in a poor-quality region of the spectrum, and the agreement between the Ly α and Ly β profiles is poor. A weak, narrow C III 977 line is also detected, which aligns well with the O VI and main H I component. The Doppler parameter of the C III line, $b_{\text{C III}}$, is significantly smaller than that of the O VI component. This may be explained in several ways: the C III line is not real—possible but unlikely, given its precise alignment with the O VI and H I positions; the O VI Doppler width is over-estimated, either by unresolved components, or due to noise in the

profile; finally, the O VI and C III absorption may arise in physically distinct gas clouds. For the well-aligned O VI and H I components, we calculate $\log T = 4.0$ and $b_{nt} = 16.5 \text{ km s}^{-1}$. Sec 5.2 has the details of this calculation.

$z_{abs} = 0.35525$ (Figure 11; Table 7)—There is only weak O VI and H I at $z_{abs} = 0.35525$, with both transitions precisely aligned. The O VI 1031 line shows a weak contaminating component or feature, although it is too weak to be detected in the O VI 1037 transition if it is real. We fit this component as a contaminating H I line, and the resulting model is a good fit to both O VI transitions. As with the $z = 0.34034$ system, the Ly α profile is quite noisy, but the H I 1215, 1025 regions are fit to within the noise. The resulting H I position is closely matched to the O VI redshift. Using this close match, we derive gas temperature $\log T = 4.3$ and non-thermal broadening $b_{nt} = 22.2 \text{ km s}^{-1}$; see Sec 5.2.

3.6. HS 0624+6907

The QSO HS 0624+6907 at $z_{qso} = 0.370$ offers a path-length for O VI absorption $0.1222 < z_{abs} < 0.3464$. We detect two O VI absorbers, at $z_{abs} = 0.31796, 0.33984$.

$z_{abs} = 0.31796$ (Figure 12; Table 8)—This absorber is seen in only three lines—O VI 1031, 1037 and Ly α ; Ly β is not present. The Ly α and O VI positions are offset ($15 \pm 5 \text{ km s}^{-1}$). The O VI 1031 line shows evidence of some warm or noisy pixels.

$z_{abs} = 0.33984$ (Figure 13; Table 8)—The significance of the O VI in this system is very weak. It meets our formal definition of a significant O VI 1031 line, and an O VI 1037 profile that is consistent with the O VI 1031 transition. We thus accept this system, noting that the O VI doublet is uncertain. Other transitions are clearly present, with strong H I, and possibly weak N V. The Ly α line is saturated and the fit is sub-optimal in the red wing, but good fits are possible to the Ly β , Ly γ and Ly δ lines. The Ly β profile is partly blended with another line, whose identification is uncertain—if this contaminant is Ly α , the expected Ly β line is at a low enough wavelength that it would not be detected in the noisy STIS data. The blended portion of the spectrum is excluded from our fits. There is a very weak, broad line at the expected position of N V 1238, but is too weak to be confirmed in the N V 1242 transition.

3.7. PG 0953+415

Along the line of sight to PG 0953+415 ($z_{qso} = 0.239$), we can detect O VI absorption in the range $0.1144 < z_{abs} < 0.2163$. A single system is detected, at $z_{abs} = 0.14232$, which has been previously discussed by Tripp & Savage (2000).

$z_{abs} = 0.14232$ (Figure 14; Table 9)—This strong O VI absorber falls in a noisy part of the STIS spectrum of PG 0953+415. The O VI 1037 line is stronger than expected, based on the O VI 1031 line strength, but this may be due to noise in the spectrum. Ly α is present, and well aligned with the O VI, but we are unable to obtain the gas temperature, $\log T$, and b_{nt} , since $b_{O VI} > b_{H I}$; see Sec 5.2 for further discussion. Due to noise in the Ly β portion of the spectrum, and blending of the Ly β profile with the QSO host H I 949 line at $z = 0.2335$, we fit only the zero-velocity H I component. There is a

hint of C II 1334, but it is very weak and uncertain. This system has been discussed by Tripp & Savage (2000).

3.8. PG 1116+215

The PG 1116+215 ($z_{qso} = 0.1765$) sightline has a single O VI absorber detected at $z_{abs} = 0.13847$ from the available path-length between $0.1144 < z_{abs} < 0.1536$.

$z_{abs} = 0.13847$ (Figure 15; Table 10)—Previously analysed by Sembach et al. (2004) this absorber has noisy O VI due to the low STIS efficiency at the observed wavelength ($\lambda_{O VI 1031} = 1174.8 \text{ \AA}$). Strong, saturated H I absorption is observed. Well-aligned metal lines of Si II, Si III, Si IV, C II, N II and possibly N V, are all observed. The Ly α, β lines in our STIS data are heavily saturated, and we cannot simultaneously provide a good fit to both H I lines. Using a curve-of-growth analysis and the weak Lyman-limit, Sembach et al. (2004) measured $\log N(\text{H I}) \sim 16.2$ for this absorber. They also concluded that photoionization models at a single ionization parameter, or collisionally ionization models at a single temperature, cannot explain all the metal lines observed.

3.9. PG 1216+069

The STIS data for PG 1216+069 ($z_{qso} = 0.3313$) allow us to search for O VI doublets in the range $0.1309 < z_{abs} < 0.3078$. We detect only a single intervening O VI absorber, at $z_{abs} = 0.28232$.

$z_{abs} = 0.28232$ (Figure 16; Table 11)—The only O VI system we detect towards PG 1216+069, this absorber has very weak O VI absorption, along with very strong, saturated, multi-component H I, allowing us to set only a lower limit on $\log N(\text{H I})$. We also detect saturated C III 977, and strong Si III 1206. In the C III region, we fit only the zero velocity component. Other components may be *bona fide* C III associated with the blue H I component, but this is not clear. Precise knowledge of the H I component positions would be valuable for determining this.

3.10. PG 1259+593

The good quality STIS data for the line-of-sight PG 1259+593 ($z_{qso} = 0.4778$) allow us to search for weak absorbers over a large path-length $0.1144 < z_{qso} < 0.4533$. We detect two O VI systems at $z_{abs} = 0.21950, 0.25981$. This sightline has also been studied by Richter et al. (2004).

$z_{abs} = 0.21950$ (Figure 17; Table 12)—This absorber contains two principle O VI components, both of which are well resolved. The blue component suffers from several bad pixels, which were excluded from the fitting regions. The H I components are aligned with the O VI, although the stronger component is saturated even in the noisy, higher order H I 949 transition. The blue edge of the Ly β profile blends with Galactic Si II 1250, but does not affect our fitting. We detect weak Si III 1206 and saturated C III 977, both aligned with the zero velocity O VI component. Richter et al. (2004), who studied all the systems on this sightline, measured $\log N(\text{H I}) = 15.2$.

$z_{abs} = 0.25981$ (Figure 18; Table 12)—The multi-component absorber at $z = 0.25981$ has two main O VI components: a narrow component at -44 km s^{-1} separation from the broad zero-velocity component. The best

fit H I profile has two components, well aligned with the O VI components. We discount the reality of a putative weak Si III 1206 transition at $\sim +40 \text{ km s}^{-1}$. We attempted to derive $\log T$ and b_{nt} for both components (Sec 5.2), but were only successful only for the O VI/H I pair at -44 km s^{-1} . The zero-velocity O VI/H I component pair has $b_{\text{O VI}} > b_{\text{H I}}$, and is discussed further in Sec 5.2. For the component at $v = -44 \text{ km s}^{-1}$, we measure $b_{\text{nt}} = 13.9 \text{ km s}^{-1}$ and $\log T = 4.5$.

3.11. PHL 1811

The PHL 1811 ($z_{\text{qso}} = 0.1917$) sightline contains a single O VI absorber at $z_{\text{abs}} = 0.15786$ in the available range $0.1144 < z_{\text{abs}} < 0.1690$. Jenkins et al. (2005) have studied this sightline, focusing on the LLS at $z_{\text{abs}} = 0.0809$. $z_{\text{abs}} = 0.15786$ (Figure 19; —This O VI system is very weak. The O VI 1031 line is obvious, but the O VI 1037 line is detected at only $\sim 2\sigma$. Nevertheless, the data show a profile very consistent with the stronger line of the doublet, and the fit to both lines is good. Further, this system is blueward of the Galactic Ly α line, so the O VI 1031 line cannot be ascribed to Ly α absorption. The H I in this system is harder to quantify. There are two components at the expected position for Ly α at this redshift. Both are well fit, but the narrow component is conspicuous given the broad nature of the O VI. Our fits are consistent with those of Tripp et al. (2008), but further investigation reveals the narrow component to be O I 1302 in the $z = 0.0809$ Lyman-limit system (LLS) (Jenkins et al. 2005). Our fit parameters for the narrow component agree well with measurements of Jenkins et al.. Further, there is no corresponding Ly β feature, which would be expected if the narrow component were H I. The broad Ly α component is too weak for Ly β absorption to be detectable. The broad O VI and H I components are well aligned, and we derive $\log T = 5.1$ and $b_{\text{nt}} = 40.5 \text{ km s}^{-1}$ (Sec 5.2). This is the only system for which we derive a temperature greater than 10^5 K , and even at this temperature, O III and O IV dominate the ionization state of Oxygen by several orders of magnitude in CIE models. Both species, however, have absorption lines which are shortward of the Lyman limit for the $z = 0.0809$ LLS, and so cannot be observed.

3.12. PKS 0312–77

The data for the PKS 0312–77 ($z_{\text{qso}} = 0.223$) allow a path-length for our doublet search $0.1241 < z_{\text{abs}} < 0.1999$. We detect the strongest O VI absorber in our survey in these data, at $z_{\text{abs}} = 0.20275$, which is part of a partial LLS. $z_{\text{abs}} = 0.20275$ (Figure 20; Table 14)—The STIS spectrum of the sightline toward PKS 0312–77 was obtained under proposal id 8651 (PI Kobulnicky). This line of sight contains the strongest O VI absorber of our entire sample: a partial Lyman Limit System at $z_{\text{abs}} = 0.20275$ with $15.9 < \log N(\text{H I}) < 18.4$, which is confirmed by a brief inspection of a FUSE spectrum. This system has two groups of components, each having a complex structure. The main component group has strong, broad O VI absorption and covers the range $-100 \lesssim v \lesssim 100 \text{ km s}^{-1}$, while the weaker group shows evidence of weak O VI ($-300 \lesssim v \lesssim -100 \text{ km s}^{-1}$).

Fitting for this absorber was complicated by the fact that many components are saturated, particularly in stronger transitions such as Ly α, β , C III 977 and Si III 1206. In general, we used weaker, low ion transitions (typically N II and C II) to fix the redshifts of the components (excluding O VI), and initialized fits with fixed redshift, and initial b -value and column density guided by weaker absorbers. Degeneracies and poorly constrained parameters naturally result from fitting saturated absorbers; these are indicated by large formal parameter errors, and the fit values are typically indicative of lower limits only.

For the main component group, we fit each species separately. Five components were first identified from low the ion transitions C II 1036, N II 1038 and Si II 1193, 1260, which all show the same structure. These redshifts were fixed and fits performed. The O VI line, while probably requiring more than one component for the measured breadth, shows little evidence of individual component structure, and a single component provided adequate fits. Only three H I transitions are present in the STIS data, all of which are strongly saturated, resulting in mostly $N(\text{H I})$ lower limits. Si II transitions are well fit, except for Si II 1190, which shows possible contamination from Galactic C I* 1190 at the red side, and Galactic C I 1190 at the blue side. The stronger Si III 1206 and Si IV transitions show saturation, with data quality at Si IV deteriorating markedly due to dropping STIS sensitivity (Si IV is at the extreme red end of the wavelength coverage). S II shows weak absorption with a different profile than other low ions—only the two strongest components in the main body of the absorber are present; better quality data would be valuable to confirm that this detection is correct, since the weaker S II 1259 transition is barely detected. For C II, the $\lambda 1036$ line is well fit, but the $\lambda 1334$ line suffers from the same decrease in sensitivity as Si IV, and is poorly fit, as is the strong C III 977 transition. N II is well fit; in the blueshifted part it is strongly saturated. Blueward of this saturated N II absorption we see Galactic O I 1301 at $\sim -380 \text{ km s}^{-1}$, and at $\sim 140 \text{ km s}^{-1}$ we see Galactic Si II 1304. Finally, N V is present in multiple components, but very weak, and we use only the stronger N V 1238 region for the fitting. Figure 21 shows the predicted profile of the N V 1242 region, based on the fits.

3.13. PKS 0405–12

PKS 0405–12 ($z_{\text{qso}} = 0.5723$) is the highest redshift QSO in our sample, allowing a path-length to search for O VI absorbers $0.1241 < z_{\text{abs}} < 0.5478$. We detect four O VI systems, at $z_{\text{abs}} = 0.15597, 0.18291, 0.36333, 0.49514$. This line of sight has also been studied previously by Chen & Prochaska (2000); Prochaska et al. (2004, 2006) $z_{\text{abs}} = 0.16697$ (Figure 22; Table 15)—The PKS 0405–12 sightline has been studied by Prochaska et al. (2004), and the partial Lyman-limit system at $z = 0.167$ by Chen & Prochaska (2000). The system has strong, saturated H I, and two O VI components—one broad and strong; one weak and narrow. Prochaska et al. (2004) estimate $\log N(\text{H I}) = 16.45$ from an analysis of the flux decrement shortward of the 912 \AA Lyman-limit in FUSE data for this sightline.

The STIS data exhibit strong lines of Si II, Si III, Si IV, C II, N II and O I, some of which appear saturated. In general, the low ion transitions are well aligned, and details are given in Table 15. Due to the heavily saturated H I lines, only the weak O VI feature at -110 km s^{-1} can be matched well with H I absorption components, and the resulting parameters $b_{nt} = 7.0 \text{ km s}^{-1}$ and $\log T = 3.7$ are derived in Sec 5.2.

$z_{abs} = 0.18291$ (Figure 23; Table 15)—The absorber at $z_{abs} = 0.18291$ consists of two separate components, separated by $\sim 90 \text{ km s}^{-1}$, both of which are reported in Prochaska et al. (2004). In our STIS data, we have only the Ly α line corresponding to these absorbers (Ly β blends into the Galactic Ly α trough), which is heavily saturated. We thus derive only lower limits to $\log N(\text{H I})$, consistent with Prochaska et al. (2004). The two O VI components are also well fit, despite the O VI 1031 line appearing on the red edge of the Galactic Ly α absorption.

$z_{abs} = 0.36333$ (Figure 24; Table 15)—This system has a well-fit O VI doublet, and corresponding noisy H I profile. Ly α is the only H I transition we detect, but it is marred by hot pixels in the data, so our resulting measurements are uncertain. Further, the Ly α line lies very close to the Galactic C I 1656, blending with the fine structure C I* 1657.38 line. Lacking the detection of Ly β , we cannot obtain reliable $\log N(\text{H I})$. We also detect weak C III. $z_{abs} = 0.49514$ (Figure 25; Table 15)—Prochaska et al. (2004) present a brief analysis of the absorber at $z_{abs} = 0.49514$. At such a high redshift, the Ly α line is redshifted out of the STIS bandpass, and the Ly β and Ly γ transitions are weak and noisy. Both O VI lines are contaminated by hot pixels. In the region of the O VI 1037 line, Galactic C IV 1538 falls at $\sim -90 \text{ km s}^{-1}$. Inspection of the C IV 1542 line shows that it does not significantly affect the O VI line. C III is detected at $v = 0 \text{ km s}^{-1}$, as are offset O III 832 and O IV 787. Both the O III and O IV transitions also show a component at $\sim 90 \text{ km s}^{-1}$. While there is no associated H I with these components at $v = 90 \text{ km s}^{-1}$, the exact alignment of both transitions argues that the absorption is real (as opposed to, say, weak H I). Due the noise in the data, we could not obtain an acceptable fit to the H I lines and we were forced to fix the H I doppler-parameter. Higher quality data would be very valuable for this system, both to obtain an accurate H I column density, and confirm the assumed doppler parameter for H I.

3.14. PKS 1302–102

We searched the STIS data for PKS 1302–102 ($z_{qso} = 0.2784$) for O VI absorbers in the range $0.1183 < z_{abs} < 0.2558$, detecting two close absorbers at $z_{abs} = 0.22565, 0.22744$. This sightline has also been studied by Cooksey et al. (2008).

$z_{abs} = 0.22565$ (Figure 26; Table 16)—As with the H 1821+643 absorber pair, these absorbers at $z_{abs} = 0.22565$ and $z_{abs} = 0.22744$ along the PKS 1302–102 sightline are separated by only $\Delta v = 440 \text{ km s}^{-1}$. Also similar to the previous example, this absorber pair consists of a strong and weak system, with the weaker system at a slightly higher redshift (although in this case, the difference is far less dramatic). The system at $z_{abs} = 0.22565$ consists of two, well defined O VI

components separated by 28 km s^{-1} . Both O VI components have matching H I absorption, detected primarily in Ly α . The two strong lines at the expected positions of the N V doublet are obviously unrelated Ly α absorbers. The temperature and non-thermal broadening can be determined for only the $v = 0 \text{ km s}^{-1}$ component ($\log T = 4.4; b_{nt} = 12.5 \text{ km s}^{-1}$), since the H I position for the component at $v = -28 \text{ km s}^{-1}$ has been fixed to that of O VI in our fitting; see Sec 5.2 for details.

$z_{abs} = 0.22744$ (Figure 27; Table 16)—The weaker of the two close O VI absorbers towards PKS 1302–102, this system has only very weak transitions of O VI 1031, 1037 and Ly α . The O VI 1031 line is close to, but unaffected by, a strong Ly α absorption line at $z = 0.4224$. Both species are well aligned, and suitable for temperature analysis in Sec 5.2. We derive $\log T = 4.2$ and $b_{nt} = 10.7 \text{ km s}^{-1}$.

3.15. Ton 28

The Ton 28 ($z_{qso} = 0.3297$) line of sight hosts only one O VI absorber at $z_{abs} = 0.27340$ in the available path-length $0.1231 < z_{abs} < 0.3059$.

$z_{abs} = 0.27340$ (Figure 28; Table 17)—The system towards Ton 28 contains strong H I absorption, and only weak O VI. The O VI 1031 line is detected at $> 3\sigma$ significance, while the O VI 1037 is only $\sim 2.5\sigma$. The Ly α absorption line is saturated, and blended with Galactic C IV 1548. Comparison of the Galactic C IV 1548 and 1550 lines shows that the full Ly α profile is blended, not just the red wing (which is apparent in Figure 28). The Ly β and Ly γ lines allow us to obtain a good H I fit, and we include the C IV absorption component that is obvious in the Ly α wing. The discrepancy between the Ly α data and fit profile is can be ascribed to the C IV blending. No other associated transitions are detected. The alignment of the H I and O VI positions makes this system useful for our temperature analysis in Sec 5.2. We have derived $\log T = 4.5$ and $b_{nt} = 20.2$.

4. COMPARISON WITH OTHER WORK

As noted in Sec 1, two similar contemporaneous studies have been conducted by other groups (Tripp et al. 2008; Danforth & Shull 2008). While differences exist in the selection of O VI systems in the different samples there is typically good agreement in measured quantities for common systems. Here we specifically address systems reported by (Tripp et al. 2008) that are not accepted by our selection criteria. In general, this is a difference between performing a *blind* search for the O VI doublet, and looking for one of the doublet lines in previously identified systems (e.g. Ly α absorbers). This associated Ly α technique accepts cases in which one or other of the O VI doublet lines is masked by strong absorption from ISM or IGM lines at a different redshift. Other systems simply fall outside our wavelength range or are identified in different data (e.g. the O VI doublet is identified in FUSE spectra).

We only consider absorbers from the Tripp et al. (2008) compilation that are within our wavelength range, but are not recovered in our search. Table 18 summarizes these systems, and we comment on each system below. The O VI 1031 (top) and 1037 (bottom) spectral regions for each system are shown in Figures 29 & 30. Note that

Danforth & Shull (2008) have also recently conducted a similar survey using both STIS and FUSE data. Finally, where our sample has common systems with the samples of Tripp et al. (2008) and Danforth & Shull (2008), we see no marked differences in the measured total column densities, or the component b -values and column densities where similar component structures are fitted.

4.1. *3C 351.0*

$z = 0.21811$ —This system shows broad absorption at the expected position of both O VI doublet members, but is rejected because acceptable fits could not be obtained; the line strengths of the putative doublet members are inconsistent at the $3 - 4\sigma$ level, with O VI 1037 stronger than O VI 1031. There is a putative Ly α absorber at this redshift, but its velocity is inconsistent with the O VI position ($\Delta v \sim 50 \text{ km s}^{-1}$). C III is obscured by Galactic Si II 1190 and no Si III is detectable. It is possible that the O VI 1037 line in this system is a broad Ly α absorber (see e.g. Sembach et al. 2004). We concur with Tripp et al. (2008) that higher S/N observations would be very valuable to firmly establish the nature of this system.

$z = 0.22111$ —This system is not considered because the O VI 1031 position is clearly blended with heavily saturated Galactic Si II 1260 absorption. Ly α and Si III 1206 are present at the expected wavelengths; C III 977 blends with Si II 1193 at $z = 0$.

4.2. *H 1821+643*

$z = 0.12143$ —There is strong Ly α absorption at $\sim -80 \text{ km s}^{-1}$ from the nominal position of this system, but our STIS data are far too noisy to detect O VI absorption ($S/N \approx 2 - 3$ in this region), which is reported by Tripp et al. (2008) in FUSE data. The strong absorption at the O VI 1037 position for this redshift is Ly δ at $z=0.225$ (Tripp et al. 2001).

$z = 0.21331$ —We initially considered this system, but rejected it due to mis-matched line strength ratio. The O VI 1037 is stronger than the O VI 1031 line, and the strength ratio is $R_{\text{O VI}} = 0.77 \pm 0.14$. As noted by Tripp et al. (2000), the region of the O VI 1037 line contains a strong Galactic S II 1259 at a velocity $v \simeq +100 \text{ km s}^{-1}$ with respect to the absorber redshift, and a weaker Galactic S II 1259 feature at $\sim +30 \text{ km s}^{-1}$. This weaker component partially blends with the putative O VI 1037 line. The weaker component is also seen in S II 1253, and is likely associated with the intermediate-velocity cloud (IVC) in the Milky Way known as the IV arch (Kuntz & Danly 1996).

4.3. *HE 0226-4110*

$z = 0.42670$ —The data show a strong O VI 1031 line in this candidate, but there is no corresponding O VI 1037 line (the $\lambda 1037$ position does contain a narrow absorption spike due to noise, which is reflected in the error array). Ly α is redshifted out of the STIS bandpass and there is no Ly β . Galactic Si IV 1393 blends with the expected position of C III 977, and there is also no Si III 1206. We conclude that this system is not real.

4.4. *PG 1216+069*

$z = 0.26768$ —O VI 1037 blends with the heavily saturated Ly β line from the absorber at $z = 0.28232$, and hence this system cannot meet our criteria for a doublet search.

4.5. *PG 1259+593*

$z = 0.31972$ —We do not detect the O VI 1037 line in this system, although there is a single-pixel negative noise spike (which is reflected in the error array). A model based on the putative O VI 1031 line is not consistent with the data in the $\lambda 1037$ region. The red wing of the O VI 1037 region blends with a weak ($\sim 20 \text{ mÅ}$) unidentified line

4.6. *PG 1444+407*

$z = 0.22032$ —The O VI 1031 line blends with Galactic S II 1259. The $z = 0$ S II line exhibits the same structure in the S II 1253 transition, confirming its Galactic nature. Shallow, broad Ly α may be seen, but the O VI 1037 is very weak and uncertain.

4.7. *PHL 1811*

$z = 0.13240$ —At the observed wavelength of this system ($\lambda_{\text{obs}} = 1168.5 \text{ Å}$), the spectrum is quite noisy. We detect a strong O VI 1031 line, and at higher wavelengths the saturated, offset Ly α line is easily detected in higher S/N data. We do not, however, see evidence of an O VI 1037 line, and thus reject this system.

4.8. *PKS 0312-77*

$z = 0.15890$ —The data for the PKS 0312-77 sightline is quite noisy, especially in the low-wavelength region about the O VI 1031 position. We see a well-fit O VI 1031, but this same profile bears no resemblance to the data in the expected region of O VI 1037. Multi component Ly α is also seen, but the lack of O VI 1037 absorption leads us to reject this system.

$z = 0.19827$ —As with the lower redshift system described above, we detected Ly α (saturated in this case) and broad O VI 1031, but no evidence of O VI 1037. There is no correspondence in the data between O VI 1031 and O VI 1037 regions, and the profile fit from the O VI 1031 region is a poor fit to O VI 1037 region.

4.9. *PKS 0405-12*

$z = 0.36156$ —Initially detected in our doublet search, and published by Prochaska et al. (2004), there is considerable mis-match between the O VI 1031 and O VI 1037 regions. Ly α is uncertain, but there may be a weak line in the wing of the strong ($N(\text{H I}) = 15.1$) Ly α line at $z = 0.3608$. Due to the profile mismatch, we are unable to confirm this system.

4.10. *PKS 1302-102*

$z = 0.19159$ —This system is another example that we are unable to confirm due to lack of O VI 1037 absorption. A line at the position of O VI 1031 is present, as is saturated Ly α , and possibly Si III 1206. Given the strength of the apparent O VI 1031 line ($\sim 62 \text{ mÅ}$), we should expect to detect any O VI 1037 line, but no significant absorption exists, and the O VI 1031 profile fit is a poor descriptor of the data in the O VI 1037 region. The independent

work of Cooksey et al. (2008) confirms this result; those authors report Ly α and O VI,1031, but do not detect O VI,1037 (see their Table 3).

4.11. *Ton 28*

$z = 0.13783$ —A strong line at the position of O VI 1031 is seen in this absorber, but no corresponding O VI 1037 is seen. At such low wavelengths, however, this is hardly surprising—our STIS spectra have $S/N < 3$ per pixel at the position of O VI 1037. A profile fit to the O VI 1031 line does not follow the data in the O VI 1037 region. Ly α is detected as part of a stronger, saturated Ly α system.

5. PHYSICAL PROPERTIES OF IONIZED GAS SELECTED BY OVI ABSORPTION

Having identified a sample of O VI absorbers, and related transitions, we now consider these absorbers in detail. We begin by matching individual absorption components of O VI and H I within an absorber. These components trace physically distinct gas clouds, and we consider first the global properties of these components. With the sample of absorption components well-aligned in velocity space, we derive the gas temperature and non-thermal broadening, and examine whether the temperatures are consistent with a collisional ionization origin. We also consider the ionization state of the O^{5+} -bearing gas using photoionization models. We close with a brief comment on the lack of O VI-only systems.

5.1. $N(O\text{ VI})$ vs $N(H\text{ I})$ for Individual Components

To consider any interpretation of the O^{5+} -bearing gas, we must determine whether the different species observed in the absorbers arise from the same gas. It is well established from very high resolution studies of the ISM that absorbers can be resolved into multiple (even many) individual absorption components ($\Delta v < 1 \text{ km s}^{-1}$) (e.g. Welty et al. 1996, 1999). Since these components will trace physically distinct gas clouds, it is at this component level that we must assess the physical nature of the gas. To define well-matched components, we compare the positions of the O VI and H I components in each absorber. The motivation for this matching is to constrain the temperature of the O^{5+} -bearing gas, a subject to which we will return in the following sections. In principle, highly ionized species such as N V would be the ideal candidate to compare to O VI in deriving physical conditions, in particular the gas temperature. N V peaks in CIE at $\log T = 5.25$ (Sutherland & Dopita 1993), so occupies the same temperature range as O VI. Conversely, H I is orders of magnitude more abundant, and so is much more likely to result in a good component match. We therefore attempt to match all O VI components with corresponding H I components. If the two component positions are equal to within their 2σ positional uncertainties (to a maximum of the STIS resolution— $6-7 \text{ km s}^{-1}$) we consider them related.

In Figure 31 we plot, for all well-matched components, the O VI column density as a function of the neutral hydrogen column density (c.f. Figure 19 of Tripp et al. 2008). It is not surprising that no points lie in the upper left part of this plot since: they would require high metallicity *and* optimum ionization parameter, and; we

see little evidence of a class of systems lacking (or with weak) H I (See Section 5.4). The lower portion of the plot is empty due to a selection effect; in most of the survey, our detection limit is $W_r \gtrsim 30 \text{ mÅ}$ which corresponds to $\log N(O\text{ VI}) \gtrsim 13.5$.

A range of physical conditions may be used to explain any particular point on this plot, since the ionization parameter and metallicity are degenerate. Nevertheless, it is worthwhile considering the range of conditions which are allowed by the data. In this vein, we have overplotted two sets of model photoionization curves: models for a variable ionization parameter at fixed metallicity; and, varying metallicity at fixed $\log U$. The dot-dashed line shows our "fiducial" condition of gas at peak ionization parameter and $1/10^{th}$ solar metallicity. Since $N(O\text{ VI})$ peaks for fixed density and metallicity at $\log U = -0.2$, any increase or decrease in $\log U$ will act to shift this line to the lower right (i.e. $N(H\text{ I})$ will be larger at fixed $N(O\text{ VI})$), an effect that is clear in Figure 32. What, then, of the points above this line? Under the assumption of photoionization equilibrium, we then infer that these systems *must* have higher metallicity than our canonical $1/10^{th}$ solar value. The dashed line shows the model curve for $\log U = -1.2$; $[M/H] = 1.0$ and hence, at fixed $[M/H] = 1.0$, the data allow a range of ionization parameters of ~ 1 dex. If we instead consider the variation in the points as solely a function of metallicity at fixed (optimal) ionization parameter, we obtain the bounds delimited by the crosses and square-dots, and a range of metallicities of ~ 1.7 dex.

It is immediately apparent that the data do not follow the same global trend as the model curves shown. Although we cannot determine a zero-point for the model curves, due to the degeneracy between metallicity and $\log U$, the trend is nevertheless valid, and we should expect a variety of metallicities and ionization conditions in the absorbers. The scatter in the observations of $N(O\text{ VI})$ vs $N(H\text{ I})$ can thus be understood as due to scatter in the metallicity and ionization state of the gas⁷.

The case of the 3C 351.0 absorber at $z = 0.31659$ (open squares) is interesting, since the O VI and H I clearly separate into three individual components. No other species are detected in the STIS band. If we posit a physical connection, based on the proximity of the components, we might expect similar conditions for each gas cloud. The three components are shown as open squares in Figure 31. It is clear that no single set of ionization and metallicity conditions can explain all the components, yet the temperatures do not admit of a collisional origin (see Sec 5.2). Likely we are simply seeing, for a constant flux of ionizing photons, density variations along the line of sight. By contrast, we would require variations of ~ 1.0 dex to explain the observations by metallicity variations alone.

5.2. Gas Temperature

In the previous discussion, we have assumed that the matched components arise from photoionized gas. Is this assumption justified? Having identified components of two different species that likely arise from the same gas phase, we can use the Doppler parameters to derive an es-

⁷ Other factors such as length scale, and varying redshift will also play a role here.

time of the gas temperature, which are related through the relation $b^2 = b_{nt}^2 + 2kT/m$, where b_{nt}^2 is the non-thermal component to the Doppler parameter (i.e. turbulence, bulk motion etc), and k , T and m are the Boltzmann constant, temperature and atomic mass as usual. The two equations thus determine both the gas temperature and the non-thermal line broadening, and this well-established fact has been used in the past to determine gas temperatures of absorbers (e.g. Chen & Prochaska 2000; Tripp & Savage 2000). It is also clear that, in the absence of a turbulent component, the Doppler parameters will be related through the square-root of the ratio of atomic masses. The distribution of O VI and H I b -values for well-aligned absorption components is shown in Figure 33. The solid lines bound two limiting cases. At one extreme, for $b_{nt} = 0$, we have simply that $b_{HI} = 4 \times b_{OVI}$. The upper boundary in Figure 33 shows the other limiting case, where $b_{HI} = b_{OVI}$. Formally, we should not see absorbers above this limit, since that regime is non-physical. In practice, any absorbers in this area imply either unresolved components, or that the O^{5+} and H^0 gas is unrelated—either physically distinct⁸, or in a separate phase of a multi-phase system. While we have three components in our sample that lie above this limit, all are consistent with $b_{HI} = b_{OVI}$ at the 1σ level.

Gas in collisional ionization equilibrium with $T \gtrsim 2 \times 10^5$ implies $b_{HI} \gtrsim 60 \text{ km s}^{-1}$. It is immediately apparent that few of our components satisfy this criteria. Including a non-thermal contribution to the b -value will further lower the implied temperature (or conversely, increase the implied Doppler parameter). This simple argument indicates that collisional ionization is not the dominant ionization mechanism. It does not, however, rule out collisionally ionized systems, since it is conceivable that weak, collisionally ionized systems may not contain a detectable amount of neutral hydrogen (i.e. by considering *only* systems with well-aligned O VI/H I components, we may be biased against systems in CIE). To quantify this statement, we examined with *Cloudy* (version 07.02.01) a simple model of gas in collisional ionization at $\log T = 5.5$ and $1/10^{th}$ solar metallicity. For O VI column densities in the range $\log N = 13.5 - 14.0$ the corresponding H I column density is $\log N \lesssim 13.0$, which will be difficult to detect in our data. We note that while we see no evidence of a population of O VI absorbers lacking H I absorption, we certainly see *components* that are not well matched with H I.

Table 19 gives the temperature and b_{nt} for the well-matched components defined above. The first three columns identify the absorber and component. The measured H I and O VI Doppler parameters are recalled here for reference. The derived gas temperature and error are given, along with the non-thermal contribution to the Doppler parameter, and the resulting thermal line-width for both H I and O VI. Finally, for comparison, we give the gas temperature we would have derived from b_{OVI} had we assumed $b_{nt} = 0$, which is strictly a formal upper-limit. Only one system lies above $\log T = 5.0$: the absorber towards PHL 1811 at $z = 0.15786$, and even in this case, the data are ambiguous (see Sec 3.11). It is clear, however, that for all cases in which we can de-

rive a gas temperature, the temperature is well below the $\log T = 5.5$ expected for CIE conditions. It may also be possible that we are observing gas that is radiatively cooling out of equilibrium. Gnat & Sternberg (2007) have shown that O VI can be present at temperatures well below those expected in equilibrium models, since the cooling time is much shorter than the recombination time. These non-equilibrium effects are only important for enriched gas (solar metallicity or higher), however, and are unlikely to be a dominant effect for our sample.

In three cases we could not determine $\log T$ and b_{nt} , because $b_{OVI} > b_{HI}$; these cases are listed in Table 19 by “...”. Note also, that these are the same three components in Fig 33 which lie above the $b_{OVI} = b_{HI}$ boundary. All are consistent with b_{nt} -dominated systems. Alternatively, this lack of correspondence between the H I and O VI line widths may indicate that either the assumption of the absorption being physically related is not correct for these systems, or there are unresolved absorption components. In other words, *if* both absorption components arise from the same gas, then we require that $1/4 < b_{OVI}/b_{HI} < 1$, since $m_O = 16 \times m_H$. The upper limit comes from a state where the b -values are dominated entirely by b_{nt} (i.e. $b_{HI} = b_{OVI}$), while the lower limit is the pure thermal case, and the b -values are simply related through the square-root of the ratio of their respective atomic masses. Similar limits can be trivially written down for all other pairs of species.

It is worth emphasizing, at this stage, that these measurements are dependent on several critical factors: a) the resolution of the spectrograph must be sufficient to resolve the lines in question, reinforcing our decision to rely solely on STIS E140M data with superior resolution (e.g. the FUSE FWHM is $\sim 20 - 25 \text{ km s}^{-1}$, but our *median* b_{OVI} is $\sim 21 \text{ km s}^{-1}$); b) Further, the resolution must be sufficient to resolve multiple absorption components and possible blending; c) the non-thermal contribution to the Doppler parameter *must* be considered, since it dominates b_{tot} in most cases. As Table 19 clearly demonstrates, if we do not take this into account, most of our absorbers would be consistent with the coronal temperature range $10^5 - 10^7 \text{ K}$, and we could easily mis-interpret these as WHIM absorbers. This point has also been made by (Tripp et al. 2008), while Danforth & Shull (2008) derive only upper limits to the temperature using b_{HI} .

5.3. Ionization State of O^{5+} Bearing Gas

Before considering the ionization conditions of the O^{5+} -bearing gas, we first inspect the results of a typical photoionization model of low-density gas. We use similar models when considering individual systems below, each tailored to the specific conditions of the individual absorber. Figure 32 shows the ionization state for the most commonly observed species as a function of the ionization parameter, $\log U \equiv \log(n_\gamma/n_H)$, where n_γ and n_H are the volume densities of ionizing photons ($h\nu > 13.6 \text{ eV}$) and hydrogen, respectively. The model was calculated for a slab of gas at with neutral hydrogen column density $\log N(H I) = 15.0$ and metal abundance $1/10^{th}$ the solar value. The gas temperature was constrained to be $\log T > 4.0$, although in practice this con-

⁸ In which case the component alignment is purely coincidental.

straint has little effect⁹. Ionizing radiation comes from an updated version of the Haardt & Madau (1996) spectrum included with *cloudy*¹⁰, at redshift $z = 0.25$ (the median redshift of our sample). Since the spectrum of the UV background is fixed, and the relative intensity is set at a fixed redshift, only changes in the density affect the ionization parameter. Thus at high densities, there are fewer ionizing photons per atom, and lower ionization states predominate. At lower densities (higher $\log U$), there are more ionizing photons for a given atom, and higher ionization states may be ionized. Inspection of the curves in Figure 32 shows that O VI can be observed over a wide range of conditions, especially if one considers that metallicity may vary over a 1 – 2 dex range. Thus, unlike with CIE where O VI occupies a very narrow temperature range, simply detecting O VI is not enough to determine the ionization conditions.

The column density ratios predicted by the *Cloudy* models are not sensitive to the adopted value of $\log N(\text{H I})$ in the optically thin regime, although the absolute column densities would obviously be lower for a lower gas column. A comparison between models with solar and $1/10^{\text{th}}$ solar metallicity shows that the column density ratios are unaffected by metallicity effects in the regime $\log U > -4.0$, which corresponds to densities $\log n_{\text{H}} < -1.6$. This is well away from $\log U = -0.2$, where O VI peaks for photoionization models. None of the systems we consider fall into this region of parameter space, so the adopted $[\text{M}/\text{H}] = -1.0$ for our models should not affect our conclusions.

The detection of multiple metal transitions in an absorber offers a powerful diagnostic of the ionization conditions of the gas, assuming that the metals responsible for the absorption are co-spatial. By comparing the column density ratios for well-aligned transitions with predictions of a model like that in Figure 32, we can place limits on $\log U$; even saturated lines can provide limits in $\log U$. With the ionization parameter determined, we obtain the average volume density of the cloud and using the ionization fraction (from the *Cloudy* output) we can then calculate a length scale for the cloud. These numbers are, however, dependent on the strength of the UV background ionization field, which is uncertain. When relevant in the following analysis, we give a range of parameters for a range of UV background intensities $J_{\nu, 912 \text{ \AA}} = 2 - 7 \times 10^{-23} \text{ erg s}^{-1} \text{ cm}^{-2} \text{ Hz}^{-1} \text{ sr}^{-1}$ (Shull et al. 1999; Scott et al. 2002).

We address several systems below. Many of these systems have already been studied in detail in terms of their ionization conditions, characteristic sizes and/or average densities. In these cases, we do not comment unless we have additional information to add, beyond what has been published. The interested reader is encouraged to see the following references for more information: Savage et al. (2005, HE 0226–4110 $z = 0.20702$); Lehner et al. (2006, HE 0226–4110 $z = 0.34034$); Tripp & Savage (2000, PG 0953+415 $z = 0.14232$); Sembach et al. (2004, PG 1116+215 $z = 0.13847$); Chen & Prochaska (2000, PKS 0405–12 $z =$

0.16703, 0.36333). Note that all our *Cloudy* models assume a solar abundance pattern. If there are significant deviations from this pattern (which may be particularly problematic for C or N), then we will deduce incorrect limits. Hence, the more metal transitions we have for a system, the better our results will be.

H 1821+643; $z = 0.22496$ —This system was first examined by Tripp et al. (2000), who report N for O VI absorbers on this sightline, but were primarily interested in the cosmological mass density of O VI, and did not discuss the ionization condition of individual absorbers. As noted in Sec 3.4 the O VI and Si III Doppler parameters for the $v = 0 \text{ km s}^{-1}$ component are inconsistent with a single phase, since $b_{\text{O VI}} \gg b_{\text{Si III}}$ and $b_{\text{O VI}} \gg b_{\text{C III}}$. For this $v = 0 \text{ km s}^{-1}$ component, we also detect weak Si IV, but no H I components are aligned with the O VI position. The Si III to Si IV column density ratio is consistent with the Si III to C III column density limit, and $\log U \approx -2.1$ ($\log n_{\text{H}} \approx -3.5$). The weaker component at $v \simeq 25 \text{ km s}^{-1}$ also contains saturated C III, Si III and Si IV. This component also falls within the width of the O VI line, but the centroids are significantly different. The nearest H I component to this low-ionization gas is at $v = 15 \text{ km s}^{-1}$, and the relation between the two is unclear. For this low-ion $v \simeq 25 \text{ km s}^{-1}$ component, Si III and Si IV have the same column density, while $\log N(\text{C III})/N(\text{Si III}) \geq 1.0$ dex, both of which are consistent with $\log U \approx -1.4$ ($\log n_{\text{H}} \approx -4.2$). There are no obvious matches to the weak O VI component at $v = 60 \text{ km s}^{-1}$. The mismatch of the broad O VI and low ion Doppler parameters, in addition to the multiple low-ion components falling within the O VI absorption range, argues for a core-halo cloud model, with a hot gaseous halo traced by O VI, surrounding cooler gas traced by lower ionization species.

PG 1216+069; $z = 0.28232$ —Tripp et al. (2005) were the first to publish STIS data of PG 1216+069, but concentrate on the DLA at $z = 0.00632$ associated with the NGC 4261 group, and do not consider this absorber in detail. We detect O VI Si III and saturated C III. The C III, Si III and H I are offset from the O VI position by $\Delta v = 6 - 9 \text{ km s}^{-1}$ to the blue, and its association is unclear. We measure $\log N(\text{C III})/N(\text{Si III}) > 1.3$ which gives the limit $\log U > -2.6$ ($\log n_{\text{H}} \lesssim -2.9$; $L > 5 \text{ kpc}$, where we have folded in the range in J_{ν} into the quoted limits).

PG 1259+593; $z = 0.21950$ —Data for the PG 1259+593 sightline was published by Richter et al. (2004), who report the detection of O III in FUSE data, in addition to O VI, Si III and (saturated) C III metal lines seen in the STIS data. They conclude that the absorber is a multi-phase medium, based on the inconsistency of the Si III data with an ionization parameter derived using O III and O VI. This conclusion is emphasised by our discussion above of the limits placed by the ratio of Doppler parameters. In our STIS data we measure $b_{\text{O VI}}/b_{\text{Si III}} = 1.6 \pm 0.6$ which is inconsistent at the 1σ level with a single gas phase, since $m_{\text{O VI}}/m_{\text{Si III}} = 0.6$ i.e. for these species to arise from the same gas phase, we must have $0.6 < b_{\text{O VI}}/b_{\text{Si III}} < 1.0$, irrespective of the relative contributions of b_{nt} and b_{therm} .

PKS 0312–77; $z = 0.20275$ —While the Lyman limit system at $z = 0.20275$ in the sightline towards PKS 0312–77

⁹ Collisional ionization is not yet significant at these temperatures.

¹⁰ Cloudy denotes this “HM05”.

shows many metal absorption lines, particularly those of low ions, none can be unambiguously matched with the O VI absorption. The main O VI absorption component is very broad compared to other ions; even the highly ionized species like Si IV and N V exhibit a complex multi-component structure that is seen in the low ionization species. It is therefore likely that O VI arises in a different gas phase, or that there are unresolved O VI absorption components.

PKS 0405–12; $z = 0.49514$ —The highest redshift O VI absorber in our survey, this absorber is fit with a single O VI component. We detect O III and O IV at $v = 90 \text{ km s}^{-1}$, but no associated O VI or H I, and we do not consider this component in detail. At $v = -10 \text{ km s}^{-1}$, the data clearly show C III and O IV 787. We discount the O III 832 absorption at $v = -29 \pm 8 \text{ km s}^{-1}$ as too far from the O VI centroid. Prochaska et al. (2004) do not provide a full analysis of this system, referring instead to a future paper which was not forthcoming. From our O VI, O IV and C III measurements, we find $\log U \simeq -0.8 - -1.3$ ($\log n_{\text{H}} \approx -4.0 - -4.5$; $L \approx 12 - 140 \text{ kpc}$).

5.4. Systems lacking H I

In a survey for O VI absorbers, we might expect to find a class of systems that do not contain associated H I. If large-scale galactic winds and superwinds shock-heat metals to a WHIM phase, they may also ionize hydrogen to a level that is not detectable for weak systems (as in the above discussion on CIE systems). Such hot bubbles may exist even without strong winds (Kawata & Rauch 2007). Since we conduct a *blind* search for the O VI doublet, we should be sensitive to the existence of such systems, down to our detection limit, which is approximately 30 mÅ with good data (but see paper I for a better quantification of this, since not all data are of equal quality).

Given the above discussion, it may be somewhat telling that we find no strong evidence for such a class of systems. Our survey contains two system that we suggest are H I free. The $z = 0.32639$ absorber toward HE 0226–4110 (Figure 9) shows no evidence of Ly α or Ly β absorption, although the Ly α region is quite noisy. The upper limit on $N(\text{H I})$ for this system implies $\log[\text{NOVI}/N\text{HI}] \gtrsim 1.1 \text{ dex}$. The $z = 0.22638$ system toward H 1821+643 (Figure 5) shows a single broad H I component significantly offset ($\Delta v = -53 \pm 2 \text{ km s}^{-1}$) from the O VI position. If we posit that this component could hide a weak, aligned H I component, and attempt to force-fit an H I component aligned with the O VI absorption, we obtain $N(\text{H I}) < 12.3$, implying $\log[\text{NOVI}/N\text{HI}] \gtrsim 1.2 \text{ dex}$. Such large column density ratios are well outside the bounds of what is found for the well-aligned components ($-0.75 < \log[N(\text{O VI})/N(\text{H I})] < 0.67$), and imply either strongly enriched gas (super-solar assuming photoionization; See Figure 31), or that the gas is collisionally ionized. Expanded samples of low- z O VI absorbers will be very valuable for determining the fraction of such systems, and their potential as tracers of hot gas.

6. SUMMARY

We have presented a catalogue of O VI absorbers selected from high-resolution HST/STIS echelle data.

Our selection technique followed a blind-search for the O VI 1031, 1037 doublet feature. Relying solely on the presence of the O VI doublet, and the ratio of doublet line strength, we detect 27 O VI absorption systems, independent of other transitions. The statistics of these absorbers were presented in paper I. We note that 16 systems reported in a contemporaneous work by Tripp et al. (2008) do not satisfy our selection criteria and therefore are not included in our sample of 27 absorbers. In cases where only one transition is found or the doublet ratio appears to be inconsistent with model expectations, these authors include the presence of other transitions, such as Ly α absorption, for justifying the identifications of O VI.

In our absorbers, it is common to find multiple absorption components in any given system, corresponding to physically distinct gas structures. By matching these absorption components from different species, we can identify different transitions likely due to the same gas. Under this assumption, we can then derive both the temperature of the gas, and the non-thermal contribution to the Doppler parameter, b_{nt} . This analysis demonstrates that, for well-matched O VI/H I components, gas temperatures are in the range $\log T = 3.7 - 5.0$, well below the temperature range at which O VI is expected to be found in collisional ionization equilibrium ($\log T = 5.5$). We thus advise caution in identifying the O VI absorbers with the hot WHIM gas that simulations predict will contain a significant fraction of the baryons. Our finding based on all available absorbers in the current HST/STIS data archive reaffirms previous findings from studies of individual lines of sight. Future generations of X-ray spectrographs are likely to be necessary to solve this question conclusively.

If galactic winds are the dominant source of O VI formation, shock heating the gas to the WHIM regime, and pushing it out to $\sim 1 \text{ Mpc}$ from galaxies, we may expect to see this in a variety of ways. A class of H I free O VI absorbers may arise, as both the hydrogen and oxygen are ionized in strong winds. We see no evidence of a large number of H I-free O VI absorbers, with only two systems present in our survey. Reasoning that the H I absorption will best trace the local over-density, we compared the velocity difference between our O VI components and the nearest H I component. A wind origin may leave an imprint on the kinematics of the absorbers, manifest as a systematic offset between the H I and O VI positions. We see no such effect (see also comparisons in T08), but this test is likely a weak one. Clearly systematic galaxy redshift surveys around the QSO lines of sight are required to properly address this.

The location of the missing baryons in the low-redshift is clearly an important issue in modern cosmology and astronomy. The WHIM is a leading candidate reservoir for this mass with simulations and suggesting that it contains as much as 50% of all $z = 0$ baryons. While some have claimed that the observations support this view, we argue that caution is required. High-resolution spectra that cover a broad wavelength range are crucial for constraining the ionization, metallicity, and the temperature of the gas involved, and care must be taken to deduce non-thermal broadening mechanisms. If the baryons are to be unambiguously located in the WHIM, further observations are crucial.

This research has made use of the NASA/IPAC Extragalactic Database (NED) which is operated by the Jet Propulsion Laboratory, California Institute of Technology, under contract with the National Aeronautics and Space Administration. C. T. and H.-W. C. acknowledge

support from NASA grant NNG06GC36G. H.-W. C. acknowledges partial support from an NSF grant AST-0607510.

HST(STIS)

REFERENCES

- Burles, S., Nollett, K. M., & Turner, M. S. 2001, *ApJ*, 552, L1
- Burles, S. & Tytler, D. 1996, *ApJ*, 460, 584
- Carswell, B., Schaye, J., & Kim, T.-S. 2002, *ApJ*, 578, 43
- Cen, R. & Ostriker, J. P. 1999, *ApJ*, 514, 1
- . 2006, *ApJ*, 650, 560
- Chen, H.-W. & Prochaska, J. X. 2000, *ApJ*, 543, L9
- Cooksey, K. L., Prochaska, J. X., Chen, H.-W., Mulchaey, J. S., & Weiner, B. J. 2008, *ApJ*, submitted (arXiv:0706:1285)
- Danforth, C. W. & Shull, J. M. 2005, *ApJ*, 624, 555
- . 2008, *ApJ*, 679, 194
- Danforth, C. W., Shull, J. M., Rosenberg, J. L., & Stocke, J. T. 2006, *ApJ*, 640, 716
- Davé, R., Cen, R., Ostriker, J. P., Bryan, G. L., Hernquist, L., Katz, N., Weinberg, D. H., Norman, M. L., & O'Shea, B. 2001, *ApJ*, 552, 473
- Fang, T., Mckee, C. F., Canizares, C. R., & Wolfire, M. 2006, *ApJ*, 644, 174
- Fukugita, M. & Peebles, P. J. E. 2004, *ApJ*, 616, 643
- Gnat, O. & Sternberg, A. 2007, *ApJS*, 168, 213
- Haardt, F. & Madau, P. 1996, *ApJ*, 461, 20
- Heckman, T. M., Norman, C. A., Strickland, D. K., & Sembach, K. R. 2002, *ApJ*, 577, 691
- Jenkins, E. B., Bowen, D. V., Tripp, T. M., & Sembach, K. R. 2005, *ApJ*, 623, 767
- Kawata, D. & Rauch, M. 2007, *ApJ*, 663, 38
- Kuntz, K. D. & Danly, L. 1996, *ApJ*, 457, 703
- Lehner, N., Savage, B. D., Wakker, B. P., Sembach, K. R., & Tripp, T. M. 2006, *ApJS*, 164, 1
- Moos, H. W., Cash, W. C., Cowie, L. L., Davidsen, A. F., Dupree, A. K., Feldman, P. D., Friedman, S. D., Green, J. C., Green, R. F., Gry, C., Hutchings, J. B., Jenkins, E. B., Linsky, J. L., Malina, R. F., Michalitsianos, A. G., Savage, B. D., Shull, J. M., Siegmund, O. H. W., Snow, T. P., Sonneborn, G., Vidal-Madjar, A., Willis, A. J., Woodgate, B. E., York, D. G., Ake, T. B., Andersson, B.-G., Andrews, J. P., Barkhouser, R. H., Bianchi, L., Blair, W. P., Brownsberger, K. R., Cha, A. N., Chayer, P., Conard, S. J., Fullerton, A. W., Gaines, G. A., Grange, R., Gummin, M. A., Hebrard, G., Kriss, G. A., Kruk, J. W., Mark, D., McCarthy, D. K., Morbey, C. L., Murowinski, R., Murphy, E. M., Oegerle, W. R., Ohl, R. G., Oliveira, C., Osterman, S. N., Sahnou, D. J., Saisse, M., Sembach, K. R., Weaver, H. A., Welsh, B. Y., Wilkinson, E., & Zheng, W. 2000, *ApJ*, 538, L1
- Morton, D. C. 2003, *ApJS*, 149, 205
- Norris, J., Peterson, B. A., & Hartwick, F. D. A. 1983, *ApJ*, 273, 450
- Oegerle, W. R., Tripp, T. M., Sembach, K. R., Jenkins, E. B., Bowen, D. V., Cowie, L. L., Green, R. F., Kruk, J. W., Savage, B. D., Shull, J. M., & York, D. G. 2000, *ApJ*, 538, L23
- O'Meara, J. M., Burles, S., Prochaska, J. X., Prochter, G. E., Bernstein, R. A., & Burgess, K. M. 2006, *ApJ*, 649, L61
- Prochaska, J. X., Chen, H.-W., Howk, J. C., Weiner, B. J., & Mulchaey, J. 2004, *ApJ*, 617, 718
- Prochaska, J. X., Weiner, B. J., Chen, H.-W., & Mulchaey, J. S. 2006, *ApJ*, 643, 680
- Rauch, M., Miralda-Escude, J., Sargent, W. L. W., Barlow, T. A., Weinberg, D. H., Hernquist, L., Katz, N., Cen, R., & Ostriker, J. P. 1997, *ApJ*, 489, 7
- Richter, P., Savage, B. D., Tripp, T. M., & Sembach, K. R. 2004, *ApJS*, 153, 165
- Savage, B. D., Lehner, N., Wakker, B. P., Sembach, K. R., & Tripp, T. M. 2005, *ApJ*, 626, 776
- Savage, B. D., Sembach, K. R., Tripp, T. M., & Richter, P. 2002, *ApJ*, 564, 631
- Scott, J., Bechtold, J., Morita, M., Dobrzycki, A., & Kulkarni, V. P. 2002, *ApJ*, 571, 665
- Sembach, K. R., Tripp, T. M., Savage, B. D., & Richter, P. 2004, *ApJS*, 155, 351
- Shull, J. M., Roberts, D., Giroux, M. L., Penton, S. V., & Fardal, M. A. 1999, *AJ*, 118, 1450
- Simcoe, R. A., Sargent, W. L. W., & Rauch, M. 2002, *ApJ*, 578, 737
- . 2004, *ApJ*, 606, 92
- Spergel, D. N., Verde, L., Peiris, H. V., Komatsu, E., Nolte, M. R., Bennett, C. L., Halpern, M., Hinshaw, G., Jarosik, N., Kogut, A., Limon, M., Meyer, S. S., Page, L., Tucker, G. S., Weiland, J. L., Wollack, E., & Wright, E. L. 2003, *ApJS*, 148, 175
- Sutherland, R. S. & Dopita, M. A. 1993, *ApJS*, 88, 253
- Thom, C. & Chen, H.-W. 2008, *ApJ*, in press (arxiv:0801.2380)
- Tripp, T. M., Giroux, M. L., Stocke, J. T., Tumlinson, J., & Oegerle, W. R. 2001, *ApJ*, 563, 724
- Tripp, T. M., Jenkins, E. B., Bowen, D. V., Prochaska, J. X., Aracil, B., & Ganguly, R. 2005, *ApJ*, 619, 714
- Tripp, T. M., Lu, L., & Savage, B. D. 1998, *ApJ*, 508, 200
- Tripp, T. M. & Savage, B. D. 2000, *ApJ*, 542, 42
- Tripp, T. M., Savage, B. D., & Jenkins, E. B. 2000, *ApJ*, 534, L1
- Tripp, T. M., Sembach, K. R., Bowen, D. V., Savage, B. D., Jenkins, E. B., Lehner, N., & Richter, P. 2008, *ApJS*, in press (arXiv:0706.1214)
- Welty, D. E., Frisch, P. C., Sonneborn, G., & York, D. G. 1999, *ApJ*, 512, 636
- Welty, D. E., Morton, D. C., & Hobbs, L. M. 1996, *ApJS*, 106, 533
- Woodgate, B. E., Kimble, R. A., Bowers, C. W., Kraemer, S., Kaiser, M. E., Danks, A. C., Grady, J. F., Loiacono, J. J., Brumfield, M., Feinberg, L., Gull, T. R., Heap, S. R., Maran, S. P., Lindler, D., Hood, D., Meyer, W., Vanhouten, C., Argabright, V., Franka, S., Bybee, R., Dorn, D., Bottema, M., Woodruff, R., Michika, D., Sullivan, J., Hetlinger, J., Ludtke, C., Stocker, R., Delamere, A., Rose, D., Becker, I., Garner, H., Timothy, J. G., Blouke, M., Joseph, C. L., Hartig, G., Green, R. F., Jenkins, E. B., Linsky, J. L., Hutchings, J. B., Moos, H. W., Boggess, A., Roesler, F., & Weistrop, D. 1998, *PASP*, 110, 1183

TABLE 1
SUMMARY OF THE STIS ECHELLE SPECTRA

QSO (1)	z_{QSO} (2)	z_{min} (3)	$z_{\text{max}}^{\text{a}}$ (4)	t_{exp} (5)	PID (6)
3C 249.1	0.3115	0.1222	0.2885	68776	9184
3C 273	0.1580	0.1144	0.1417	18671	8017
3C 351.0	0.3719	0.1309	0.3483	73198	8015
HE 0226–4110	0.4950	0.1154	0.4707	43772	9184
HS 0624+6907	0.3700	0.1222	0.3464	61950	9184
H 1821+643	0.2970	0.1144	0.2741	50932	8165
PG 0953+415	0.2390	0.1144	0.2163	24478	7747
PG 1116+215	0.1765	0.1144	0.1536	39836	8165/8097
PG 1216+069	0.3313	0.1309	0.3078	69804	9184
PG 1259+593	0.4778	0.1144	0.4533	95760	8695
PG 1444+407	0.2673	0.1222	0.2442	48624	9184
PHL 1811	0.1917	0.1144	0.1690	33919	9418
PKS 0312–77	0.2230	0.1241	0.1999	37908	8651
PKS 0405–12	0.5726	0.1241	0.5478	27208	7576
PKS 1302–102 ...	0.2784	0.1183	0.2558	22119	8306
Ton 28	0.3297	0.1231	0.3059	48401	9184

NOTE. — This summary of STIS echelle lines of sight is taken from paper I. It is repeated here for completeness.

^a The maximum redshift is defined for O VI absorbers at velocity separation $> 5000 \text{ km s}^{-1}$ from the background QSO, but the line search is conducted through the emission redshift of the QSO. In this paper we do not consider system inside this 5000 km s^{-1} limit.

TABLE 2
SUMMARY OF O VI ABSORBERS

QSO (1)	z_{abs} (2)	W_r (1031) (3)	$\sigma_{W_r(1031)}$ (4)	W_r (1037) (5)	$\sigma_{W_r(1037)}$ (6)	$R_{\text{O VI}}$ (7)	$\sigma_{R_{\text{O VI}}}$ (8)	$N_{\text{O VI}}$ (9)	$\sigma_{N_{\text{O VI}}}$ (10)
3C 249.1	0.24676	72.1	9.0	31.0	9.0	2.33	0.74	13.9	0.1
3C 273	0.12003	22.4	5.6	21.5	5.6	1.04	0.38	13.5	0.1
3C 351.0	0.31659	232.5	13.8	139.8	13.8	1.66	0.19	14.4	0.1
H 1821+643	0.22498	162.2	6.7	108.5	6.7	1.49	0.11	14.3	0.0
H 1821+643	0.22638	29.8	3.9	19.7	3.9	1.51	0.36	13.5	0.1
H 1821+643	0.24532	53.9	4.9	36.0	4.9	1.50	0.25	13.7	0.1
H 1821+643	0.26656	44.2	4.0	23.7	4.0	1.86	0.36	13.6	0.1
HE 0226–4110	0.20702	165.3	8.9	106.5	8.9	1.55	0.15	14.4	0.1
HE 0226–4110	0.32639	43.0	8.0	15.8	8.0	2.72	1.47	13.6	0.2
HE 0226–4110	0.34034	62.1	6.6	41.5	6.6	1.50	0.29	13.9	0.1
HE 0226–4110	0.35529	45.5	7.8	11.5	7.8	3.96	2.77	13.6	0.2
HS 0624+6907	0.31796	43.7	6.0	26.9	6.0	1.62	0.43	13.7	0.1
HS 0624+6907	0.33984	27.1	8.3	22.5	8.3	1.20	0.58	13.4	0.3
PG 0953+415	0.14232	121.2	22.3	89.1	22.3	1.36	0.42	14.2	0.1
PG 1116+215	0.13846	75.7	16.0	38.0	16.0	1.99	0.94	13.9	0.1
PG 1216+069	0.28232	26.4	5.6	16.9	5.6	1.56	0.61	13.4	0.2
PG 1259+593	0.21950	98.9	7.6	21.1	7.6	4.68	1.73	13.9	0.1
PG 1259+593	0.25981	77.0	8.3	34.1	8.3	2.26	0.60	13.9	0.1
PHL 1811	0.15786	63.5	13.2	39.2	13.2	1.62	0.64	13.9	0.2
PKS 0312–77	0.20275	655.3	20.1	336.5	20.1	1.95	0.13	15.0	0.2
PKS 0405–12	0.16697	360.7	41.4	236.7	41.4	1.52	0.32	14.7	0.1
PKS 0405–12	0.18291	103.7	14.7	77.5	14.7	1.34	0.32	14.2	0.2
PKS 0405–12	0.36333	30.4	4.8	12.4	4.8	2.45	1.02	13.5	0.1
PKS 0405–12	0.49506	212.6	15.6	151.0	15.6	1.41	0.18	14.5	0.1
PKS 1302–102	0.22565	70.9	9.3	64.4	9.3	1.10	0.21	13.9	0.1
PKS 1302–102	0.22744	30.3	5.5	14.4	5.5	2.10	0.89	13.5	0.1
Ton 28	0.27340	25.6	7.0	18.1	7.0	1.41	0.67	13.4	0.2

NOTE. — Redshift of absorbers is generally the position of the strongest component. Equivalent widths are rest-frame mÅ. Column densities are total column density for absorber, taken from component fitting. See individual systems for details.

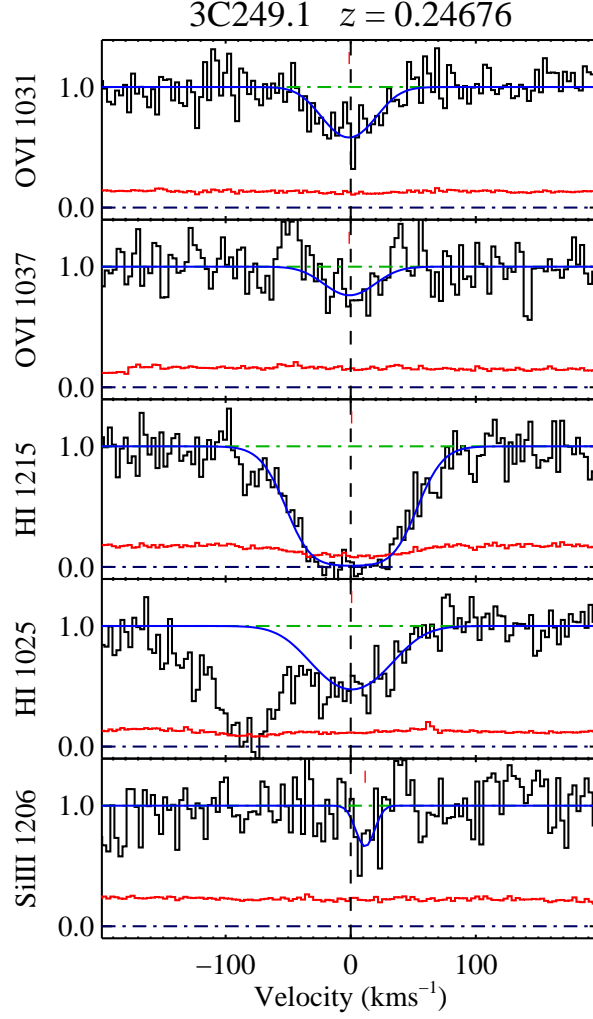


FIG. 1.— 3C 249.1 $z = 0.24676$ —O VI and strong H I are detected in this system. Ly β is blended with what we tentatively assign as Ly α line at $z = 0.0517$. There is a weak and uncertain feature which may be Si III 1206.

TABLE 3
O VI ABSORBER MEASUREMENTS ALONG THE LINE OF SIGHT TOWARDS 3C 249.1

ion	z_{comp}	v km s $^{-1}$	σ_v km s $^{-1}$	b km s $^{-1}$	σ_b km s $^{-1}$	$\log N$ log(cm $^{-2}$)	$\sigma_{\log N}$ log(cm $^{-2}$)	Flag
$z = 0.24676$								
O VI	0.24676	0	0	27.0	3.2	13.9	0.1	...
H I	0.24676	0	1	38.2	1.4	14.4	0.1	...
Si III	0.24681	11	3	9.9	5.6	12.1	0.2	Z

TABLE 4
O VI ABSORBER MEASUREMENTS ALONG THE LINE OF SIGHT TOWARDS 3C 273

ion	z_{comp}	v km s $^{-1}$	σ_v km s $^{-1}$	b km s $^{-1}$	σ_b km s $^{-1}$	$\log N$ log(cm $^{-2}$)	$\sigma_{\log N}$ log(cm $^{-2}$)	Flag
$z = 0.12003$								
O VI	0.12003	0	1	8.6	2.5	13.5	0.1	...
H I	0.12004	3	0	23.2	0.6	13.5	0.1	...

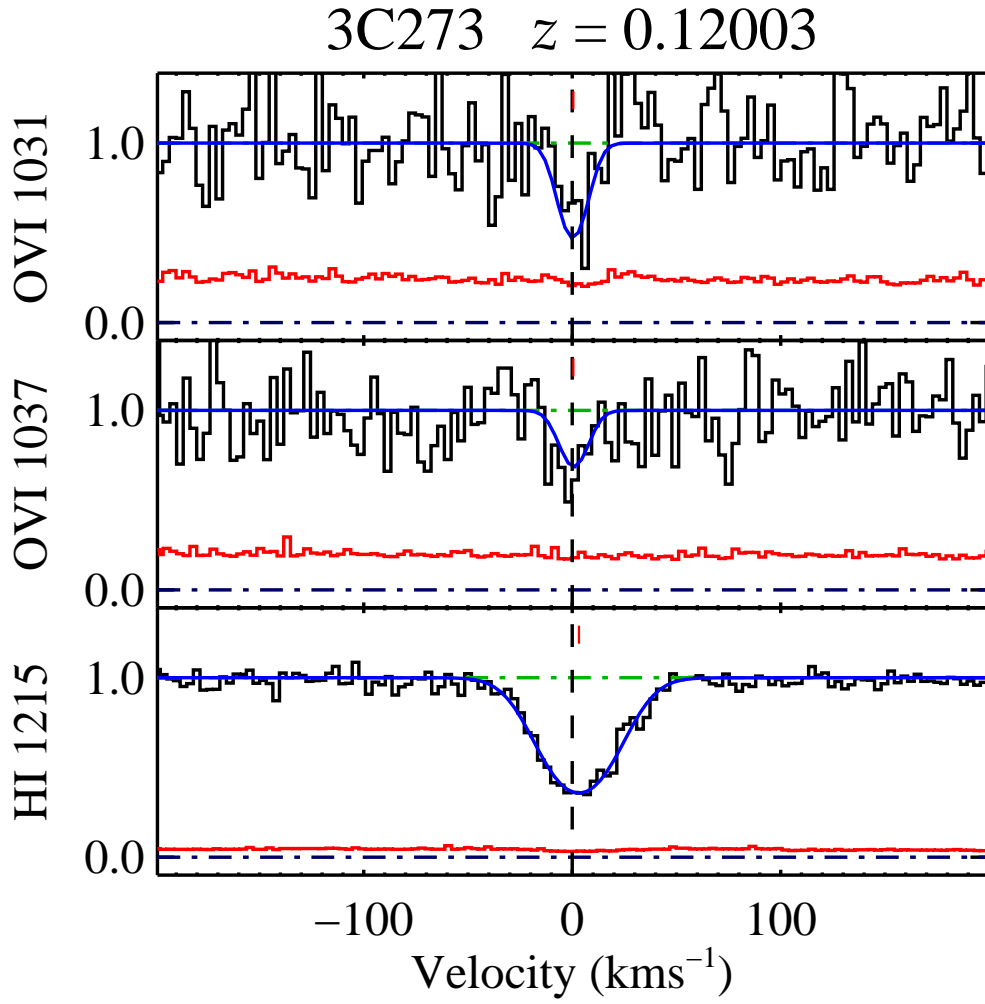


FIG. 2.— 3C273 $z = 0.12003$ —This weak system is detected in only O VI and Ly α . The O VI lines are mismatched in their strengths, but neither can be weak Ly α , since they both lie to the blue of the $z = 0$ Ly α 1215 line.

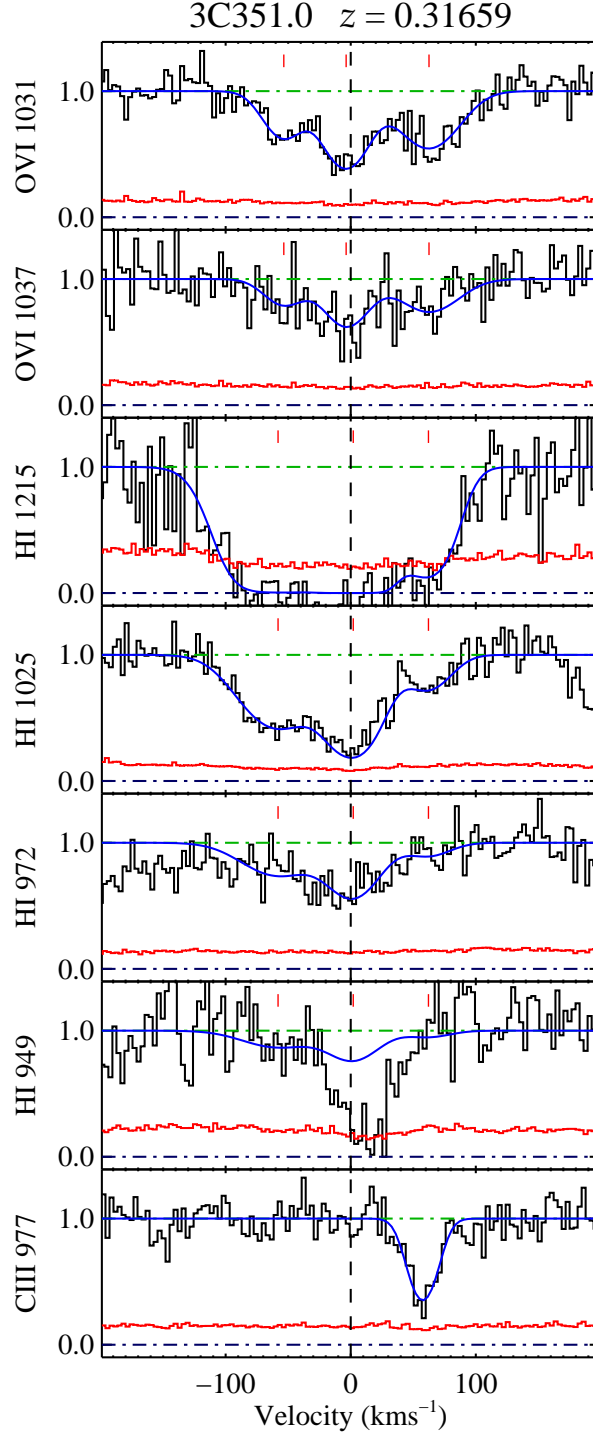


FIG. 3.— 3C351.0 $z = 0.31659$ —Three obvious O VI components are seen in this absorber. Corresponding Ly α absorption is heavily saturated, but Ly β and Ly γ allow us to derive H I column densities and positions. The Ly α components are well matched in position with the O VI absorption. No associated metals are detected in our wavelength range.

TABLE 5
O VI ABSORBER MEASUREMENTS ALONG THE LINE OF SIGHT TOWARDS 3C 351.0

ion	zcomp	v km s ⁻¹	σ_v km s ⁻¹	b km s ⁻¹	σ_b km s ⁻¹	$\log N$ log(cm ⁻²)	$\sigma_{\log N}$ log(cm ⁻²)	Flag
$z = 0.31659$								
O VI	0.31635	-53	4	21.1	5.5	13.7	0.2	...
O VI	0.31657	-3	2	23.3	4.4	14.0	0.1	...
O VI	0.31686	62	3	30.9	4.7	14.0	0.1	...
H I	0.31633	-58	5	37.8	4.8	14.4	0.1	...
H I	0.31660	2	2	26.9	3.8	14.6	0.1	...
H I	0.31686	62	5	23.3	5.8	13.8	0.1	...

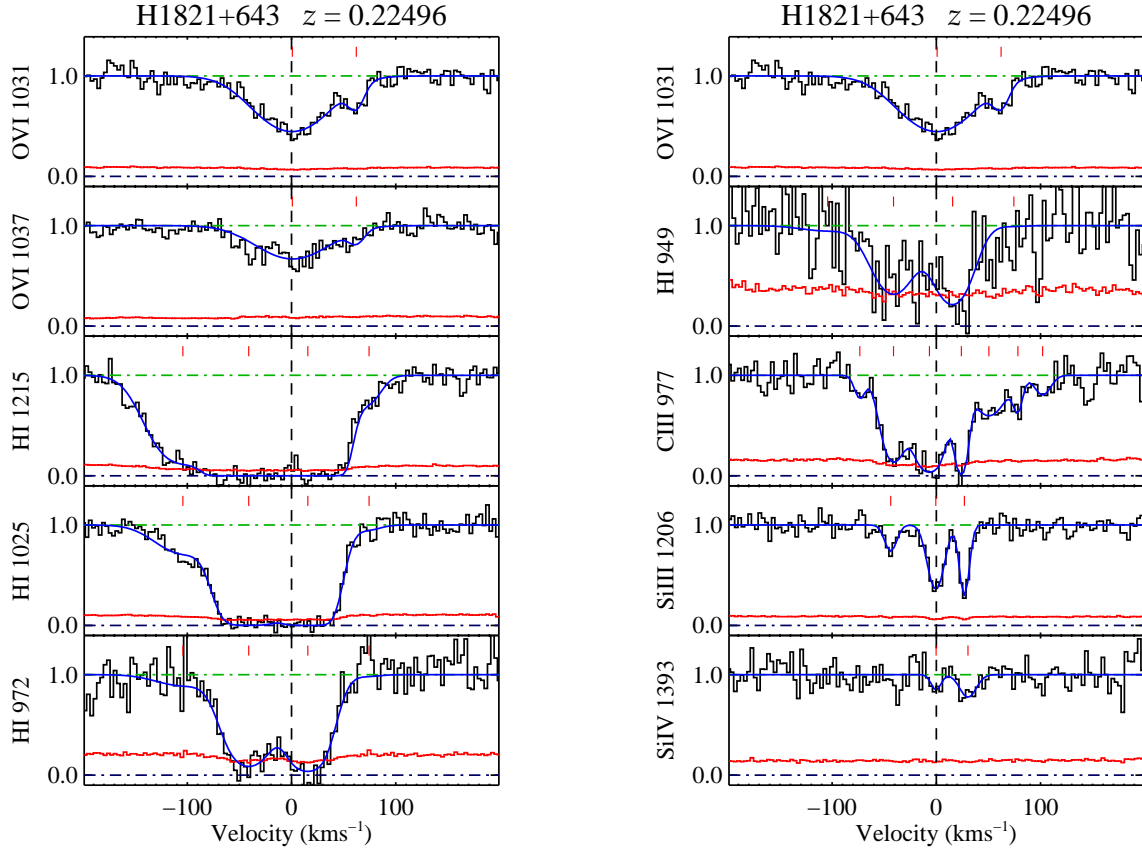


FIG. 4.— H1821+643 $z = 0.22496$ —A strong main O VI absorption component and weaker, offset component are both obvious in this system. Ly α is heavily saturated, but higher order Lyman lines are available. Strong C III and Si III can also be seen.

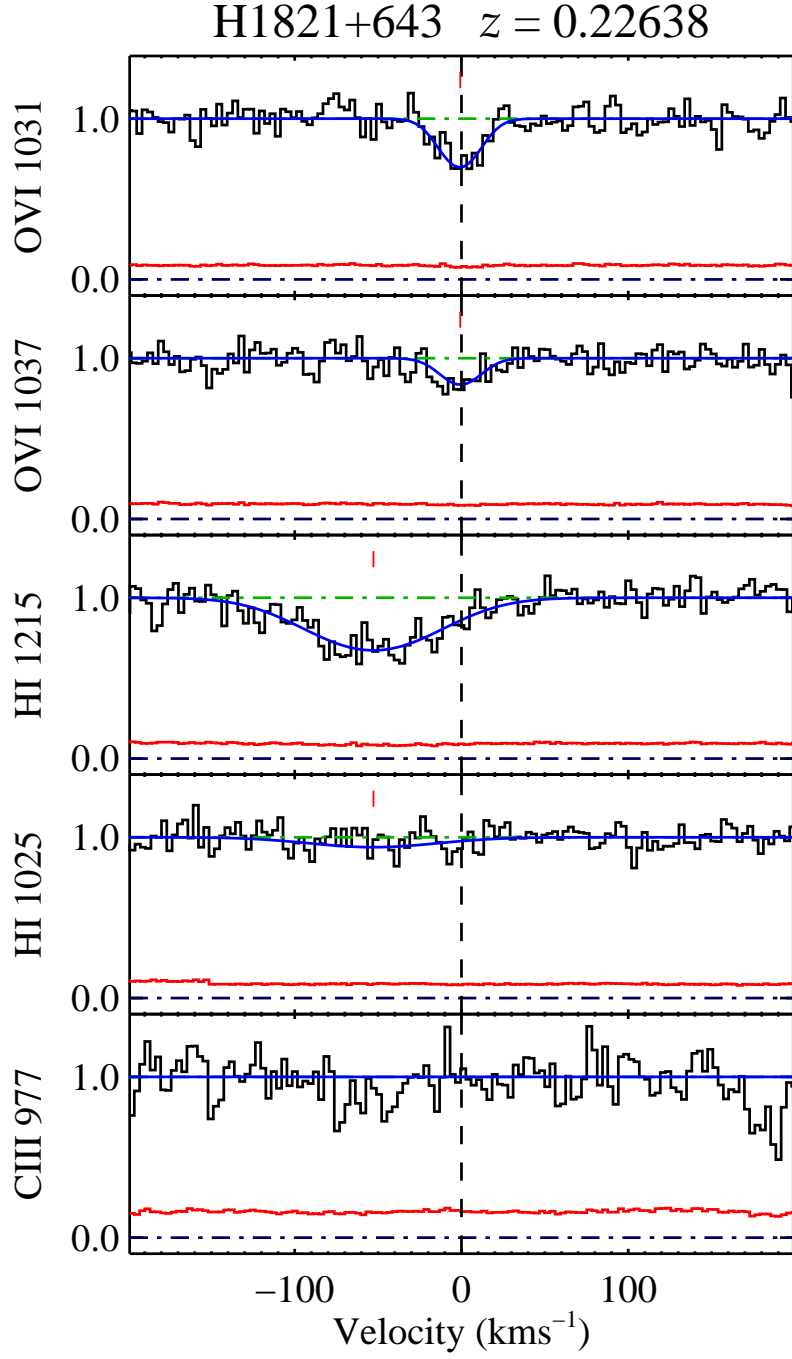


FIG. 5.— H1821+643 $z = 0.22638$ —This system comprises weak O VI absorption, and very broad H I absorption offset from the O VI by -53 km s^{-1} . This absorber is only $\sim 350 \text{ km s}^{-1}$ from the system at $z = 0.22496$.

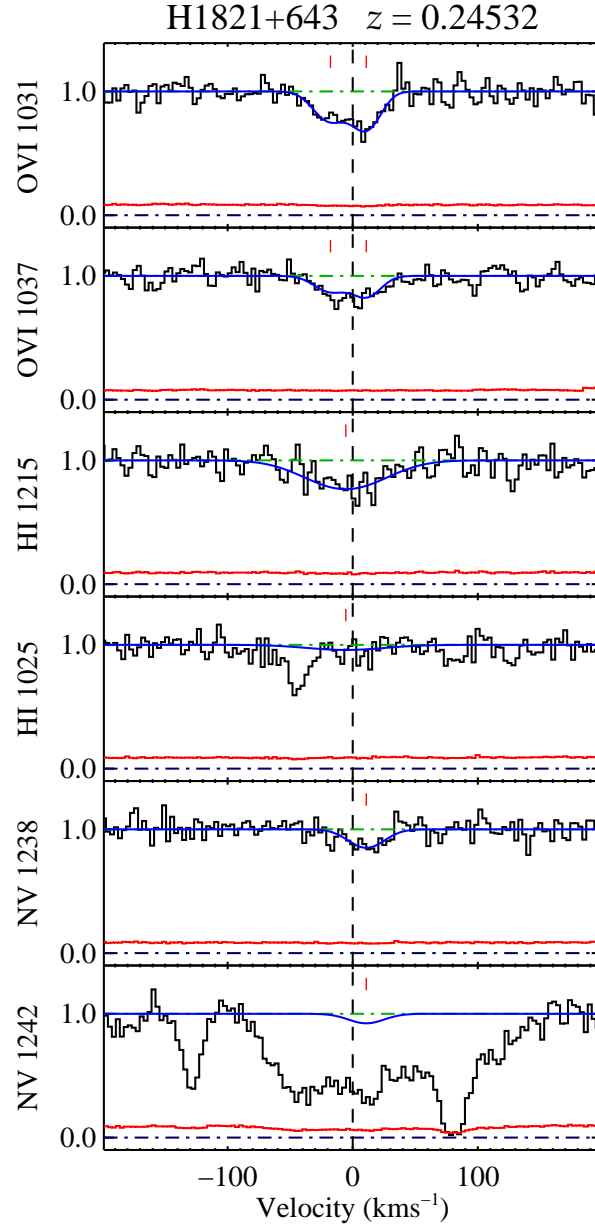


FIG. 6.— H1821+643 $z = 0.24532$ —Two weak O VI components and a corresponding very weak H I absorber are seen in this system. N V 1238 is possibly present, but the N V 1242 line is lost in the Galactic C IV 1548 line.

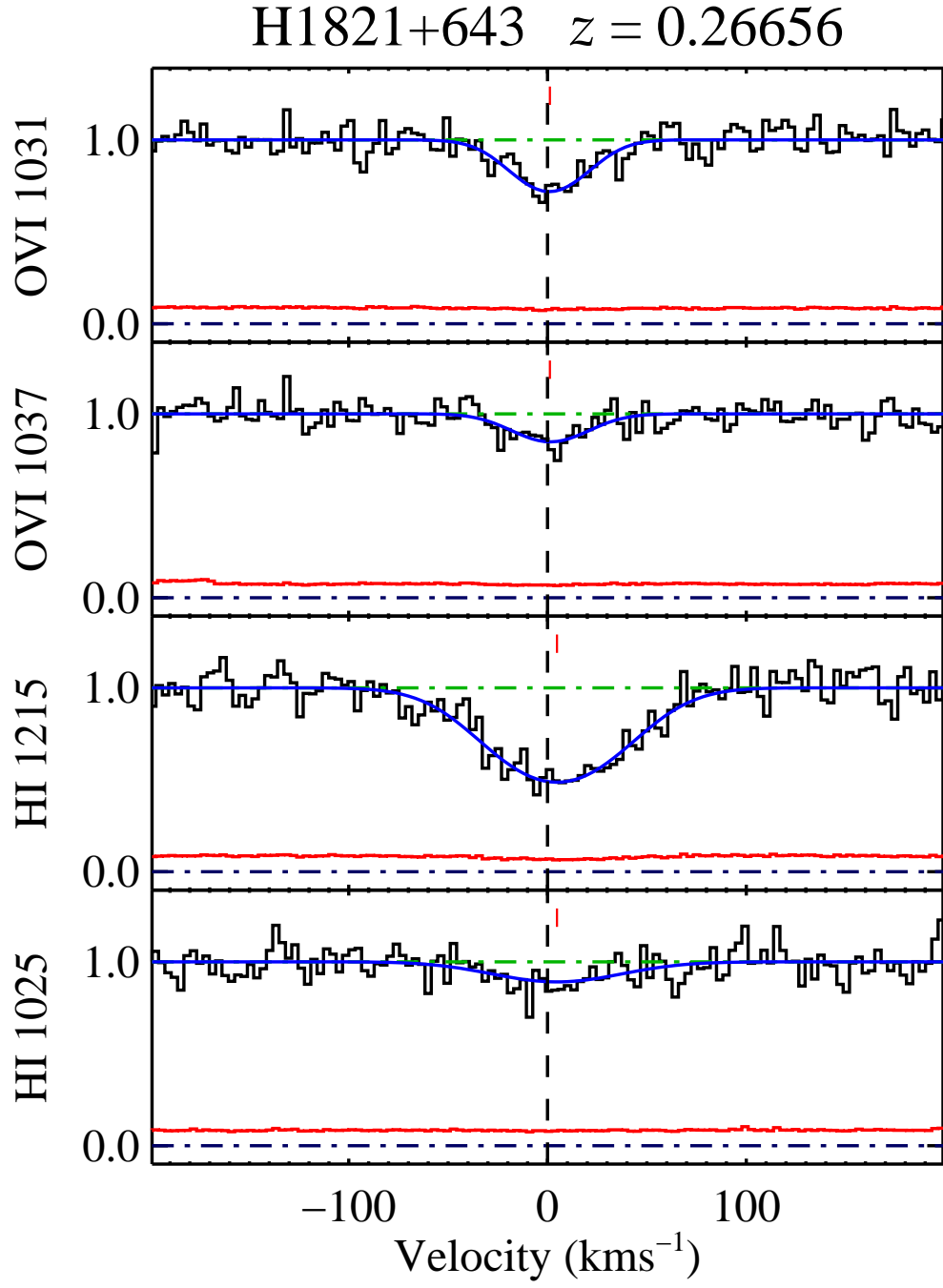


FIG. 7.— H 1821+643 $z = 0.26656$ —This weak system consists of a single O VI and H I component, both well-aligned.

TABLE 6
O VI ABSORBER MEASUREMENTS ALONG THE LINE OF SIGHT TOWARDS H 1821+643

ion	z_{comp}	v km s ⁻¹	σ_v km s ⁻¹	b km s ⁻¹	σ_b km s ⁻¹	$\log N$ log(cm ⁻²)	$\sigma_{\log N}$ log(cm ⁻²)	Flag
$z = 0.22496$								
O VI	0.22496	0	1	45.3	2.0	14.3	0.1	...
O VI	0.22521	62	1	9.6	2.7	13.2	0.1	...
H I	0.22453	-104	4	34.5	3.2	14.0	0.1	...
H I	0.22479	-41	1	24.9	1.8	15.2	...	L
H I	0.22502	15	1	21.6	0.8	15.2	...	L
H I	0.22526	74	4	15.1	5.1	12.8	0.1	...
C III	0.22493	-6	1	15.4	3.0	13.7	...	L
C III	0.22506	23	0	5.2	2.5	13.5	...	L
C III	0.22517	50	4	20.8	12.0	13.0	0.2	Z
C III	0.22528	78	2	4.5	5.0	12.3	0.3	Z
C III	0.22479	-41	1	13.1	2.0	13.4	0.1	...
C III	0.22466	-73	2	5.8	4.5	12.2	0.2	Z
C III	0.22538	102	3	9.7	6.0	12.3	0.2	Z
Si III	0.22496	0	0	9.1	0.8	12.5	0.1	...
Si III	0.22507	26	0	4.5	0.7	12.4	0.1	...
Si III	0.22478	-43	1	6.8	2.1	11.9	0.1	...
Si IV	0.22496	0	3	5.2	5.8	12.0	0.3	Z
Si IV	0.22508	30	2	9.9	4.2	12.4	0.1	Z
$z = 0.22638$								
O VI	0.22638	0	1	16.5	1.8	13.5	0.1	...
H I	0.22616	-53	2	53.1	3.4	13.5	0.1	...
$z = 0.24532$								
O VI	0.24525	-17	4	17.4	4.6	13.4	0.2	...
O VI	0.24536	10	2	15.1	3.5	13.4	0.2	...
H I	0.24530	-5	3	43.2	5.2	13.2	0.1	...
N V	0.24536	10	0	19.4	5.2	13.0	0.1	Z
$z = 0.26656$								
O VI	0.26656	0	1	26.1	2.5	13.6	0.1	...
H I	0.26658	4	1	44.8	1.9	13.6	0.1	...
C III	0.26656	1	0	30.1	0.0	12.2	...	U

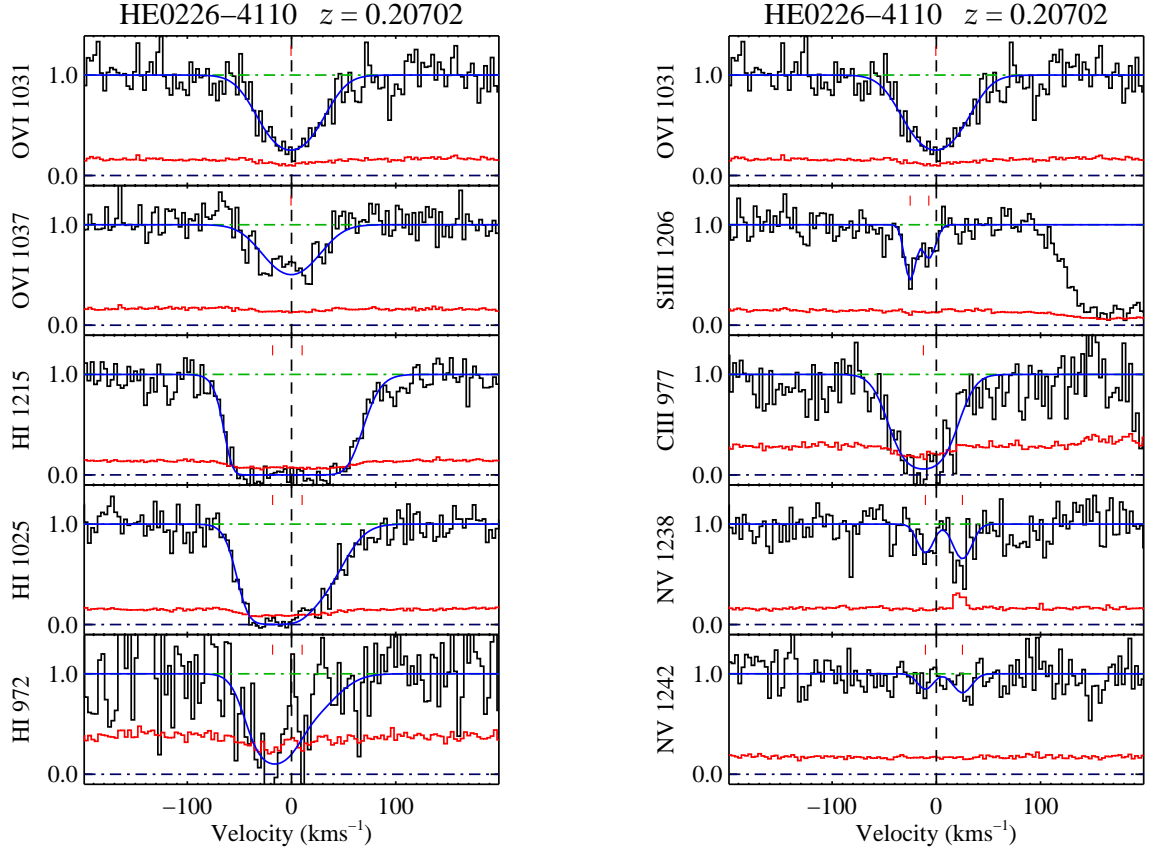


FIG. 8.— HE 0226-4110 $z = 0.20702$ —This strong O VI absorber is also seen in saturated Ly α, β absorption. The Ly γ line is contaminated by hot pixels, making the $N(\text{H I})$ determination uncertain. We see associated Si III, C III and possibly N V absorption.

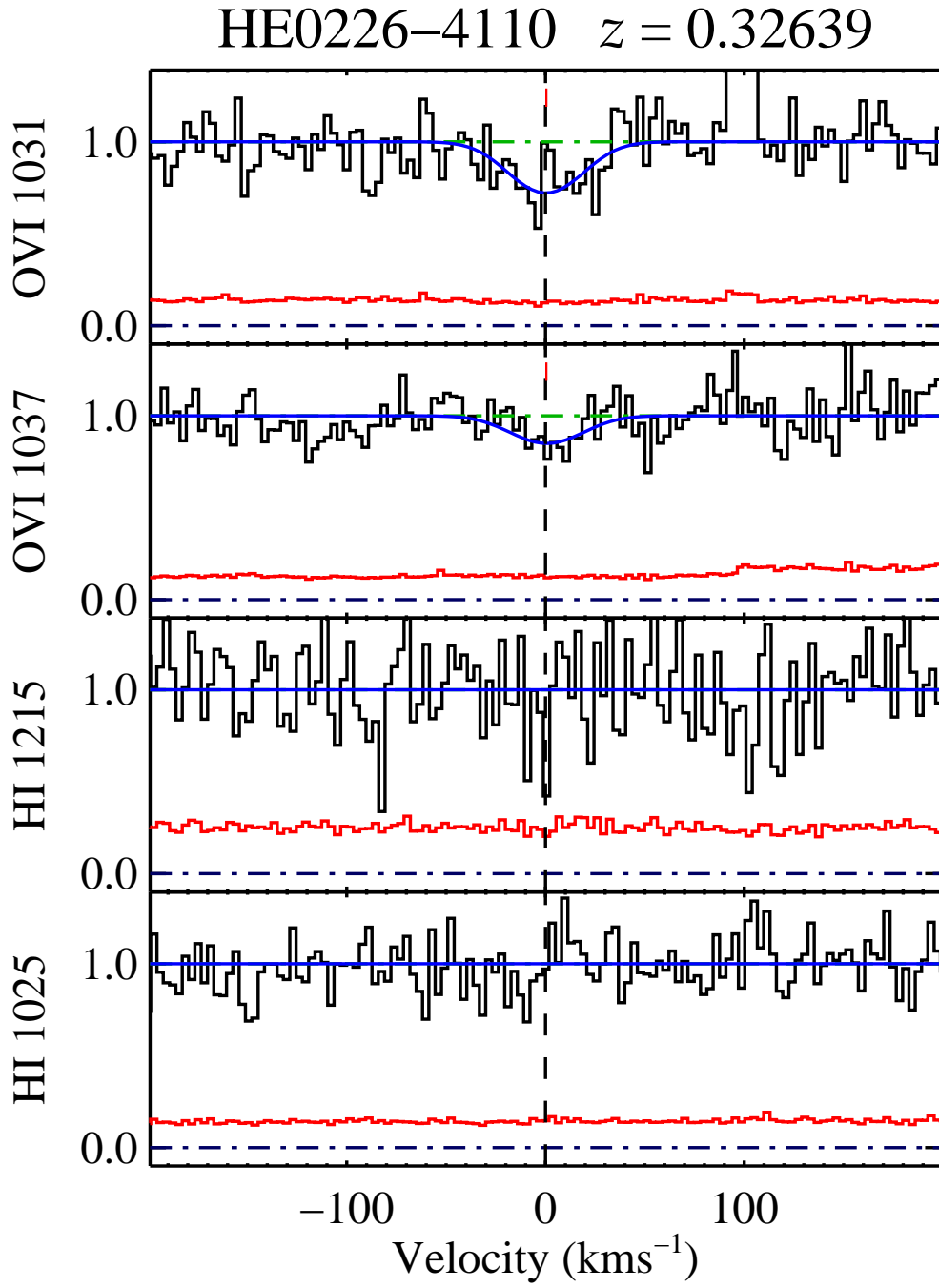


FIG. 9.— HE0226–4110 $z = 0.32639$ —This system is weak and uncertain. It is the only system we detect without corresponding H I absorption. No other transitions are present and correspond to the O VI absorption.

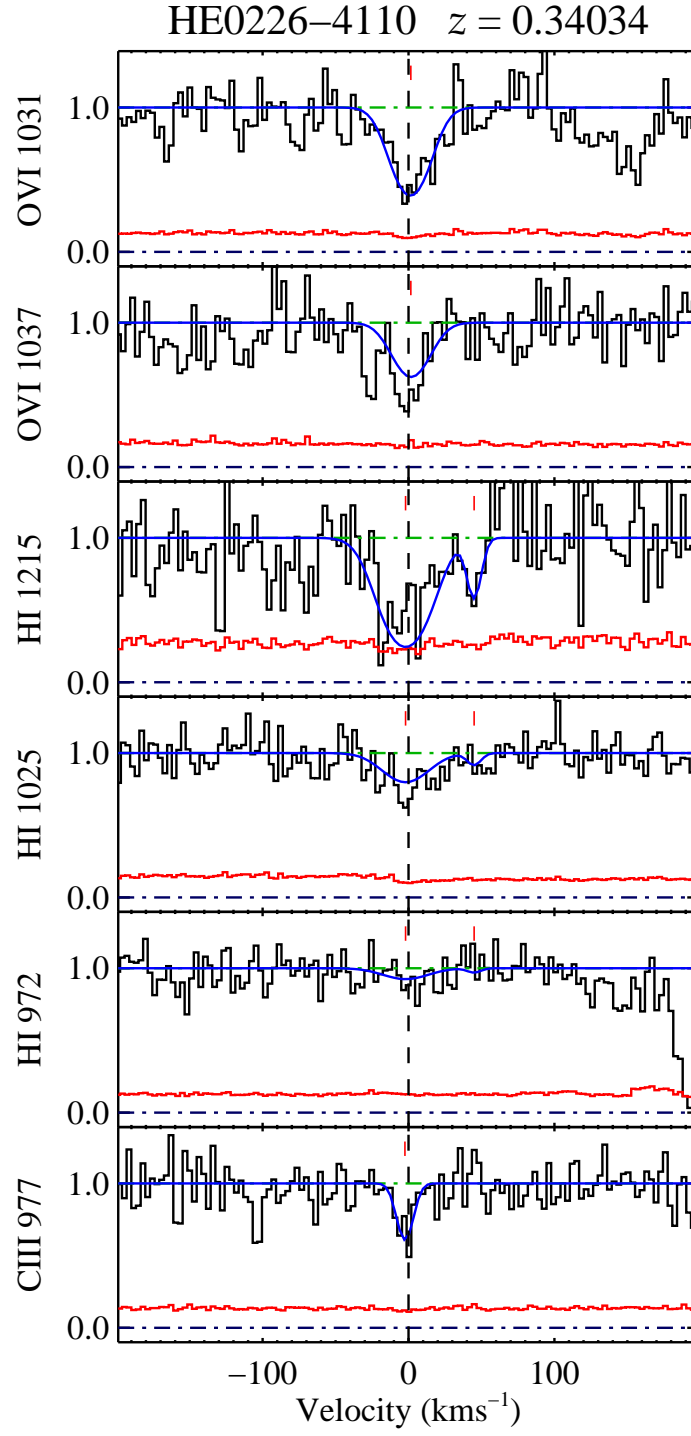


FIG. 10.— HE 0226–4110 $z = 0.34034$ —The O VI 1037 line in this system is contaminated by an unidentified metal line. H I is present, but noisy, and the fit is poor. Weak C III is also detected.

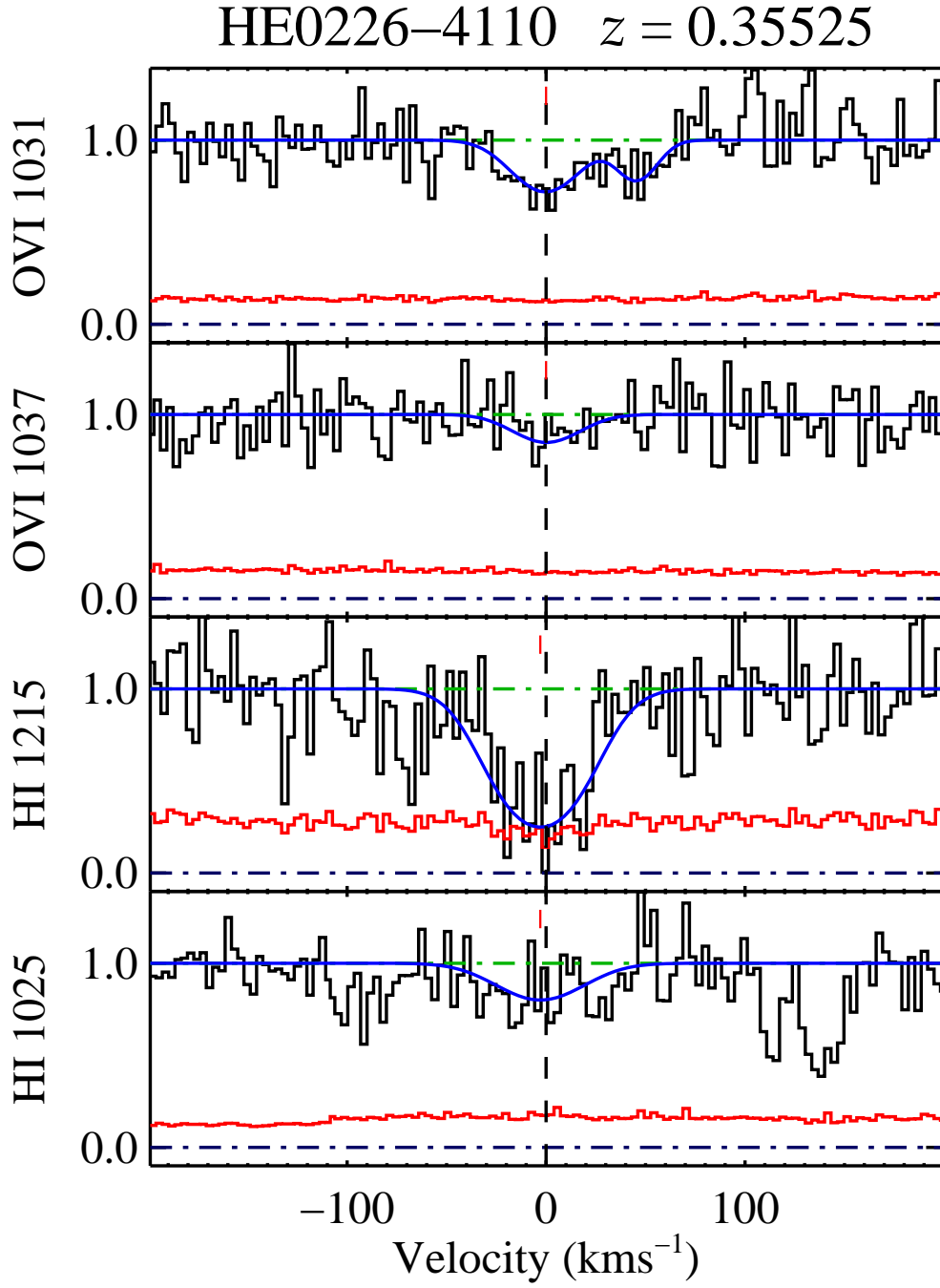


FIG. 11.— HE0226–4110 $z = 0.35525$ —O VI1031 in this system shows some evidence of contamination in the line wing, but this does not unduly affect our fits. Only associated H I lines are detected; no metal lines are seen in our STIS data.

TABLE 7
O VI ABSORBER MEASUREMENTS ALONG THE LINE OF SIGHT TOWARDS HE 0226–4110

ion	z_{comp}	v km s $^{-1}$	σ_v km s $^{-1}$	b km s $^{-1}$	σ_b km s $^{-1}$	$\log N$ log(cm $^{-2}$)	$\sigma_{\log N}$ log(cm $^{-2}$)	Flag
$z = 0.20702$								
O VI	0.20702	0	1	33.0	1.8	14.4	0.1	...
H I	0.20695	-18	2	23.7	2.7	15.0	...	L
H I	0.20706	10	15	35.9	6.7	14.7	...	L
C III	0.20697	-12	1	28.0	2.8	13.9	...	L
N V	0.20712	25	2	11.3	3.4	13.2	0.1	Z
N V	0.20698	-10	2	9.6	3.5	13.1	0.1	Z
Si III	0.20699	-6	2	7.7	4.8	12.1	0.2	...
Si III	0.20692	-24	1	6.0	2.0	12.3	0.1	...
$z = 0.32639$								
O VI	0.32639	0	3	24.8	4.8	13.6	0.2	...
H I	0.32639	0	0	27.9	0.0	12.5	...	U
$z = 0.34034$								
O VI	0.34035	2	1	16.8	1.7	13.9	0.1	...
H I	0.34033	-2	2	21.1	2.9	13.6	0.1	Z
H I	0.34054	45	2	5.4	4.3	12.7	0.2	...
C III	0.34033	-2	1	6.7	2.3	12.5	0.1	...
$z = 0.35525$								
O VI	0.35525	0	5	22.6	5.1	13.6	0.2	...
H I	0.35524	-3	2	28.6	3.3	13.7	0.1	...

TABLE 8
O VI ABSORBER MEASUREMENTS ALONG THE LINE OF SIGHT TOWARDS HS 0624+6907

ion	z_{comp}	v km s $^{-1}$	σ_v km s $^{-1}$	b km s $^{-1}$	σ_b km s $^{-1}$	$\log N$ log(cm $^{-2}$)	$\sigma_{\log N}$ log(cm $^{-2}$)	Flag
$z = 0.31796$								
O VI	0.31796	0	2	24.0	3.1	13.7	0.1	...
H I	0.31789	-15	4	35.9	6.5	13.3	0.1	...
$z = 0.33984$								
O VI	0.33984	0	7	34.8	11.6	13.4	0.3	Z
H I	0.33978	-14	0	40.9	0.9	14.5	0.1	...

TABLE 9
O VI ABSORBER MEASUREMENTS ALONG THE LINE OF SIGHT TOWARDS PG 0953+415

ion	z_{comp}	v km s $^{-1}$	σ_v km s $^{-1}$	b km s $^{-1}$	σ_b km s $^{-1}$	$\log N$ log(cm $^{-2}$)	$\sigma_{\log N}$ log(cm $^{-2}$)	Flag
$z = 0.14232$								
O VI	0.14232	-1	3	31.9	4.5	14.2	0.1	...
H I	0.14232	1	2	28.7	2.2	13.5	0.1	...
C II	0.14233	2	3	8.3	4.6	12.8	0.2	Z

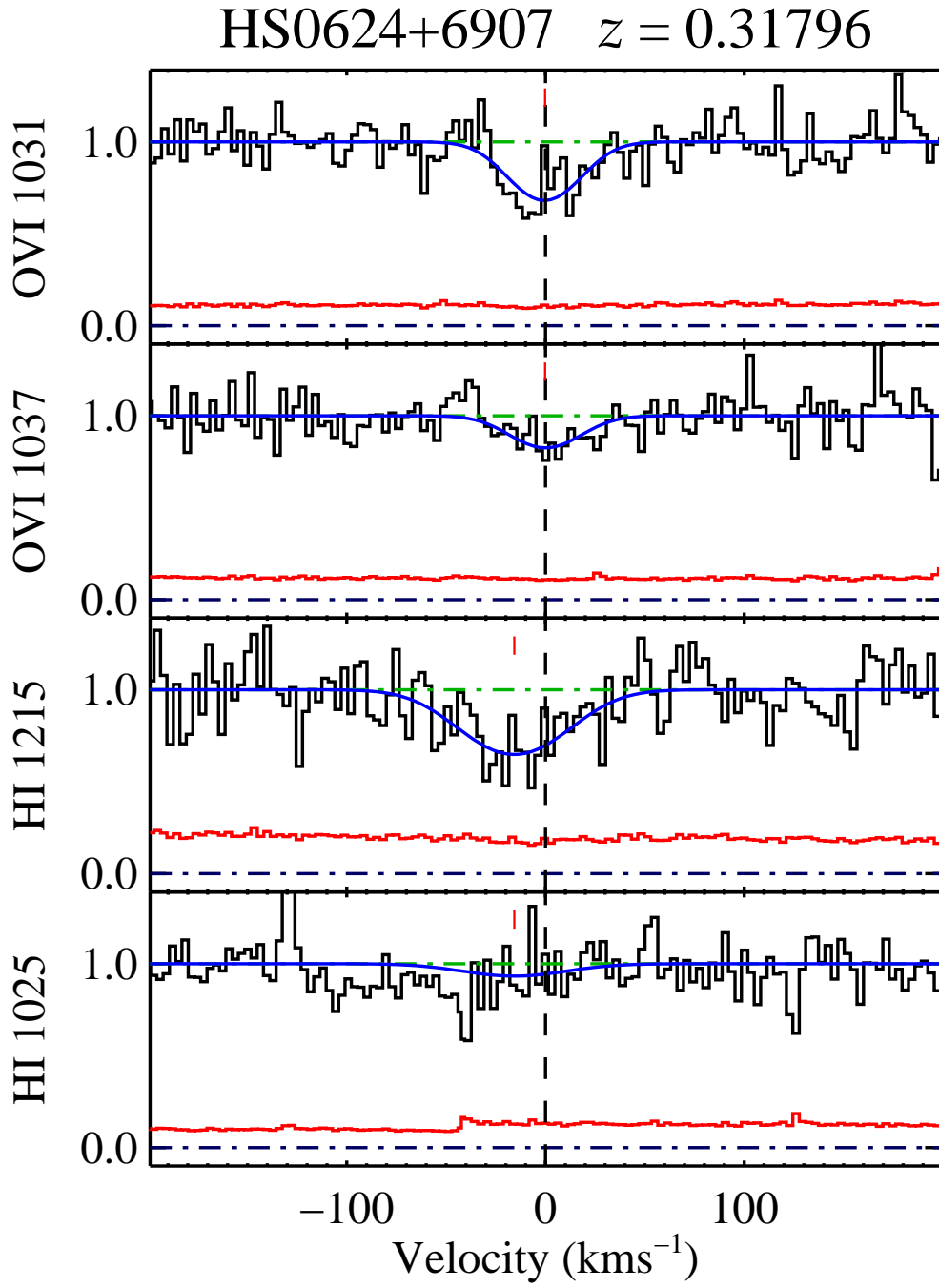


FIG. 12.— HS0624+6907 $z = 0.31796$ —This weak absorber is detected only in O VI and Ly α , with a 15 km s^{-1} offset between the two species.

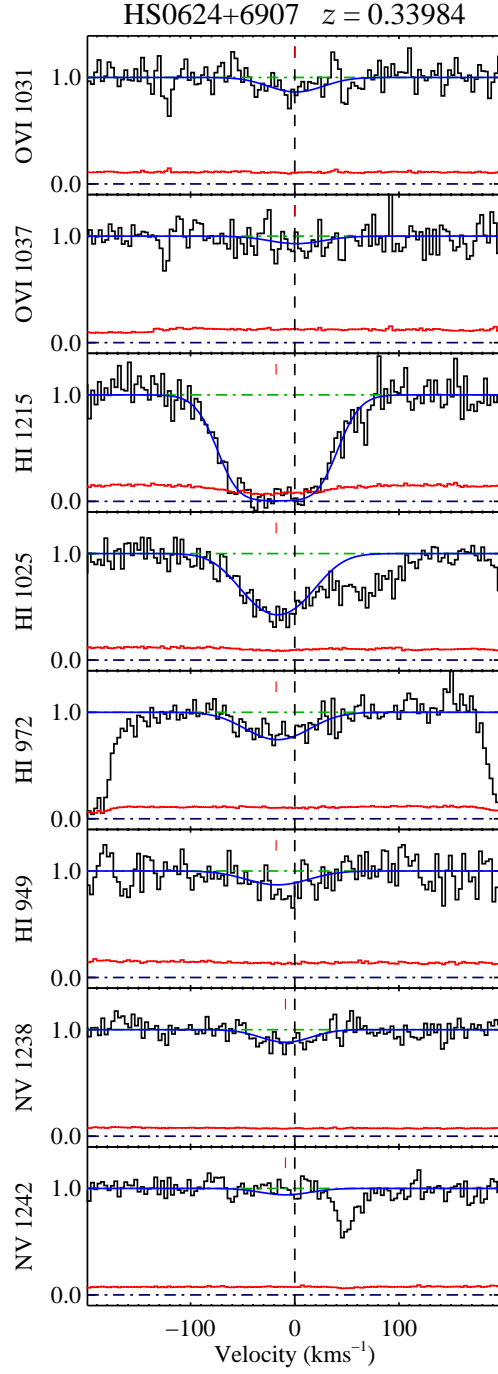


FIG. 13.— HS0624+6907 $z = 0.33984$ —While the Ly α line is heavily saturated in this absorber, the O VI lines are very weak. The Ly β profile is partly blended, but the Ly γ line is free from contamination. No significant absorption from other species are detected.

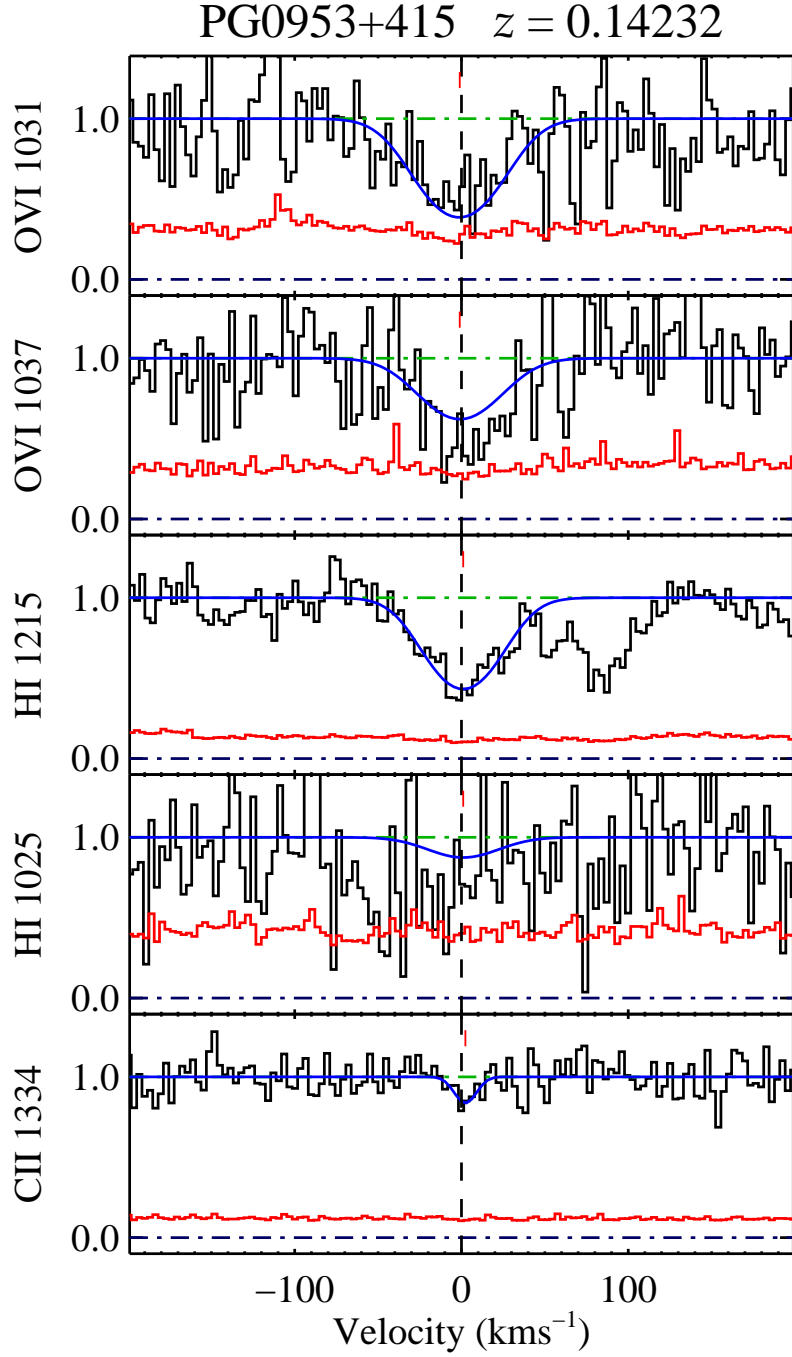


FIG. 14.— PG 0953+415 $z = 0.14232$ —Strong O VI is present in this system, although the O VI 1037 line is stronger than expected. H I is well fit in the Ly α line, and is not affected by the blending seen to the red of the line. Ly β in this absorber is contaminated by H 1949 line from the QSO host at $z = 0.2335$. C II 1334 may be present, but is extremely weak and we flag it as uncertain.

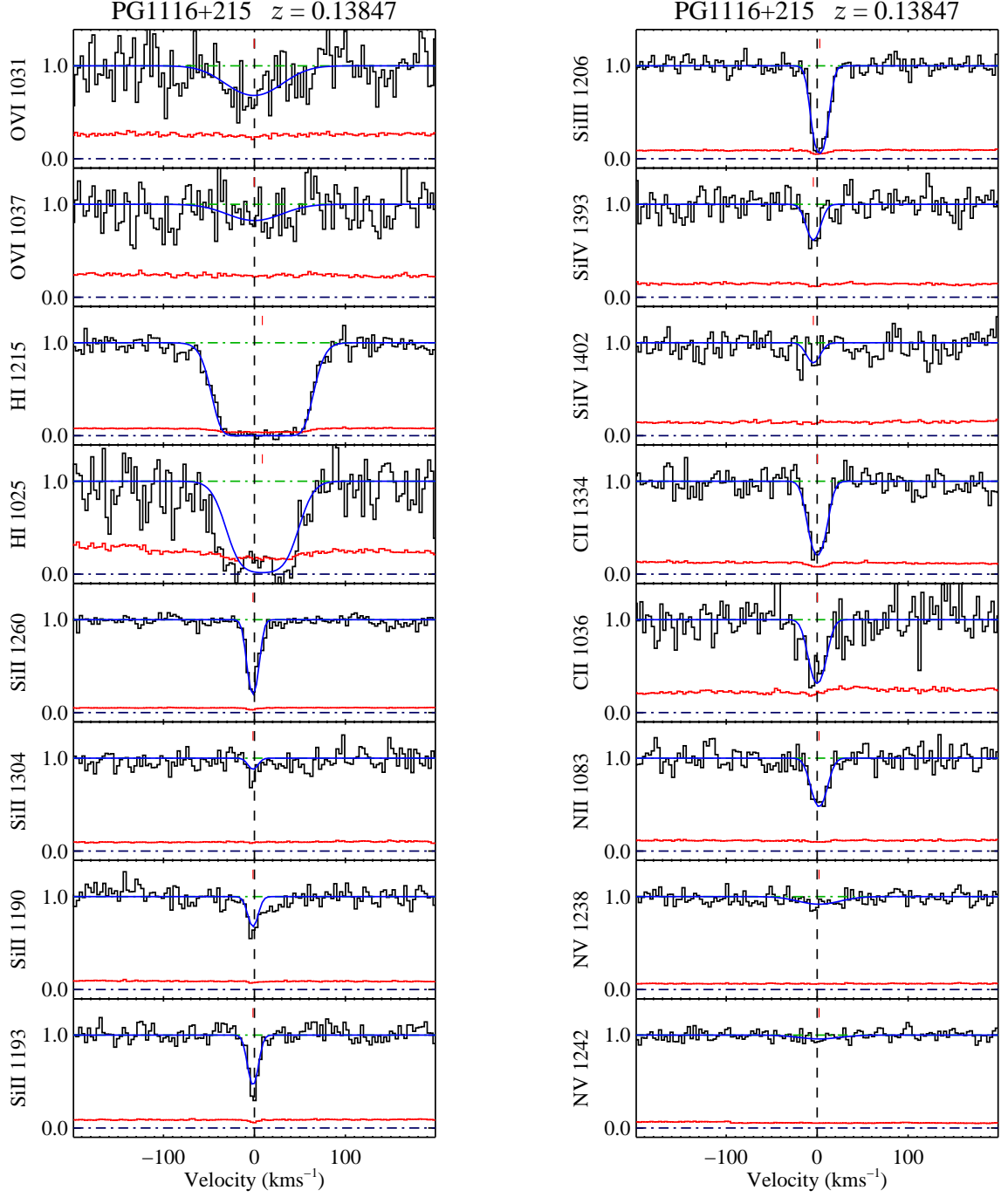


FIG. 15.— PG 1116+215 $z = 0.13847$ —While the O VI transitions in this absorber are quite noisy, we have good data for Ly α, β , both of which are saturated. We cannot obtain satisfactory fits to Ly α and Ly β simultaneously. Si II, Si III, Si IV, N II and C II are all clearly detected, often in multiple transitions (e.g. Si II is detected in the 1190, 1193, 1260 and 1304 transitions).

TABLE 10
O VI ABSORBER MEASUREMENTS ALONG THE LINE OF SIGHT TOWARDS PG 1116+215

ion	z_{comp}	v km s^{-1}	σ_v km s^{-1}	b km s^{-1}	σ_b km s^{-1}	$\log N$ $\log(\text{cm}^{-2})$	$\sigma_{\log N}$ $\log(\text{cm}^{-2})$	Flag
$z = 0.13847$								
O VI	0.13847	0	6	40.5	8.7	13.9	0.1	...
H I	0.13850	8	0	30.0	0.6	15.0	...	L
C II	0.13847	0	0	11.1	0.9	13.9	0.1	...
N II	0.13848	2	1	10.7	1.4	13.7	0.1	...
N V	0.13848	2	5	31.3	7.6	13.0	0.1	...
Si II	0.13846	-1	0	6.6	0.3	12.8	0.1	...
Si III	0.13848	2	0	8.6	0.5	13.0	0.1	...
Si IV	0.13845	-4	1	9.5	2.2	12.7	0.1	...

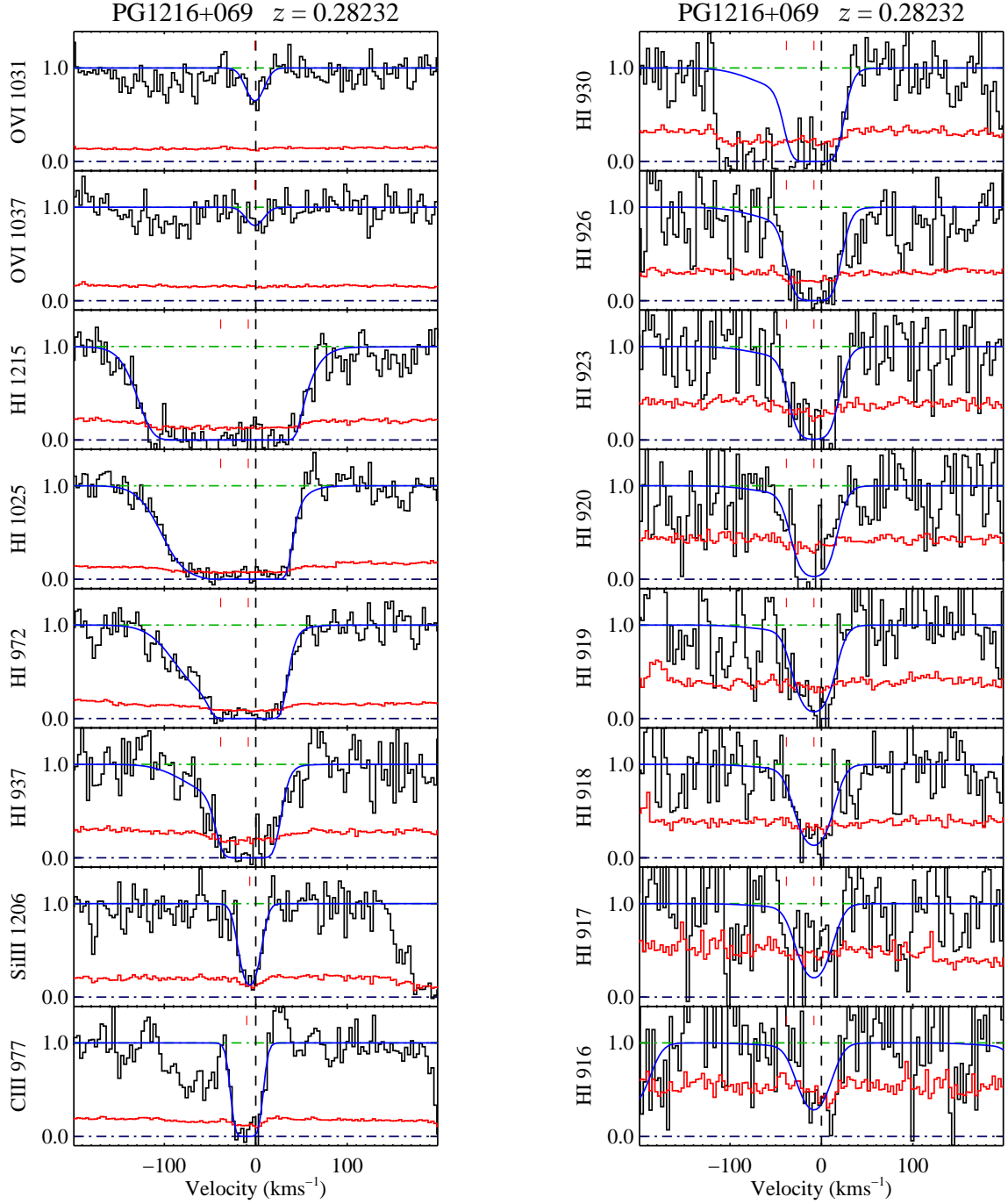


FIG. 16.— PG 1216+069 $z = 0.28232$ —This system is another instance of very strong, saturated H I, strong low ion metal species, but only weak O VI. All the Lyman series lines in our spectrum are saturated, or are too noisy to be useful. C III 977 is also saturated. It is not clear whether the absorption to the blue of the central C III component is C III associated with blue H I components, or a contaminating line.

TABLE 11
O VI ABSORBER MEASUREMENTS ALONG THE LINE OF SIGHT TOWARDS PG 1216+069

ion	z_{comp}	v km s ⁻¹	σ_v km s ⁻¹	b km s ⁻¹	σ_b km s ⁻¹	$\log N$ log(cm ⁻²)	$\sigma_{\log N}$ log(cm ⁻²)	Flag
$z = 0.28232$								
O VI	0.28232	0	1	12.6	2.6	13.4	0.2	...
H I	0.28216	-38	1	48.3	1.0	15.2	...	L
H I	0.28229	-8	0	20.2	0.6	16.5	...	L
C III	0.28228	-9	0	10.1	1.6	14.2	...	L
Si III	0.28229	-6	0	11.7	1.3	12.9	0.1	...

TABLE 12
O VI ABSORBER MEASUREMENTS ALONG THE LINE OF SIGHT TOWARDS PG 1259+593

ion	z_{comp}	v km s ⁻¹	σ_v km s ⁻¹	b km s ⁻¹	σ_b km s ⁻¹	$\log N$ log(cm ⁻²)	$\sigma_{\log N}$ log(cm ⁻²)	Flag
$z = 0.21950$								
O VI	0.21934	-39	2	18.9	3.2	13.7	0.1	Z
O VI	0.21950	0	1	13.6	2.5	13.6	0.1	...
H I	0.21932	-44	31	46.0	13.6	14.0	0.5	...
H I	0.21948	-5	1	27.5	1.6	15.1	...	L
C III	0.21949	-2	0	10.8	2.0	13.7	...	L
Si III	0.21950	0	1	8.7	2.6	12.1	0.1	...
$z = 0.25981$								
O VI	0.25962	-44	3	15.0	3.6	13.5	0.1	...
O VI	0.25982	4	6	34.2	9.6	13.6	0.1	...
H I	0.25963	-43	7	26.6	5.0	13.6	0.2	...
H I	0.25982	1	6	25.3	5.3	13.5	0.2	...

TABLE 13
O VI ABSORBER MEASUREMENTS ALONG THE LINE OF SIGHT TOWARDS PHL 1811

ion	z_{comp}	v km s ⁻¹	σ_v km s ⁻¹	b km s ⁻¹	σ_b km s ⁻¹	$\log N$ log(cm ⁻²)	$\sigma_{\log N}$ log(cm ⁻²)	Flag
$z = 0.15786$								
O VI	0.15786	0	5	42.0	7.8	13.9	0.2	...
H I	0.15785	-3	5	49.9	7.1	13.3	0.1	...

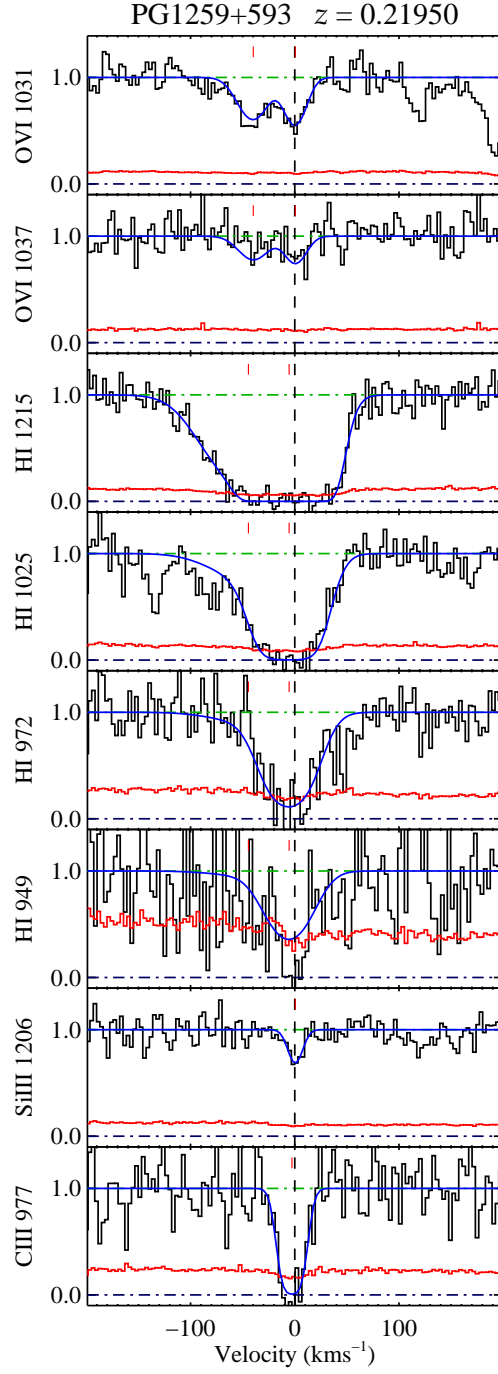


FIG. 17.— PG 1259+593 $z = 0.21950$ —Multi-component O VI and H I are both present in this system, with the H I lines saturated. The blue wing of the Ly β line blends with Galactic S II 1250. C III and Si III are both detected; C III is saturated, while the Si III line is weak. Both species align with the $v = 0 \text{ km s}^{-1}$ component.

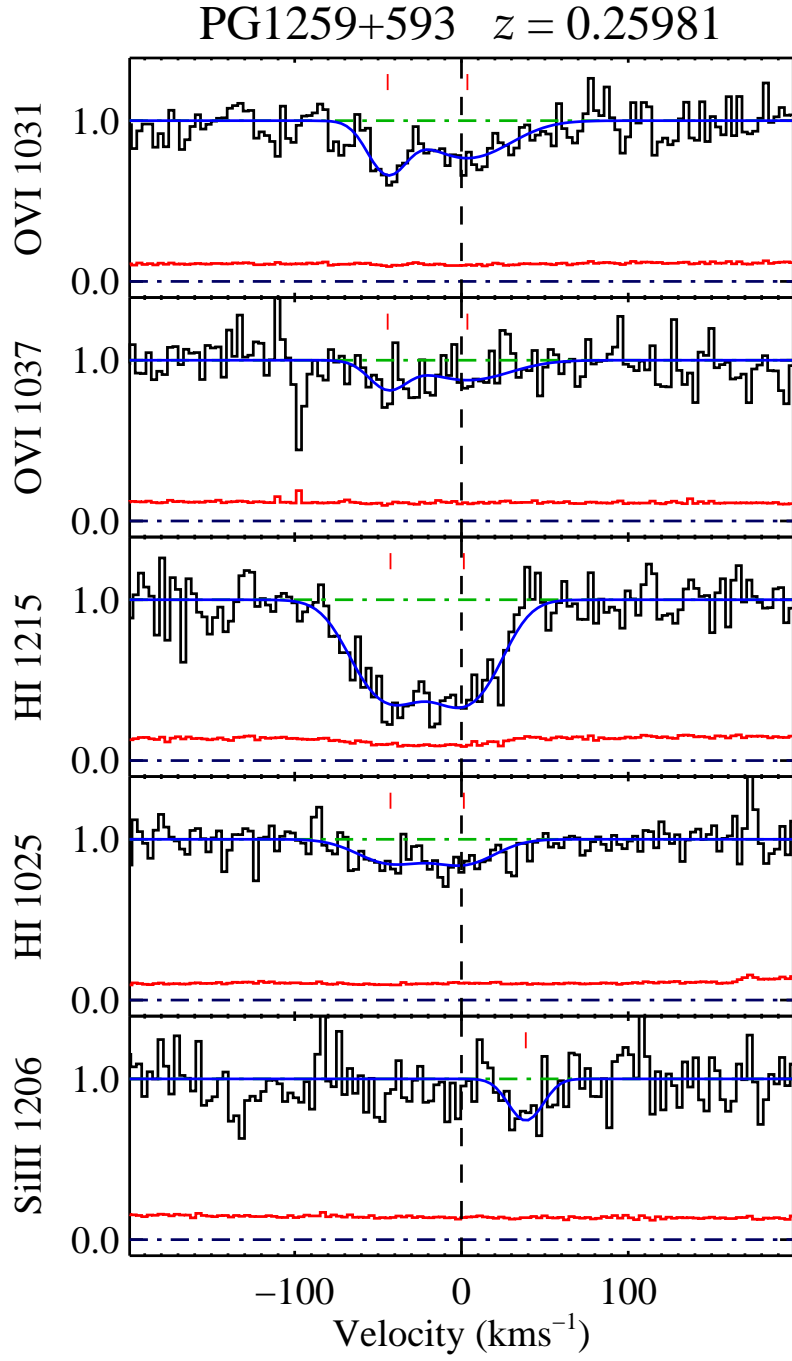


FIG. 18.— PG 1259+593 $z = 0.25981$ —This double-component absorber shows only two O VI and H I components.

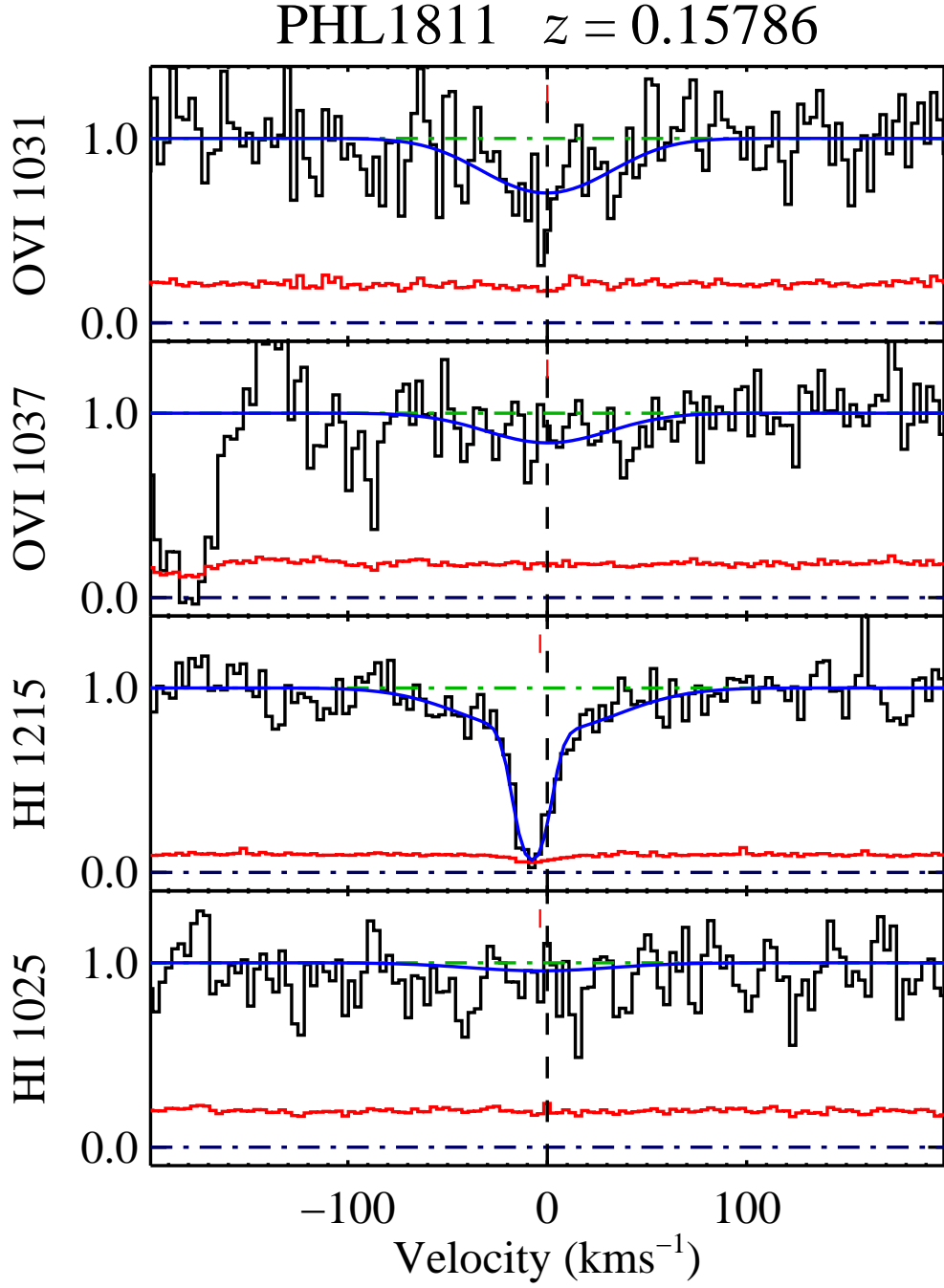


FIG. 19.— PHL1811 $z = 0.15786$ —Both O VI and H I in this system are weak. The putative narrow H I component is *not* H I, but rather O I 1302 in the $z = 0.0809$ Lyman-limit system. We include this line in the fit, detecting only broad, weak H I that is too weak to be detected in the Ly β transition.

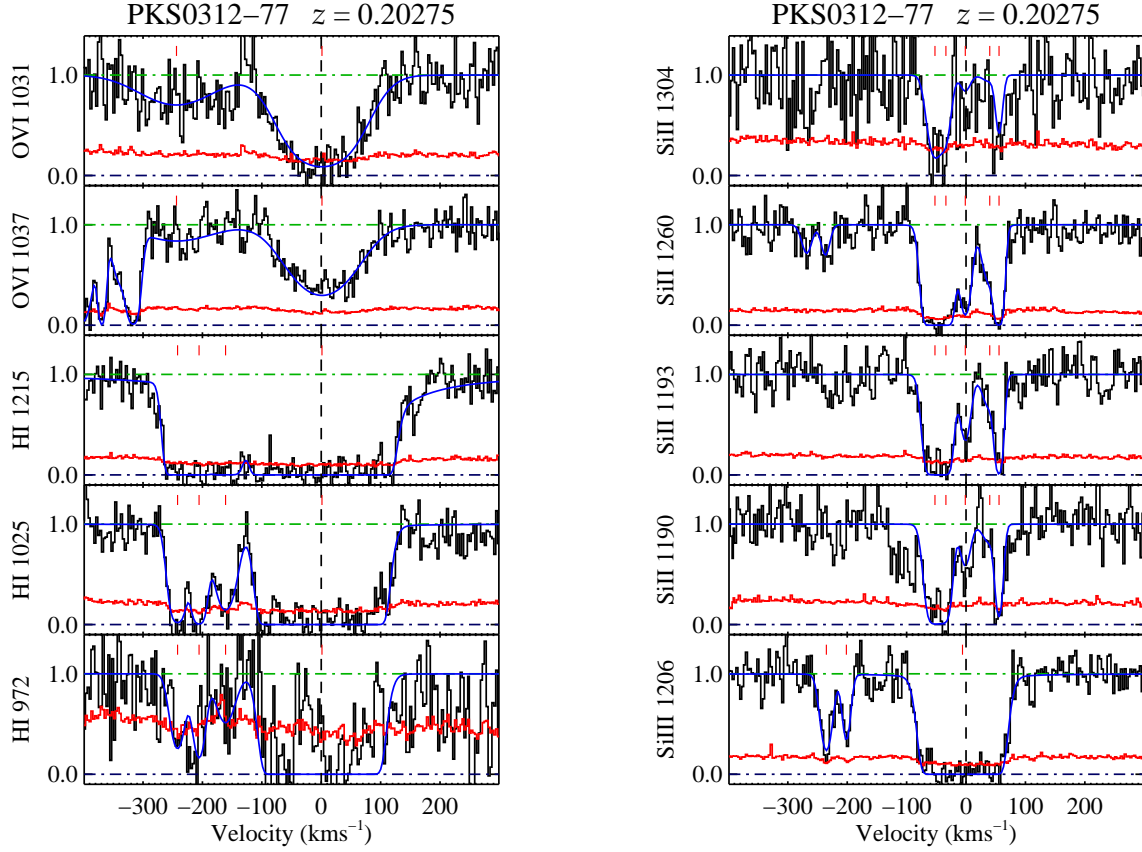


FIG. 20.— PKS0312-77 $z = 0.20275$ —This Lyman-limit system shows strong, saturated O VI H I, Si II, Si III Si IV and C III. We also see weak N V. We are not able to resolve multiple absorption components in the main O VI absorber, but their presence is strongly suggested by the complicated component structure exhibited in other transitions.

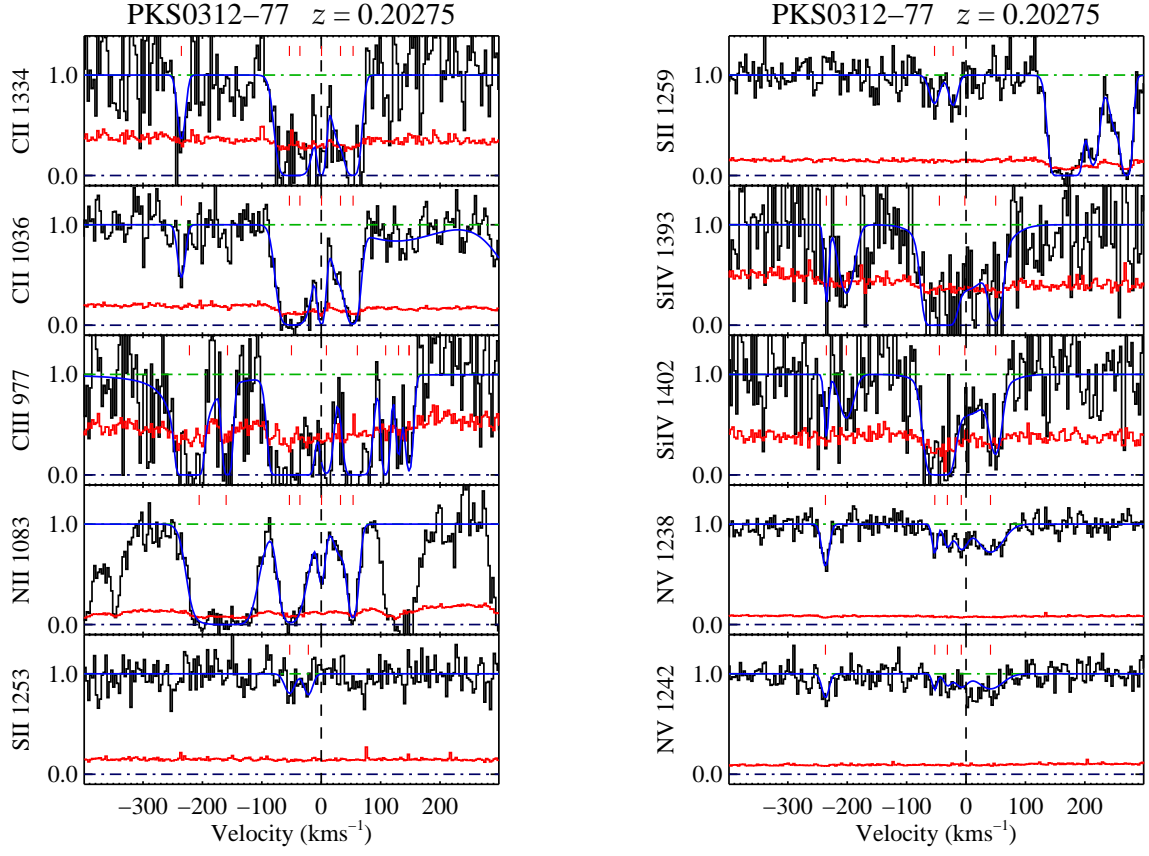


FIG. 21.— Further transitions of the PKS 0312-77 $z = 0.20275$ system, as for Figure 20.

TABLE 14
O VI ABSORBER MEASUREMENTS ALONG THE LINE OF SIGHT TOWARDS PKS 0312–77

ion	z_{comp}	v km s ⁻¹	σ_v km s ⁻¹	b km s ⁻¹	σ_b km s ⁻¹	$\log N$ log(cm ⁻²)	$\sigma_{\log N}$ log(cm ⁻²)	Flag
$z = 0.20275$								
O VI	0.20177	-243	8	80.8	13.1	14.1	0.1	...
O VI	0.20276	1	1	68.4	2.3	14.9	0.2	...
H I	0.20178	-241	1	14.6	1.2	14.7	0.1	...
H I	0.20192	-205	1	11.8	2.7	14.7	0.1	...
H I	0.20210	-161	1	20.4	2.7	14.5	0.1	...
H I	0.20276	1	0	38.2	0.4	18.4	...	U
C II	0.20275	0	0	5.4	2.7	14.4	...	L
C II	0.20288	32	0	17.3	5.6	13.9	0.1	...
C II	0.20297	53	0	10.4	1.6	14.4	...	L
C II	0.20261	-35	0	19.8	5.3	14.5	...	L
C II	0.20254	-53	0	17.3	2.0	14.7	...	L
C II	0.20181	-235	1	7.2	1.9	13.5	0.1	...
C III	0.20279	8	3	9.8	6.1	13.6	0.4	...
C III	0.20299	60	2	15.5	5.9	14.3	...	L
C III	0.20255	-50	2	17.2	7.2	15.6	...	L
C III	0.20319	108	1	4.1	7.2	14.4	...	L
C III	0.20327	130	2	4.8	5.5	13.0	...	L
C III	0.20334	147	2	6.1	5.2	13.1	0.3	...
C III	0.20212	-157	1	4.9	6.7	14.3	...	L
C III	0.20186	-221	2	8.1	1.6	16.8	...	L
N II	0.20275	0	0	6.8	5.5	13.6	0.3	...
N II	0.20288	32	0	14.4	16.6	13.5	0.4	...
N II	0.20297	53	0	9.0	3.0	14.2	...	L
N II	0.20261	-35	0	19.4	10.4	14.1	...	L
N II	0.20254	-53	0	15.9	4.2	14.5	...	L
N II	0.20211	-160	0	35.6	6.7	15.2	...	L
N II	0.20193	-205	0	19.1	7.6	14.3	...	L
N V	0.20272	-7	9	13.8	18.8	13.1	0.5	...
N V	0.20291	41	8	27.6	13.6	13.5	0.2	...
N V	0.20262	-31	8	7.9	12.1	12.9	0.7	...
N V	0.20254	-52	3	4.3	5.9	12.9	0.3	...
N V	0.20180	-236	2	7.2	3.7	13.2	0.2	...
S II	0.20266	-21	2	9.0	3.1	14.1	0.1	...
S II	0.20254	-53	2	10.7	3.4	14.1	0.1	...
Si II	0.20275	-1	0	10.5	1.8	13.1	0.1	...
Si II	0.20291	39	9	15.3	7.4	12.8	0.3	...
Si II	0.20297	55	0	6.3	1.2	13.6	0.2	...
Si II	0.20261	-33	5	10.1	3.7	13.8	0.3	...
Si II	0.20254	-52	2	14.2	1.2	14.2	0.2	...
Si III	0.20273	-5	0	30.4	2.3	15.7	...	L
Si III	0.20194	-201	1	7.9	1.8	12.5	0.1	...
Si III	0.20181	-235	0	11.5	1.6	12.8	0.1	...
Si IV	0.20274	-1	22	56.6	14.5	13.7	0.2	...
Si IV	0.20295	49	2	11.1	3.9	13.5	0.2	...
Si IV	0.20257	-44	2	17.0	5.1	14.6	...	L
Si IV	0.20194	-201	0	15.2	4.7	13.2	0.1	...
Si IV	0.20181	-235	0	2.6	2.3	13.1	0.5	...

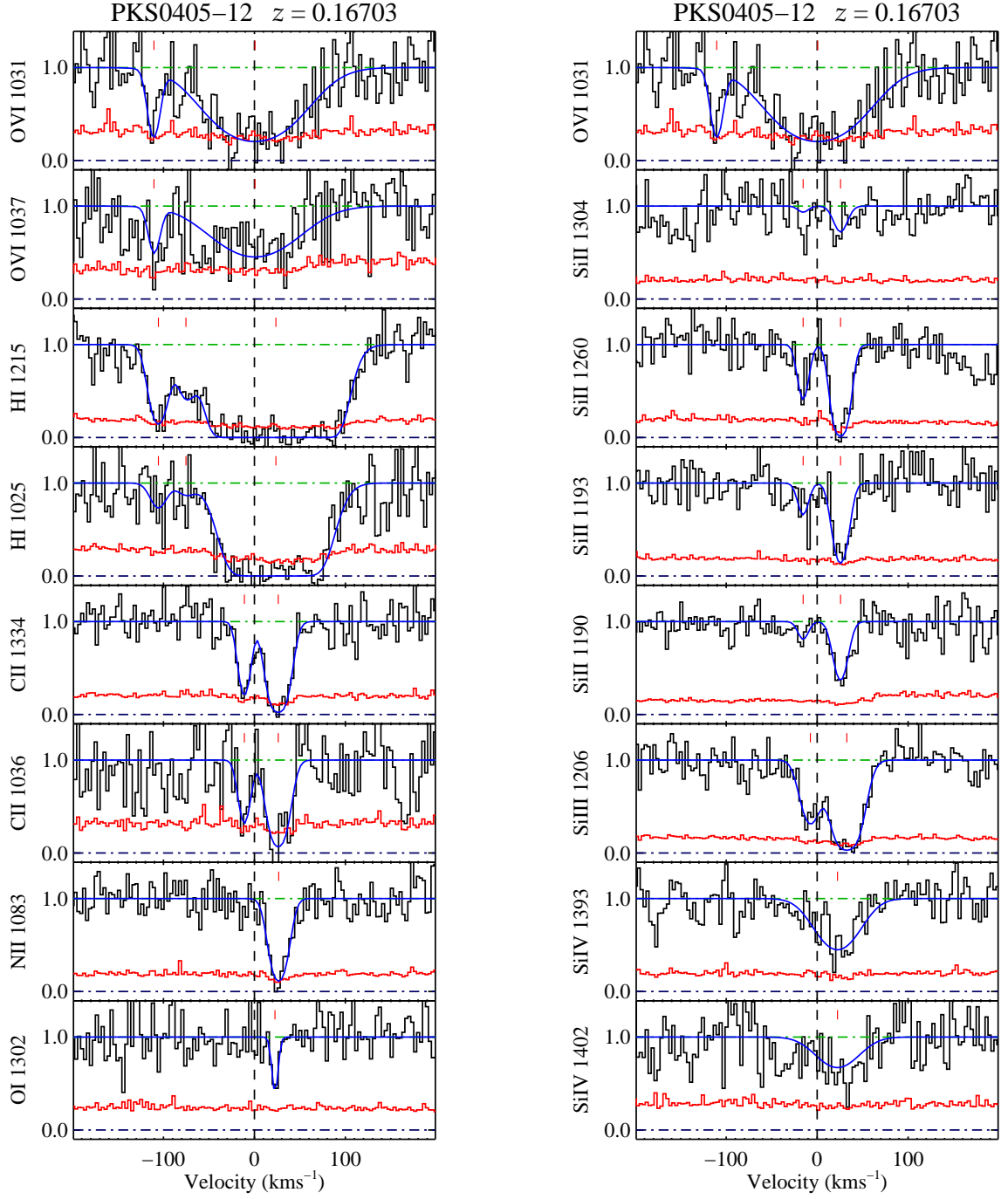


FIG. 22.— PKS0405-12 $z = 0.16703$ —This partial Lyman-limit system has strong O VI and corresponding saturated H I, and low ion metals with a complicated structure.

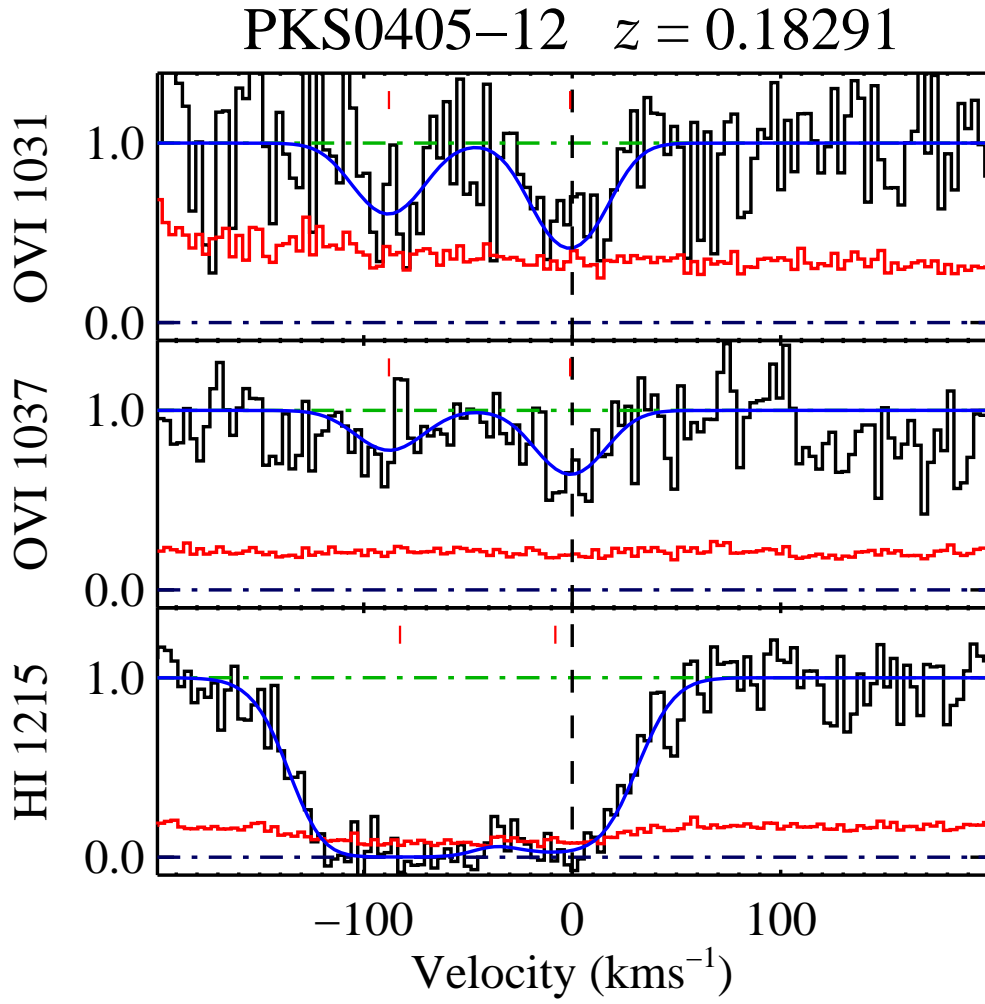


FIG. 23.— PKS0405–12 $z = 0.18291$ —This system has two strong O VI components separated by some 90 km s^{-1} . The O VI 1031 data are quite noisy. Both O VI components have corresponding H I absorption, but the Ly α line is heavily saturated and higher order lines are outside the wavelength coverage of our data. No metal absorption is seen.

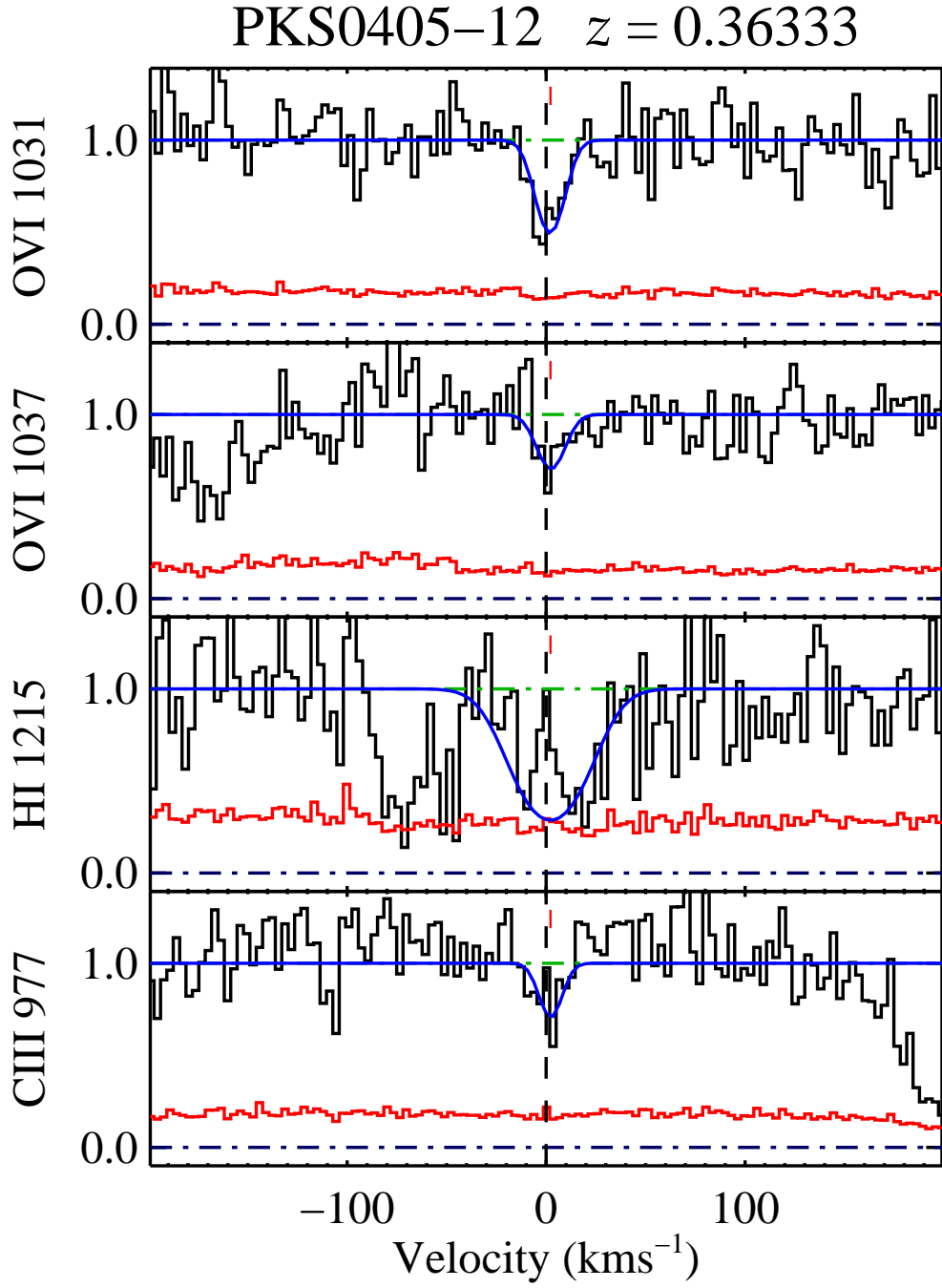


FIG. 24.— PKS0405–12 $z = 0.36333$ —This system shows weak O VI with a well-fit doublet. The Ly α line shows contamination from bad pixels, and is also possibly blended with Galactic C I* 1657; Ly β is not detected. Weak C III is also present.

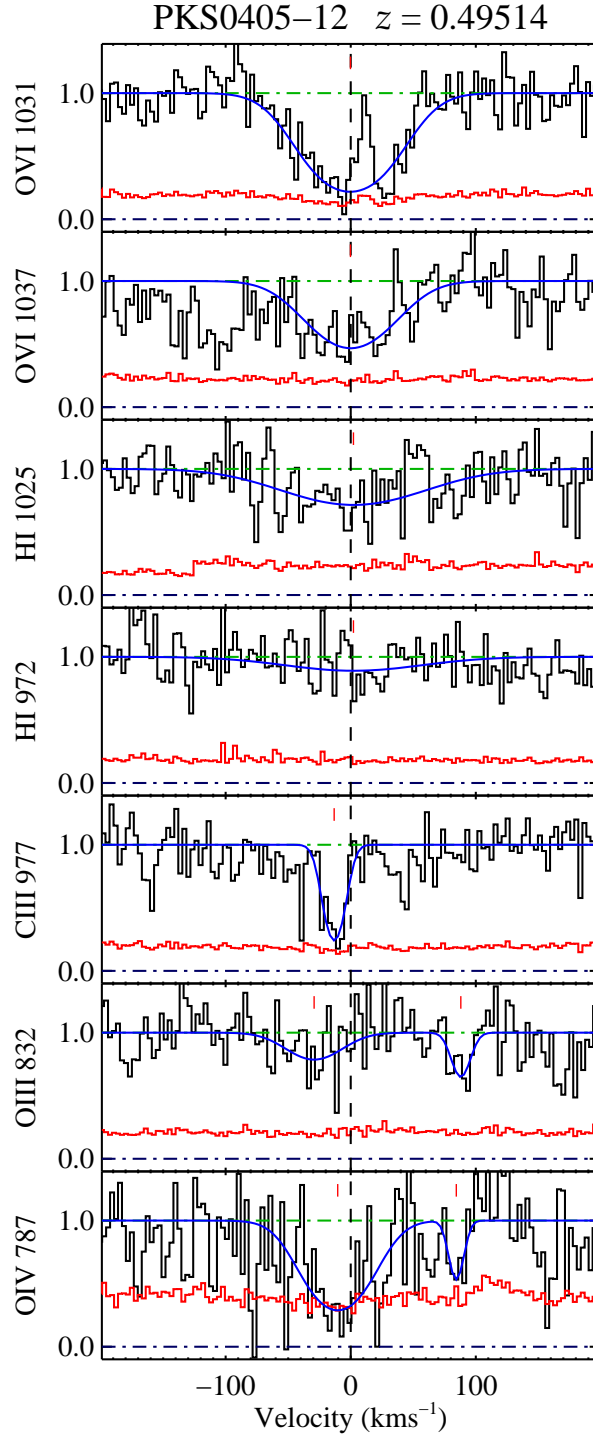


FIG. 25.— PKS0405-12 $z = 0.49514$ —The highest redshift absorber in our sample, both O VI lines are clearly detected, but both suffer from bad pixels, complicating the fitting. Ly α is redshifted out of our wavelength range, and Ly β shows a very wide profile. Strong C III is detected, as are O III and O IV.

TABLE 15
O VI ABSORBER MEASUREMENTS ALONG THE LINE OF SIGHT TOWARDS PKS 0405–12

ion	z_{comp}	v km s^{-1}	σ_v km s^{-1}	b km s^{-1}	σ_b km s^{-1}	$\log N$ $\log(\text{cm}^{-2})$	$\sigma_{\log N}$ $\log(\text{cm}^{-2})$	Flag
$z = 0.16703$								
O VI	0.16660	-110	1	7.4	2.2	13.8	0.2	...
O VI	0.16703	0	3	58.7	5.1	14.7	0.1	...
H I	0.16662	-105	1	11.5	2.2	13.5	0.1	...
H I	0.16674	-75	3	12.8	6.8	13.1	0.2	...
H I	0.16712	23	1	36.8	2.2	15.7	...	L
C II	0.16713	26	0	12.2	1.3	14.3	...	L
C II	0.16699	-11	1	7.4	1.4	13.7	0.1	...
N II	0.16713	26	1	11.2	1.3	14.2	...	L
O I	0.16712	22	1	2.5	2.2	13.8	0.3	Z
Si II	0.16713	25	0	9.4	1.0	13.3	0.1	...
Si II	0.16697	-15	1	6.9	2.1	12.5	0.1	...
Si III	0.16700	-7	1	13.1	2.2	12.7	0.1	...
Si III	0.16716	32	1	16.6	1.8	13.3	0.1	...
Si IV	0.16712	22	2	30.5	3.5	13.4	0.1	...
$z = 0.18291$								
O VI	0.18256	-87	4	21.5	6.5	13.7	0.2	...
O VI	0.18291	0	2	21.4	3.8	14.0	0.2	...
H I	0.18258	-82	4	35.3	3.1	14.5	...	L
H I	0.18288	-8	5	30.9	4.6	14.2	...	L
$z = 0.36333$								
O VI	0.36334	2	0	8.8	1.8	13.5	0.1	...
H I	0.36334	2	0	22.8	4.1	13.6	0.1	Z
C III	0.36334	2	0	6.9	3.8	12.4	0.2	Z
$z = 0.49514$								
O VI	0.49514	0	1	43.8	1.9	14.5	0.1	...
H I	0.49515	2	10	75.0	0.0	14.3	0.1	Z
C III	0.49507	-13	1	10.1	1.7	13.1	0.1	...
O III	0.49499	-29	8	29.9	11.1	13.7	0.1	Z
O III	0.49558	88	3	9.2	4.2	13.5	0.2	Z
O IV	0.49509	-10	6	33.0	0.0	14.5	0.1	Z
O IV	0.49556	85	5	6.9	5.7	13.6	0.2	Z

TABLE 16
O VI ABSORBER MEASUREMENTS ALONG THE LINE OF SIGHT TOWARDS PKS 1302–102

ion	z_{comp}	v km s^{-1}	σ_v km s^{-1}	b km s^{-1}	σ_b km s^{-1}	$\log N$ $\log(\text{cm}^{-2})$	$\sigma_{\log N}$ $\log(\text{cm}^{-2})$	Flag
$z = 0.22565$								
O VI	0.22553	-28	5	19.4	6.9	13.5	0.3	...
O VI	0.22565	0	2	13.4	2.8	13.7	0.1	...
H I	0.22553	-28	0	51.6	3.7	13.9	0.1	...
H I	0.22565	-1	6	23.6	10.8	13.3	0.3	...
$z = 0.22744$								
O VI	0.22744	0	1	11.4	2.4	13.5	0.1	...
H I	0.22743	-1	4	19.4	6.0	12.9	0.1	...

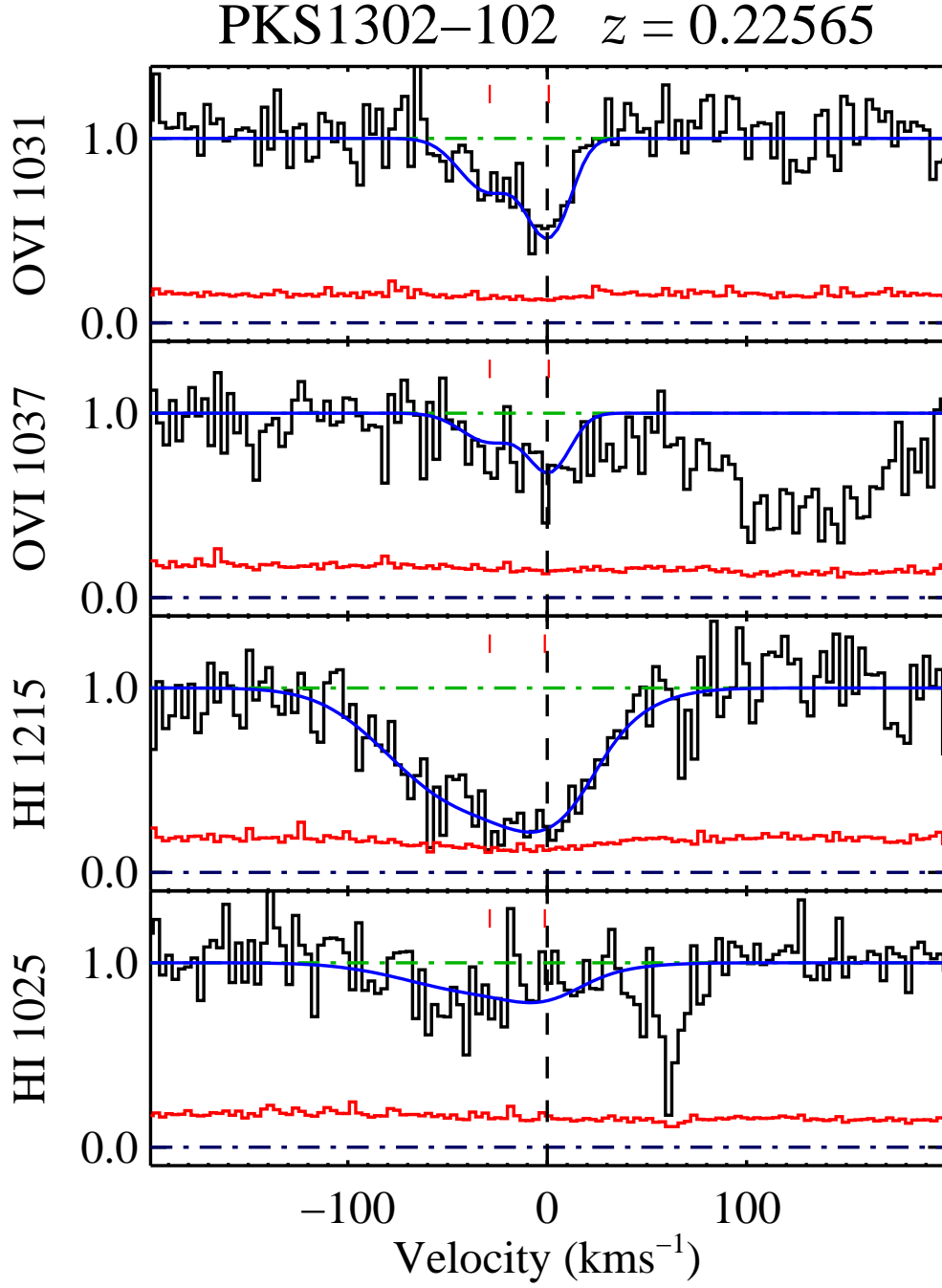


FIG. 26.— PKS1302–102 $z = 0.22565$ —The lopsided, two-component structure seen in O VI in this system is mirrored in the H I absorption. No other transitions are detected.

TABLE 17
O VI ABSORBER MEASUREMENTS ALONG THE LINE OF SIGHT TOWARDS TON 28

ion	z_{comp}	v km s^{-1}	σ_v km s^{-1}	b km s^{-1}	σ_b km s^{-1}	$\log N$ $\log(\text{cm}^{-2})$	$\sigma_{\log N}$ $\log(\text{cm}^{-2})$	Flag
$z = 0.27340$								
O VI	0.27340	0	3	20.9	4.2	13.4	0.2	...
H I	0.27337	-8	1	30.2	1.8	14.2	0.1	...

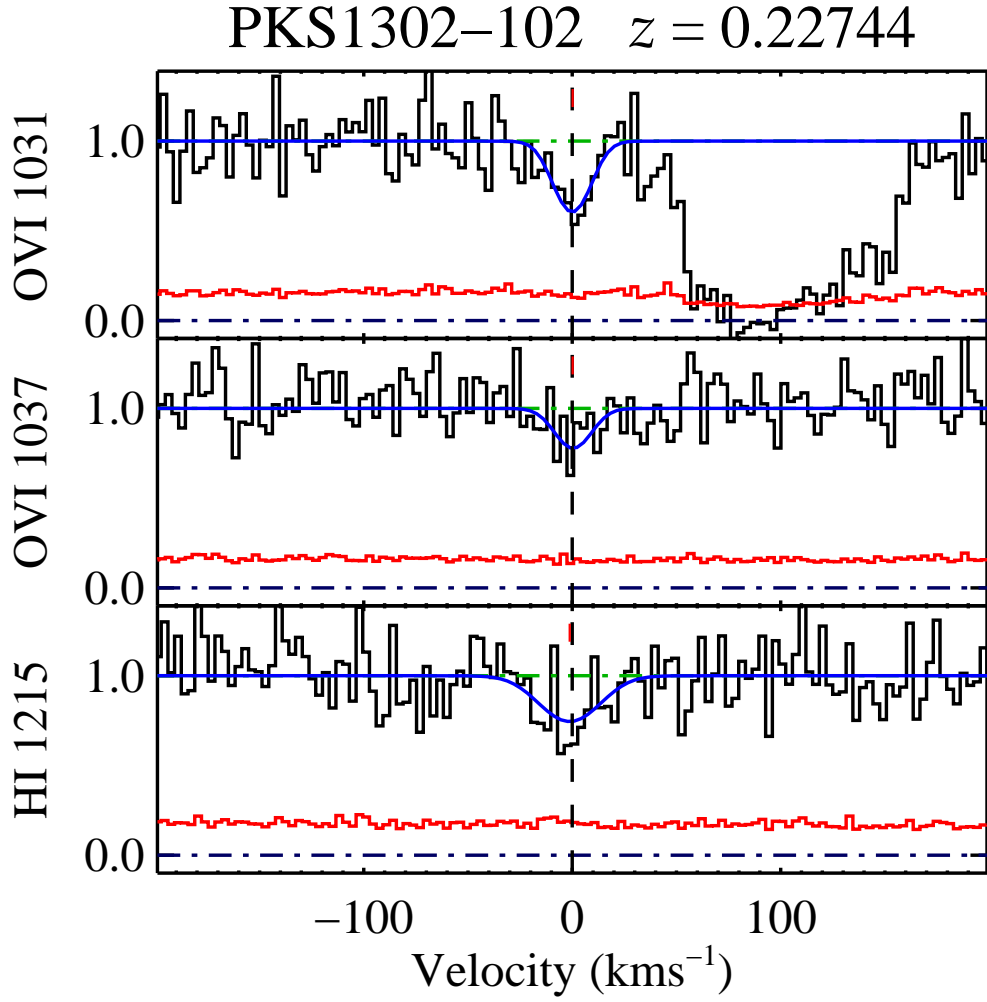


FIG. 27.— PKS 1302–102 $z = 0.22744$ —A mere 440 km s^{-1} from the absorber at $z = 0.22565$, this absorber is weaker than the lower redshift system. The O VI 1037 line is detected with low significance, and the corresponding H I line is very weak. The strong line to the red of the O VI 1031 line is Ly α .

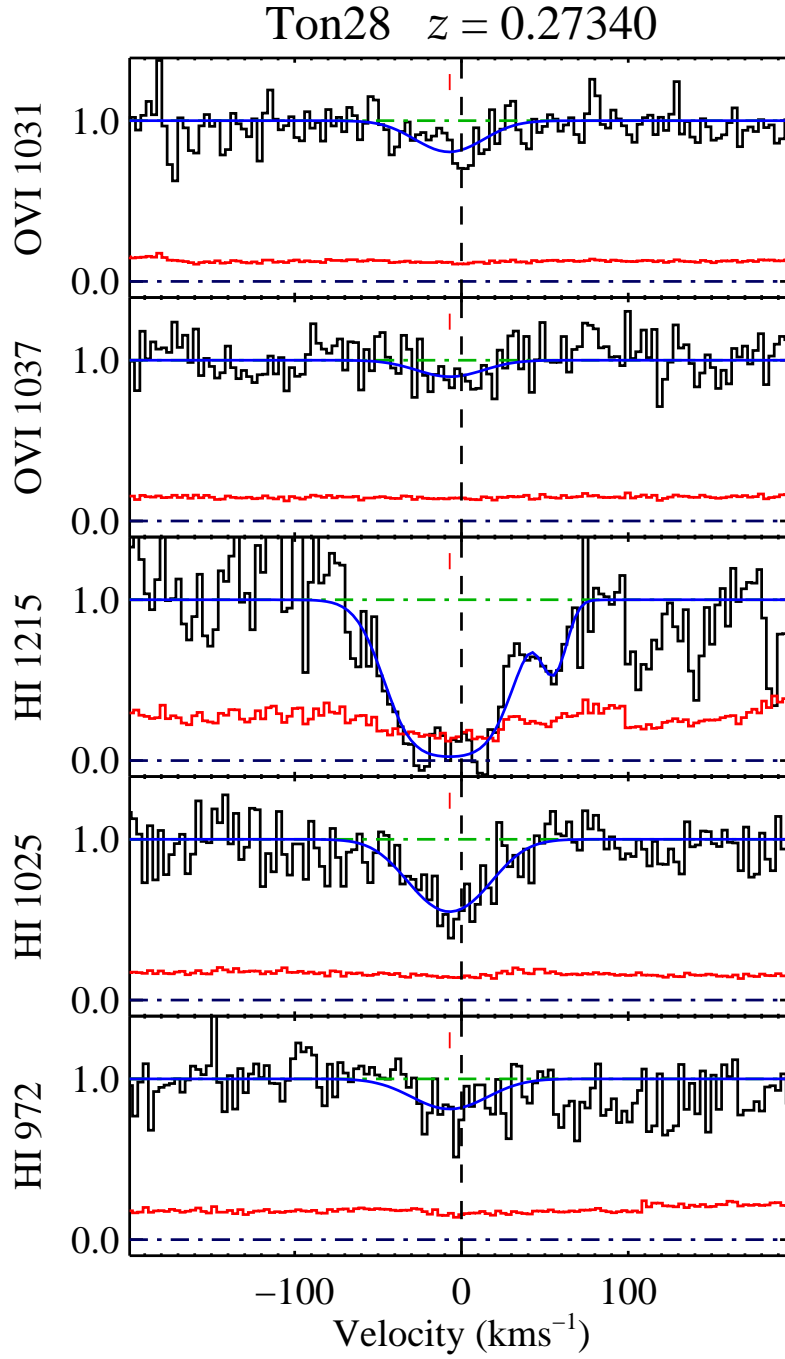


FIG. 28.— Ton28 $z = 0.27340$ —Only very weak O VI absorption is seen to correspond with the saturated Ly α in this system. Ly β is present and unsaturated, as is Ly γ . The Ly α line is blended with Galactic C IV 1548, which we fit simultaneously.

TABLE 18
SYSTEMS NOT CONFIRMED BY OUR SEARCH

QSO (1)	z_{abs} (2)	$N(\text{O VI})$ (3)	$N(\text{H I})$ (4)
3C 249.1	0.23641	13.99	13.23
3C 351.0	0.21811	13.96	13.50
3C 351.0	0.22111	14.25	>14.56
H 1821+643	0.12143	13.94	14.31
H 1821+643	0.21331	13.57	>14.29
HE 0226-4110	0.42670	14.34	... ^a
PG 1216+069	0.26768	13.30	>13.86
PG 1259+593	0.31972	13.92	14.04
PG 1444+407	0.22032	13.95	13.63
PHL 1811	0.13240	14.39	>14.30
PKS 0312-77	0.15890	13.94	13.90
PKS 0312-77	0.19827	13.84	>14.26
PKS 0405-12	0.36156	14.00	>14.14
PKS 1302-102	0.19159	13.93	>14.17
Ton 28	0.13783	13.99	>14.37
Ton 28	0.20524	13.69	13.20

NOTE. — Summary of O VI candidates which we do not recover. See text for details on individual systems.

^a Tripp et al. (2008) report no H I with this system. Ly α is redshifted out of the STIS band, and Ly β is not detected.

TABLE 19
DERIVED TEMPERATURES OF O VI/H I COMPONENTS

LOS	z_{abs}	v	$b_{\text{H I}}$	$b_{\text{O VI}}$	$\log T$	$\sigma_{\log T}$	b_{nt}	$b_{\text{H I}, therm}$	$b_{\text{O VI}, therm}$	$\log T_{nt=0}$
3C 249.1	0.24676	0	38.2	27.0	4.7	0.1	26.0	27.9	7.0	5.8
3C 273	0.12003	0	23.2	8.6	4.5	0.1	6.6	22.3	5.6	4.8
3C 351.0	0.31659	62	23.3	30.9	6.0
3C 351.0	0.31659	-3	26.9	23.3	4.1	0.4	23.0	13.9	3.5	5.7
3C 351.0	0.31659	-53	37.8	21.1	4.8	0.2	19.5	32.4	8.1	5.6
H 1821+643	0.26656	0	44.8	26.1	4.9	0.1	24.4	37.5	9.4	5.8
HE 0226-411	0.34034	2	21.1	16.8	4.0	0.3	16.5	13.2	3.3	5.4
HE 0226-411	0.35525	0	28.6	22.6	4.3	0.3	22.2	18.1	4.5	5.7
PG 0953+415	0.14232	-1	28.7	31.9	6.0
PG 1259+593	0.25981	-44	26.6	15.0	4.5	0.2	13.9	22.7	5.7	5.3
PG 1259+593	0.25981	4	25.3	34.2	6.1
PHL 1811	0.15786	0	49.9	42.0	4.7	0.4	41.5	27.8	6.9	6.2
PKS 0405-12	0.16703	-110	11.5	7.4	3.7	0.2	7.0	9.1	2.3	4.7
PKS 1302-10	0.22565	0	23.6	13.4	4.4	0.4	12.5	20.0	5.0	5.2
PKS 1302-10	0.22744	0	19.4	11.4	4.2	0.3	10.7	16.2	4.1	5.1
Ton 28	0.27340	0	30.2	20.9	4.5	0.2	20.2	22.4	5.6	5.6

NOTE. — Results of temperature and non-thermal broadening calculation for well-matched O VI and H I components. The line-of-sight, system and component are listed, along with the measured doppler parameters. The temperature, $\log T$, and non-thermal broadening, b_{nt} , are given. We also list the thermal component of the observed doppler parameter. The final column gives the temperature we would have derived if we assumed $b_{nt} = 0$. In three cases these parameters cannot be determined since $b_{\text{O VI}} > b_{\text{H I}}$.

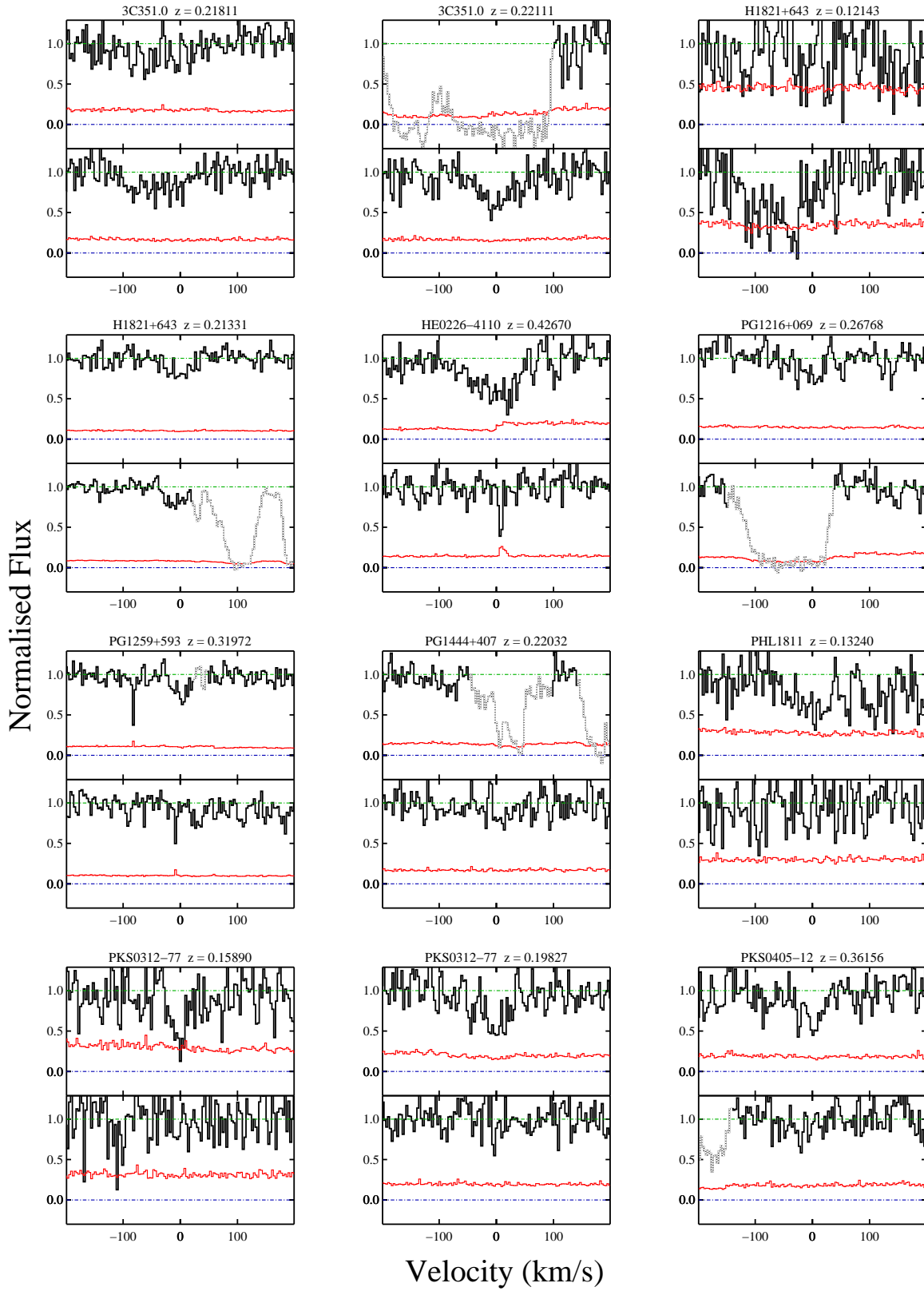


FIG. 29.— Spectra of the O VI 1031 (top) and O VI 1037 (bottom) spectral regions for absorbers we do not confirm. Blended regions are shown by dotted spectral regions.

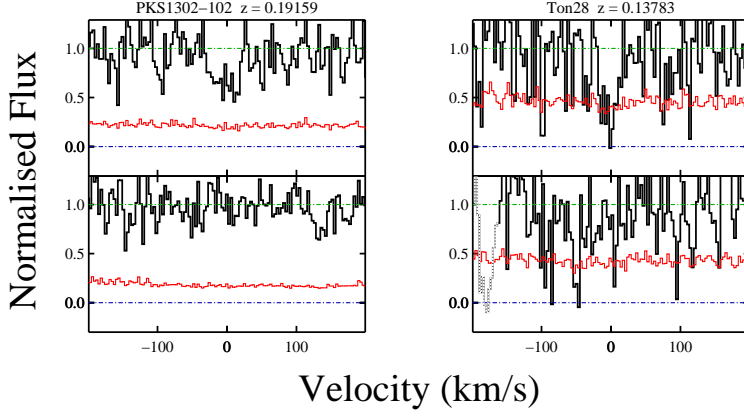


FIG. 30.— As for Figure 29, but remaining systems not shown in that figure.

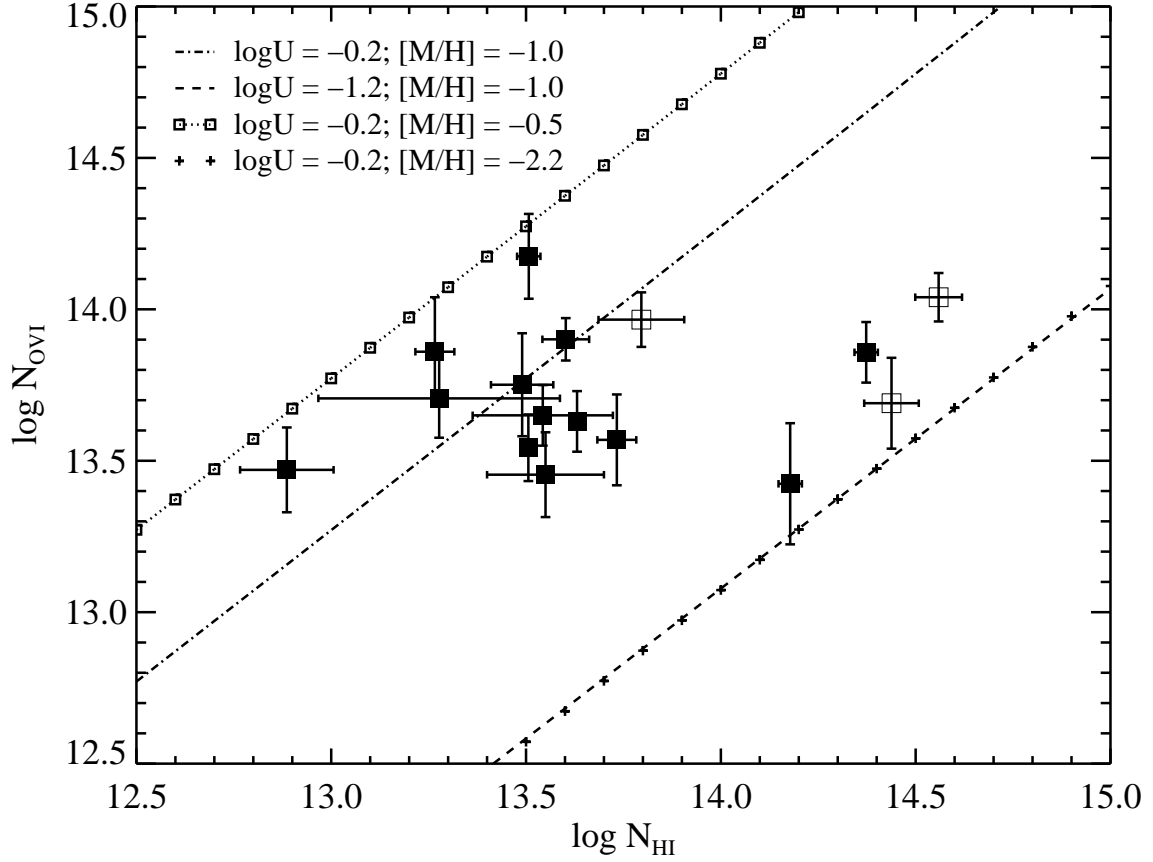


FIG. 31.— Distribution of O VI and H I column densities for well aligned absorption components. Full symbols are regular components, while open circles designate components whose alignment is flagged as uncertain.

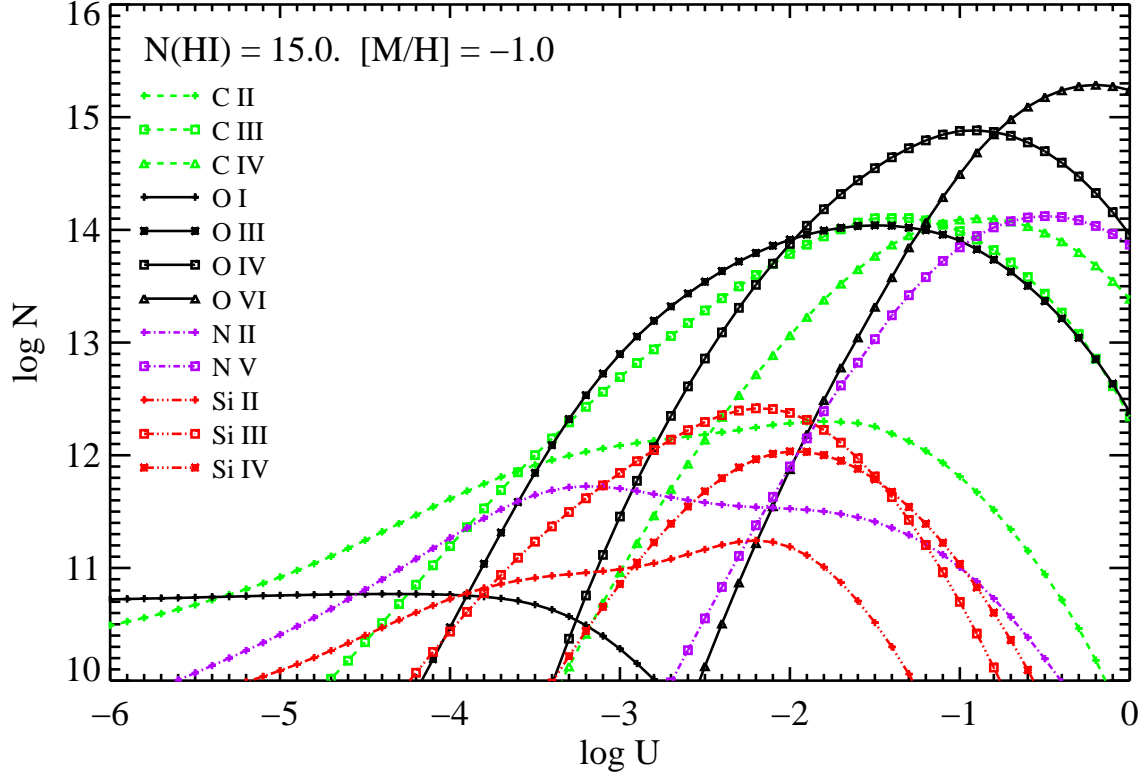


FIG. 32.— Example of column densities as a function of ionization parameter derived from *Cloudy* photoionization models. With increasing ionization parameter, species become more highly ionized, as expected. The models were computed for $\log N = 15.0$, and a nominal abundance $[M/H] = -1.0$. O VI dominates the Oxygen ionization at $\log U > -0.8$ and peaks at $\log U = -0.2$.

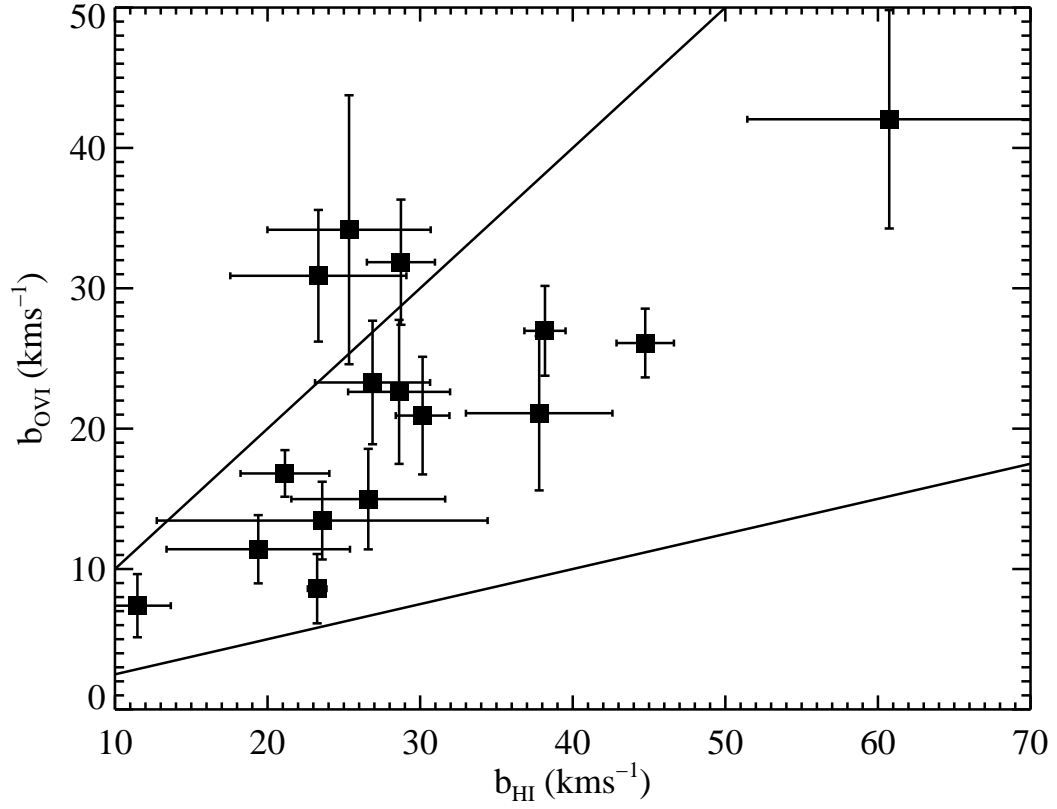


FIG. 33.— Distribution of Doppler parameters for aligned components. Symbols are the same as for Fig 31. The lower line shows the boundary for $b_{\text{nt}} = 0$, below which we should not see any components. The upper line shows $b_{\text{OVI}} = b_{\text{HI}}$, where the Doppler parameter is dominated by turbulent motions.